Magnesium Battery Electrolytes

in Ionic Liquids

by

Tylan Strike Watkins

A Dissertation Presented in Partial Fulfillment
of the Requirements for the Degree
Doctor of Philosophy

Approved December 2015 by the
Graduate Supervisory Committee:

Daniel Buttry, Chair
George Wolf
Peter Williams

ARIZONA STATE UNIVERSITY

May 2016

ABSTRACT

A lack of adequate energy storage technologies is arguably the greatest hindrance to a modern sustainable energy infrastructure. Chemical energy storage, in the form of batteries, is an obvious solution to the problem. Unfortunately, today's state of the art battery technologies fail to meet the desired metrics for full scale electric grid and/or electric vehicle role out. Considerable effort from scientists and engineers has gone into the pursuit of battery chemistries theoretically capable of far outperforming leading technologies like Li-ion cells. For instance, an anode of the relatively abundant and cheap metal, magnesium, would boost the specific energy by over 4.6 times that of the current Li-ion anode (LiC_6).

The work presented here explores the compatibility of magnesium electrolytes in $TFSI^-$-based ionic liquids with a Mg anode (TFSI = bis(trifluoromethylsulfonyl)imide). Correlations are made between the Mg^{2+} speciation conditions in bulk solutions (as determined via Raman spectroscopy) and the corresponding electrochemical behavior of the electrolytes. It was found that by creating specific chelating conditions, with an appropriate Mg salt, the desired electrochemical behavior could be obtained, i.e. reversible electrodeposition and dissolution. Removal of $TFSI^-$ contact ion pairs from the Mg^{2+} solvation shell was found to be essential for reversible electrodeposition. Ionic liquids with polyethylene glycol chains pendent from a parent pyrrolidinium cation were synthesized and used to create the necessary complexes with Mg^{2+}, from $Mg(BH_4)_2$, so that reversible electrodeposition from a purely ionic liquid medium was achieved.

The following document discusses findings from several electrochemical experiments on magnesium electrolytes in ionic liquids. Explanations for the failure of many of these systems to produce reversible Mg electrodeposition are provided. The key characteristics of ionic liquid systems that are capable of achieving reversible Mg electrodeposition are also given.

ACKNOWLEDGMENTS

First and foremost, I must thank my loving wife, Laura. We met as I was just beginning my graduate career, and without her unwavering support, I may never have made it through. She has a kind and caring soul, and I will be forever grateful for her presence in my life. Secondly, I would like to thank my parents, Sue and Cliff. Without their support and encouragement growing up, I may not have had the courage to pursue graduate school in the first place.

Of course, I would also like to thank my advisor, Daniel Buttry, not simply because it is customary to do so, but because he was willing to take me in when I was struggling to find a new research home. I did not begin my graduate career in Dr. Buttry's group and he was under no obligation to take a chance on me. As it turned out, joining his group was a blessing in more ways than I could have imagined. Not only was I able to escape from a previous situation that proved very unhealthy for me, but I was also introduced to a project—and consequently a field of research—that I would soon come to love. Without Dan's support, guidance, and willingness to take a risk on a student in need, none of this dissertation would have been possible.

Furthermore, I gratefully acknowledge use of the facilities and equipment of the Center for Solid State Science (CSSS). This is a world class facility with a great supporting staff. Staff scientists like Barry Wilkens (in charge of Rutherford Back Scattering) and Emmanuel Soignard (Raman Spectroscopy and High Resolution X-ray Diffraction) were always willing and available for help, and they provided it in a warm and friendly manner. Their help was paramount to my growth and success.

I should not go without acknowledging the aid and companionship of previous lab mates Gordon Gryzbowski and Rick Beeler, whose guidance and wealth of knowledge helped me build a strong research foundation.

Naturally, special thanks are also due to Buttry group members Ashok Kumar, Joseph Reinhardt, and Poonam Singh who I spent countless hours with discussing science and beyond.

Finally, I would like to thank all my friends and family, whose support helped give me the strength to move forward, even during the most trying of times.

This thesis was supported by the Army Research Office (ARO) under Grant number W911NF-11-1-0432.

TABLE OF CONTENTS

Page

Page

LIST OF TABLES

Table Page

LIST OF FIGURES

Figure Page

Figure Page

Figure Page

CHAPTER 1

INTRODUCTION

1.1 The Need for Energy Storage

As of this writing, the world's population is just shy of 7.3 billion people.[1] Collectively, this population consumes over 100 PWh (10^{15} Wh) of energy on an annual basis, only 21% of which is from renewable sources.[2] Energy being consumed from the combustion of fossil fuels—the other 79%—leads to the emissions of over 30 gigatonnes of CO_2 every year; this is over twice the emissions rate observed in 1970. The non-reversible nature of these emissions has led to continuously increasing CO_2 levels in our atmosphere (currently around 400 ppm, which is higher than it has been for one million years).[3] The vast majority of climate scientists agree that such staggeringly high CO_2 levels have directly affected the planet's changing climate in a way that is likely harmful to much, if not all, of Earth's many lifeforms—including humans. Adding to the issue are the facts that fossil fuels are ultimately a limited resource and they are not evenly distributed across the globe—both of which result in conflicts between nations. Thus, energy and related issues should be at the top of the list for concerned global citizens of current and future generations.

One way to combat CO_2 emissions, other hazardous environmental pollution, and our declining supply of nonrenewable fuels is to continually seek more sophisticated energy conversion options. Grand endeavors in progress, like the pursuit of workable nuclear fusion reactors, promise the ultimate energy sustainability option. However, such

a technology is, at best, likely decades away. At the moment, each renewable energy source comes with obvious drawbacks. For instance, the ultimate source of energy in our solar system, the sun, delivers an average 250 W/m^2 of electromagnetic radiation incident on the Earth's surface (value calculated from an average solar radiative rate intercepted by Earth of 1367 W/m^2 and an average atmospheric albedo of 0.26).[4,5] At practical photovoltaic photon-to-electricity energy conversion efficiencies (around 20% for modern commercial terrestrial units) solar panels would need to cover 0.34% of Earth's land surface (roughly the size of the state of Texas) to power the world's economy. Unfortunately, even this is a drastic oversimplification of the problem. For one, the energy flow is not steady; varying weather patterns and night fall create disturbances in the generation of electricity from solar cells. Of course, electricity generation fluctuations from solar cells do not overlap with societal demand for the electricity. In other words, there are times when solar panels produce more electricity than is needed, and times when they drastically fall short of people's need. Thus, while the total electric energy produced over the course of a year is a reliable standard, a means of storing excess energy during high production times is necessary. Unfortunately, modern electric grids simply do not have adequate energy storage capabilities and much produced electricity—and the method/fuel used to produce it—is essentially wasted.

The other key issue is that transportation accounts for over 27% of total energy demands, and only 3.5% of energy currently used for transportation is derived from renewable sources.[2] This presents another major innovative challenge to scientists and engineers. Vehicles of the future must be powered by either electricity or by fuels

generated in a sustainable way, such as hydrogen from solar energy.[6] While a number of renewable storage options exist, the work presented here is focused on the chemistry of electrolytes for a particular energy storage device (i.e. the battery). The following section briefly reviews battery science before moving into the narrower topic of magnesium batteries in particular.

1.2 Chemical Energy Storage via Batteries

All batteries are composed of three main components, two electrodes and an electrolyte (Figure 1). The electrode where oxidation takes place during discharge is known as the anode and the electrode where reduction takes place during discharge is known as the cathode. For secondary (rechargeable) batteries the roles of the anode and cathode reverse during charging but the names remain the same, regardless of the direction of electric polarity. The electrolyte acts as a mediator for ionic movement between the two electrodes so charge conservation is satisfied.

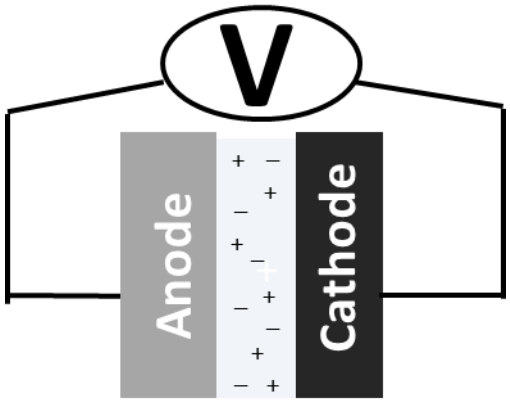

Figure 1: General schematic for an electrochemical battery cell connected to an external circuit, establishing a voltage (V) between a cathode and anode material, with electrolyte between the electrodes.

The total amount of energy a single battery cell can deliver depends on the quantity of charge each electrode is capable of holding (the electrode's capacity), as well as the difference in the respective reduction/oxidation (redox) potentials for the electrochemical processes at each electrode. The capacity of a material is given by:

$$\mathrm{Cap} = \frac{\mathrm{nF}}{\sum_i \mathrm{MW_i}} \tag{1.1}$$

Where n is the number of moles of electrons involved in the redox process and F is Faraday's constant. The denominator represents the sum of the molecular weights of each species making up the electrode material. The specific energy (SE) of a material is then defined as the product of the capacity and its standard redox potential (E°):

$$\mathrm{SE} = \frac{\mathrm{nFE^o}}{\sum_i \mathrm{MW_i}} \tag{1.2}$$

The term specific energy is sometimes used to distinguish the density of energy in the material with respect to weight, as opposed to volume—which is given the term energy density (ED). Often these two terms are used interchangeably but it should be apparent which meaning is being discussed based on context.

Another important point to make here is that the redox potential of a chemical process is not a standalone value, but must be measured with respect to a separate redox process. The most commonly used standard with which to reference redox potentials is the standard hydrogen electrode (SHE). E° values in tables are usually given with respect to this electrochemical process (being hydrogen reduction on Pt with 1 atm pressure of hydrogen bubbled through a 1N acidic solution).

So, in theory, any two different redox couples separated by an electrolyte and connected to an external circuit will drive electrical energy via an established voltage—determined by the thermodynamic difference in potentials of the redox processes. The electrolyte can be in either a liquid or solid phase, so long as it conducts ions at a useful rate. However, in practice chemistry is rarely as "clean" as the theoretical physics that governs it. If it were that simple, a battery driven by the Li/Li^+ redox couple at the anode and the $F_2/2F^-$ couple at the cathode would have been prepared long ago, as the pairing would establish the highest conceivable voltage—and energy density—naturally available.

While the difficulties with preparing a theoretical battery using Li and F_2 might be fairly apparent, some chemical systems that appear more readily achievable have proven

to be quite elusive over the decades. For instance, Li metal holds the highest theoretical specific energy of any known substance and has therefore been an explored candidate for use as the anode of rechargeable batteries for over 4 decades.[7,8] Unfortunately, no one has been able to work around the issues plaguing Li/Li^+ electrochemistry for rechargeable applications; namely, the facts that highly reactive Li metal continually degrades electrolytes upon consecutive cycling and dendritic growth of deposits have been known to cause severe safety hazards. Challenging chemistry like that in the Li metal system has prevented battery technology from taking a trajectory analogous to that of Moore's law for integrated circuits.[9] Rather than steady exponential growth, from simply miniaturizing device components, improvements in battery technology requires discovery of new chemistries, followed by improvements on those systems (see Figure 2 in reference 10 for a nice historical layout of secondary battery technology).[10] Thus, battery technology is often improved in quantum leaps. Many in the field hope the next jump is just around the corner.

The biggest breakthrough in modern energy storage came when the Sony Corporation invented the first Lithium-Ion (Li-ion) battery in 1991. This device revolutionized the portable technologies industry. Coupled with the $LiCoO_2$ cathode material, discovered by Goodenough *et al.*[11] a decade before, graphite showed the ability to reversibly intercalate Li^+ at the anode with high efficiency and excellent cycle stability. By swapping Li metal for LiC_6, Li-ion cells are able to avoid the pitfalls associated with Li electrodeposition.[7]

While the achievement of the Li-ion battery should in no way be downplayed, it is disappointing that 24 years later state of the art Li-ion batteries use the same chemistry. However, it has been pointed out that since the 1950s each battery system experiences steady growth rates for 20–30 years before the next chemistry is developed.[10] With this trend in mind, one might optimistically presume that we are currently on the verge of the next big breakthrough. A fundamental limit for Li-ion cells is quickly being approached and, for reasons discussed above, a strong push is being made to create batteries with new—game changing—chemistry.

1.3 Beyond Li-ion and The Case for a Magnesium Battery

Table 1: Anode materials compared. SCap and VCap are the specific and volumetric capacities, respectively. SE and ED are the specific energies and energy densities, respectively. Molalities (moles of substance per kg of earth) are expressed with respect to lithium, which is normalized at 1, and were taken from the CRC Handbook of Physics and Chemistry.[15] Costs were estimated from prices for pure materials.[72–77]

Anode	SCap Ah/kg	VCap Ah/L	SE Wh/kg	ED Wh/L	Molality w.r.t. Li	Cost $/kg	$/kWh
LiC_6	372	819	1116	2458	5	69	68
Mg	**2205**	**3832**	**5226**	**9082**	**333**	**37**	**7**
Li	3862	2062	11779	6290	1	270	23
Zn	820	5854	625	4459	0.4	53	85
Al	2980	8046	4953	13372	1058	16	3
Ca	1337	2073	3836	5946	359	200	52

As Li-ion batteries quickly approach their theoretical limit, scientists and engineers have turned to chemistries theoretically capable of outperforming today's standard. Although intercalation of Li^+ ions into graphite occurs at a potential close to that of pure Li—allowing similar voltages between anode and cathode to be achieved—the capacity of the anode is severely limited by the added weight of the host carbon material. Extra weight is also present from the binding polymer, used for cheap assembly, and conductive carbon black additive. With the capacity loss from non-active electrode components in mind it is easy to see why pure materials, like metals, are so attractive. An electrode composed solely of a metal operates by simply depositing the metal from ions in solution, during charging, and stripping the metal, in the form of its constituent ions, back into the electrolyte upon discharge. No host material is necessary for metal plating,

nor is there a need for any binding material or conductive additive. For these reasons, many researchers have reinitiated work on Li metal. However, despite considerable progress, safety concerns and electrolyte decomposition reactions continue to plague Li metal anodes.[7]

Alternative metals have naturally been proposed, particularly attractive are multivalent metals which transfer more electrons per formula unit of active material.[12,13] Table 1 compares some of the more attractive metals in terms of important material features such as their specific energy, energy density, and cost per unit energy. An attractive alternative to Li as an anode material is magnesium metal; the reasons for this are apparent in table 1. The theoretical limit for magnesium's specific energy is over 4.6 times that of graphite Li-ion intercalation anodes. Perhaps more important is the energy density (volumetric), which is actually greater than that for Li metal. Mg is also cheaper, being far more abundant than Li in Earth's crust and ocean waters.[14,15] Finally, Mg-based batteries are expected to be much safer than Li-based systems due to a lack of evidence suggesting dendritic growth when undergoing Mg deposition/stripping cycles.[12] Also, unlike Li, Mg metal is not violently reactive when exposed to air and water. In the following section a brief review of electrolytes for Mg batteries is given. It is noted that progress on Mg batteries has been hindered by both a lack of adequate electrolytes and a lack of high performing cathode materials. However, the focus of this thesis work was on electrolyte systems so a review of cathode materials will not be given here. The interested reader is instead referred to the literature for reviews of Mg cathode candidates.[16,17]

1.3.1 Magnesium Electrolytes

For Mg batteries the proper choice of electrolyte is key. It is well recognized that simple magnesium salts in typical aprotic organic solvents are not compatible with Mg anodes (i.e. they do not allow any reversible electrodeposition of Mg).[18,19] Extensive work in the past has shown that highly reactive Mg metal decomposes common electrolyte components that consequently form insulating passivation films on the metal's surface.[18–20] On the other hand, despite being even more reactive than Mg, Li metal will allow reversible electrodeposition from several Li-salt/aprotic-solvent electrolytes (with varying degrees of efficiency) because Li^+ ions are able to conduct through the formed passivation layers where Mg^{2+} simply cannot. It is also stressed that atmospheric contaminants are detrimental to reversible Mg electrodeposition.[19] So, for a Mg electrolyte to perform well it must prevent passivation layers from forming on the surface of a Mg anode. The following sections provide highlights of Mg electrolytes discussed in the literature that allow reversible electrodeposition of Mg. This is by no means a comprehensive review as several very good reviews on the subject are found in the recent literature.[12,13,21–24,17]

A. Grignard Reagents (RMgX)

The first electrolytes that showed an ability to reversibly electrodeposit Mg were organometallic Grignard reagents in ether solvents, usually THF.[25–33] It was actually discovered that Grignards could electrodeposit Mg in 1927, but only a few articles were written on the subject prior to the 1990s. The Aurbach group, recognized leaders in the

field, performed a number of important experiments with an aim of understanding the underlying mechanism for the reversible deposition process.[19,31,32,34–37] Specifically, in-situ characterizations, like use of an electrochemical quartz crystal microbalance (EQCM) and spectroelectrochemical FTIR, revealed that the Mg electrodeposition and stripping processes are complex in nature. Rather than simple reduction of Mg^{2+} to Mg^0, it was suggested that electron transfer to RMg^+ produces $RMg^{\bullet}_{(ad)}$. This is accompanied by complex adsorption routes in which species containing C-Mg bonds bind to the surface and finally leave Mg adatoms behind. Furthermore, electrochemical impedance spectroscopy (EIS), SEM images, and EDS spectra revealed a porous deposit composed of Mg, C, and halide components for the initial layers, followed by compact Mg when the layer of deposit was > 400mC/cm^2. The importance of these studies cannot be overstated as they laid a strong foundation for understanding unique electrochemical behavior for working Mg electrolytes.

B. Magnesium Borates

In 1990 Gregory *et al.* published some of the first work to look extensively and exclusively at electrolytes with Mg batteries in mind.[30] In their work Mg dissolution tests were conducted with several tetrabutyl ammonium salts in THF to assess the stability of prospective anions in the presence of Mg. They found that all complex fluoride anions could be ruled out, likely due to formation of MgF_2 on the Mg surface. They also ruled out Br_3 and ClO_4^- as they reacted with organomagnesium species. One major conclusion of the Gregory *et al*. work was that only Mg compounds showing a high degree of covalency allowed reversible Mg electrodeposition to occur. In fact, until the Mohtadi *et*

al. $Mg(BH_4)_2$ study in 2012 the general consensus was that inorganic Mg salts were to be more or less ruled out.[35,38] Magnesium plating experiments found organoborates to be the only suitable anions among those tested. This prompted them to test a full cell using $Mg(Bu_2Ph_2)_2$ and a Co_3O_4 cathode (which showed good intercalation kinetics). A deposition/dissolution efficiency of 99% was measured after 4 cycles, but the cell ultimately suffered from the lack of oxidative stability of the electrolyte.

Following Gregory's work, a number of borate based Mg salts were screened by the Aurbach group and found to generally have poorer cycling efficiencies and lower oxidative stabilities than their aluminate counterparts.[35] More recently boron based compounds have generated some renewed interest due to the very high oxidative stability found for tris(pentafluorophenyl)monophenylborate anion as well as reports showing the ability for Mg organoborates derived from Lewis acid-base reactions with Grignards to reversibly electrodeposit Mg even after the solution was exposed to air.[23,39] Intriguing carborane based magnesium salts have also been reported in the recent literature.[40,41]

C. Organometallic Lewis Acid-Base Complexes

To increase the oxidative stability of organometallic based Mg electrolytes—while maintaining reversible Mg electrodeposition at the anode—$R_{2-x}MgX_x$ (x = 0 or 1) Lewis bases can be combined with $R'_{3-x}AlCl_x$ (x = 0, 1, 2, or 3) Lewis acids to obtain complexes that stabilize the R group by binding it to Al. This was first demonstrated with the dichloro complex $Mg(AlCl_2BuEt)_2$ (DCC). The DCC electrolyte was the first Mg electrolyte used to build a working prototype battery (Mo_6S_8 was used as an intercalation

cathode).[31] The next notable breakthrough came with the all phenyl complex (APC) which is a combination of PhMgCl with $AlCl_3$, usually at a 2:1 ratio of PhMgCl to $AlCl_3$. By replacing the alkyl groups with an aryl group the oxidative stability was increased significantly to approximately 3 V vs. Mg on a Pt electrode.[42] The Lewis acid-base strategy has proven very useful over the past decade. This general synthetic route has been used to create several anologues of the APC electrolyte by replacing the Mg-C bond with that of O, N, or S (i.e. ROMgCl, RNMgCl, or RSMgCl + $AlCl_3$).[43,44] Each of these iterations has been shown to give reversible Mg electrodeposition from ethereal solutions. Much more recently, fully inorganic Lewis acid-base have also been developed and may prove to be a safer way to synthetically produce Mg electrolytes with the same ideal characteristics.[45,46] Unfortunately, all of these contain halides—usually Cl^-, that have been shown to cause considerable corrosion of common battery components, such as stainless steel.[47]

D. Non-halide Containing Inorganic Magnesium Salts

Less prevalent in the literature are reports of Mg electrolytes that are capable of reversible electrodeposition but halide free. Reports of magnesium bis(trifluoromethylsulfonyl)imide ($Mg(TFSI)_2$) in glymes have shown evidence of a reversible process but with very poor cycling efficiency.[48–51] More notable is the work on $Mg(BH_4)_2$, the first all inorganic-halide free Mg salt to show reversible electrodeposition.[38,52–57] With the aid of $LiBH_4$ these electrolytes have shown extremely good coulombic efficiencies of greater than 99% in glyme based solvents. The main drawback to the BH_4^- systems is the oxidative instability of the anion. These systems are

elaborated on more in chapter 4, where $Mg(BH_4)_2$ is shown to work in combination with PEGylated ionic liquids.

1.4 Ionic Liquids for Battery Electrolytes

The entirety of the original work presented here deals with the behavior of magnesium electrolytes specifically in ionic liquid media. Thus, it is appropriate to introduce the topic of ionic liquids, especially with regard to their use in battery electrolytes. Several exceptional reviews have been written on the subject of ionic liquids and, in the interest of brevity, most of the available material is omitted from this discussion. The interested reader is encouraged to seek the cited literature sources to learn more.[58–69]

1.4.1 Classifications and General Properties of Ionic Liquids

In the last two decades, a class of liquids known as ionic liquids (ILs) has gained considerable momentum in the chemical sciences due to discovery of ionic salts with interesting properties, such as melting points (T_m) below 100°C. Melting below 100°C is generally considered the definitive trait for defining a material as an IL.[61] More useful still are ionic materials that exist in the liquid state at room temperature, sometimes specifically referred to as room temperature ILs (RTILs). Most of the ILs used in the works described here were in fact of the room temperature variety. In the interest of creating a more readable document RTILs will simply be referred to as ILs from here on.

In Angell's 2012 review four classes of ionic liquids are identified, aprotic, protic, inorganic and solvate (or chelate) ionic liquids.[67] Protic ionic liquids are essentially ruled

out from use with high voltage batteries as metals like Li and Mg operate at potentials well below hydrogen reduction. Inorganic ionic liquids are much less prevalent in the literature but are essentially extremely low melting eutectic salt mixtures. Some inorganic ILs have been attempted for Mg electrolytes but with limited success.[70,71] Solvate ILs are an interesting category in which a molecular chelating ligand is used to screen the charge from the cation and/or anion, drastically reducing coulombic interactions, and ultimately significantly reducing the melting temperature of the parent salt. These are elaborated on more in chapter 3.

Although not all encompassing, the IL class of liquids are often characterized by wide electrochemical windows, high intrinsic conductivities, high thermal stabilities, and low volatilities. All of these characteristics are desired in battery electrolytes.

1.4.2 Use of Ionic Liquids in Battery Electrolytes

For chemical reactions in general the appropriate chose of solvent(s) can be very important. When considering a solvent system for battery electrolytes the primary concern is the electrochemical window (the voltages between which reduction and oxidation of solvent molecules takes place). The electrochemical window of the solvent system must encompass the potentials at which the electrochemistry at each electrode takes place. The ideal solvent will also maximize ionic conductivity with a chosen salt solute, minimize cost, and minimize safety hazards such as flammability. Thus, the appropriate chose of ionic liquid and electroactive specie(s) could create an ideal battery electrolyte. There are numerous reports on the use of ionic liquids with Li electrolytes and many of the systems appear to have most of the desired characteristics mentioned. At

the moment, it appears ILs have not made their way into commercial battery systems due to higher synthetic costs and lower rate performances than typical organic solvent electrolytes.[69] The lower rates of charge and discharge in IL electrolytes are primarily due to the higher viscosities of these solutions, with respect to common organic solvent based systems. Despite the drawbacks of IL systems thus far, there is no reason to believe the right combination of IL and active salt species will not be discovered.

1.5 References

1. Bureau, U. S. C. U.S. and World Population Clock. 1 (2015). at <http://www.census.gov/popclock/>

2. Agency, I. E. *Key World Energy Statistics*. (2015).

3. NOAA. CO2 Now.org. 1 (2015). at <http://co2now.org/>

4. Pidwirny, M. Solar Radiation. *Encycl. Earth* 1 (2012). at <http://www.eoearth.org/view/article/156098/>

5. Budikova, D. Albedo The Encyclopedia of Earth. *Encycl. Earth* 1 (2013). at <http://www.eoearth.org/view/article/149954/>

6. Gröger, O., Gasteiger, H. a. & Suchsland, J.-P. Review—Electromobility: Batteries or Fuel Cells? *J. Electrochem. Soc.* **162,** A2605–A2622 (2015).

7. Scrosati, B., Hassoun, J. & Schalkwijk, W. A. Van. *Lithium Batteries: Advanced Technologies and Applications*. (John Wiley & Sons, 2013).

8. Aurbach, D., Zinigrad, E., Cohen, Y. & Teller, H. A short review of failure mechanisms of lithium metal and lithiated graphite anodes in liquid electrolyte solutions. *Solid State Ionics* **148,** 405–416 (2002).

9. Moore, G. E. Cramming more components onto integrated circuits. *Proc. IEEE* **86,** 82–85 (1998).

10. Zu, C.-X. & Li, H. Thermodynamic analysis on energy densities of batteries. *Energy Environ. Sci.* **4,** 2614 (2011).

11. Mizushima, K., Jones, P. C., Wiseman, P. J. & Goodenough, J. B. LixCoO2 (0<x<-1): A new cathode material for batteries of high energy density. *Mater. Res. Bull.* **15,** 783–789 (1980).

12. Muldoon, J., Bucur, C. B. & Gregory, T. Quest for Nonaqueous Multivalent Secondary Batteries: Magnesium and Beyond. *Chem. Rev.* **114,** 11683–11720 (2014).

13. Gao, X.-P. & Yang, H.-X. Multi-electron reaction materials for high energy density batteries. *Energy Environ. Sci.* **3,** 174 (2010).

14. Petersen, U. Mining the hydrosphere. *Geochim. Cosmochim. Acta* **58,** 2387–2403 (1994).

15. CRC. *Handbook of Chemistry Physics*. (2015).

16. Huie, M. M., Bock, D. C., Takeuchi, E. S., Marschilok, A. C. & Takeuchi, K. J. Cathode materials for magnesium and magnesium-ion based batteries. *Coord. Chem. Rev.* **287,** 15–27 (2015).

17. Yoo, H. D. *et al.* Mg rechargeable batteries: an on-going challenge. *Energy Environ. Sci.* **6,** 2265–2279 (2013).

18. Peled, E. & Straze, H. The Kinetics of the Magnesium Electrode in Thionyl Chloride Solutions. **834,** 1030–1035 (1977).

19. Lu, Z., Schechter, A., Moshkovich, M. & Aurbach, D. On the electrochemical behavior of magnesium electrodes in polar aprotic electrolyte solutions. *J. Electroanal. Chem.* **466,** 203–217 (1999).

20. Lossius, L. P. & Emmenegger, F. Plating Of Magnesium From Organic Solvents. *Electrochem. Acta* **41,** 445–447 (1996).

21. Bucur, C. B., Gregory, T., Oliver, A. G. & Muldoon, J. Confession of a Magnesium Battery. *J. Phys. Chem. Lett.* 3578–3591 (2015). doi:10.1021/acs.jpclett.5b01219

22. Mohtadi, R. & Mizuno, F. Magnesium batteries: Current state of the art, issues and future perspectives. *Beilstein J. Nanotechnol.* **5,** 1291–311 (2014).

23. Muldoon, J. *et al.* Electrolyte roadblocks to a magnesium rechargeable battery. *Energy Environ. Sci.* **5,** 5941–5950 (2012).

24. Park, M.-S., Kim, J.-G., Kim, Y.-J., Choi, N.-S. & Kim, J.-S. Recent Advances in Rechargeable Magnesium Battery Technology: A Review of the Field's Current Status and Prospects. *Isr. J. Chem.* **55,** 570–585 (2015).

25. Linn, C. B.; Noller, C. R. The Catalyzed Reaction of Ethylmagnesium Bromide with Ethyl Bromide. **58,** 816–819 (1926).

26. Gaddum, L. W. & French, H. E. The Electrolysis of Grignard Solutions. *J. Am. Chem. Soc.* **49,** 1295–1299 (1927).

27. Overcash, D. M. & Mathers, F. C. The Electrodeposition of Magnesium. *ECS Trans.* **64,** 305–311 (1933).

28. Evans, W. V.; Lee, F. H.; Lee, C. H. The Decomposition Voltage of Grignard Reagents in Ether Solution. *J. Am. Chem. Soc.* **57,** 489–491 (1935).

29. Connor, J. H., Reid, W. E. & Wood, G. B. Electrodeposition of Metals from Organic Solutions. *J. Electrochem. Soc.* **104,** 38 (1957).

30. Gregory, T. D., Hoffman, R. J. & Winterton, R. C. Nonaqueous Electrochemistry of Magnesium Applications to Energy Storage. *J. Electrochem. Soc.* **137,** 775–780 (1990).

31. Aurbach, D. *et al.* Prototype systems for rechargeable magnesium batteries. *Nature* **407,** 724–7 (2000).

32. Aurbach, D., Moshkovich, M., Schechter, A. & Turgeman, R. Magnesium Deposition and Dissolution Processes in Ethereal Grignard Salt Solutions Using Simultaneous EQCM-EIS and In Situ FTIR Spectroscopy. *Electrochem. Solid-State Lett.* **3,** 31–34 (2000).

33. Liebenow, C., Yang, Z., Lobitz, P., Moritz, E. & Uni, A. The electrodeposition of magnesium using solutions of organomagnesium halides , amidomagnesium halides and magnesium organoborates. 1–5 (2000).

34. Aurbach, D., Schechter, A., Moshkovich, M. & Cohen, Y. On the Mechanisms of Reversible Magnesium Deposition Processes. *J. Electrochem. Soc.* **148,** A1004 (2001).

35. Aurbach, D. *et al.* Electrolyte Solutions for Rechargeable Magnesium Batteries Based on Organomagnesium Chloroaluminate Complexes. *J. Electrochem. Soc.* **149,** A115 (2002).

36. Aurbach, D., Turgeman, R., Chusid, O. & Gofer, Y. Spectroelectrochemical studies of magnesium deposition by in situ FTIR spectroscopy. *Electrochem. commun.* **3,** 252–261 (2001).

37. Aurbach, D., Cohen, Y. & Moshkovich, M. The Study of Reversible Magnesium Deposition by In Situ Scanning Tunneling Microscopy. *Electrochem. Solid-State Lett.* **4,** A113 (2001).

38. Mohtadi, R., Matsui, M., Arthur, T. S. & Hwang, S.-J. Magnesium borohydride: from hydrogen storage to magnesium battery. *Angew. Chem. Int. Ed. Engl.* **51,** 9780–3 (2012).

39. Guo, Y. *et al.* Boron-based electrolyte solutions with wide electrochemical windows for rechargeable magnesium batteries. *Energy Environ. Sci.* **5,** 9100 (2012).

40. Tutusaus, O. *et al.* An Efficient Halogen-Free Electrolyte for Use in Rechargeable Magnesium Batteries. *Angew. Chem. Int. Ed. Engl.* 1–6 (2015). doi:10.1002/anie.201412202

41. Carter, T. J. *et al.* Boron clusters as highly stable magnesium-battery electrolytes. *Angew. Chem. Int. Ed. Engl.* **53,** 3173–7 (2014).

42. Aurbach, D. *et al.* Progress in Rechargeable Magnesium Battery Technology. *Adv. Mater.* **19,** 4260–4267 (2007).

43. Wang, F., Guo, Y., Yang, J., Nuli, Y. & Hirano, S. A novel electrolyte system without a Grignard reagent for rechargeable magnesium batteries. *Chem. Commun. (Camb).* **48,** 10763–5 (2012).

44. Bian, P., NuLi, Y., Abudoureyimu, Z., Yang, J. & Wang, J. A novel thiolate-based electrolyte system for rechargeable magnesium batteries. *Electrochim. Acta* **121,** 258–263 (2014).

45. Doe, R. E. *et al.* Novel, electrolyte solutions comprising fully inorganic salts with high anodic stability for rechargeable magnesium batteries. *Chem. Commun. (Camb).* **50,** 243–5 (2014).

46. Shterenberg, I. *et al.* Evaluation of $(CF_3SO_2)_2N^-$ (TFSI) Based Electrolyte Solutions for Mg Batteries. *J. Electrochem. Soc.* **162,** A7118–A7128 (2015).

47. Muldoon, J. *et al.* Corrosion of magnesium electrolytes: chlorides – the culprit. *Energy Environ. Sci.* **6,** 482 (2013).

48. Kitada, A. *et al.* Room Temperature Magnesium Electrodeposition from Glyme-Coordinated Ammonium Amide Electrolytes. *J. Electrochem. Soc.* **162,** D389–D396 (2015).

49. Ha, S. *et al.* Magnesium(II) Bis(trifluoromethane sulfonyl) Imide-Based Electrolytes with Wide Electrochemical Windows for Rechargeable Magnesium Batteries. *Appl. Mater. Interfaces* **6,** 4063–4073 (2014).

50. Kitada, A., Kang, Y., Uchimoto, Y. & Murase, K. Room-Temperature Electrodeposition of Mg Metal from Amide Salts Dissolved in Glyme-Ionic Liquid Mixture. *J. Electrochem. Soc.* **161,** D102–D106 (2014).

51. Fukutsuka, T. *et al.* New Magnesium-ion Conductive Electrolyte Solution Based on Triglyme for Reversible Magnesium Metal Deposition and Dissolution at Ambient Temperature. *Chem. Lett.* **43,** 1788–1790 (2014).

52. Shao, Y. *et al.* Coordination chemistry in magnesium battery electrolytes: how ligands affect their performance. *Sci. Rep.* **3,** 3130 (2013).

53. Chang, J. *et al.* Synergetic Role of Li(+) during Mg Electrodeposition/Dissolution in Borohydride Diglyme Electrolyte Solution: Voltammetric Stripping Behaviors on a Pt Microelectrode Indicative of Mg-Li Alloying and Facilitated Dissolution. *ACS Appl. Mater. Interfaces* **7,** 2494–2502 (2015).

54. Mohtadi, R. Borohydride Solvo-Ionic Liquid Family For Magnesium Battery. **1,** 1–4 (2015).

55. Su, S. *et al.* A novel rechargeable battery with a magnesium anode, a titanium dioxide cathode, and a magnesium borohydride/tetraglyme electrolyte. *Chem. Commun.* **51,** 2641–2644 (2015).

56. Tuerxun, F. *et al.* High concentration magnesium borohydride/tetraglyme electrolyte for rechargeable magnesium batteries. *J. Power Sources* **276,** 255–261 (2015).

57. Shao, Y. *et al.* Nanocomposite polymer electrolyte for rechargeable magnesium batteries. *Nano Energy* **12,** 750–759 (2015).

58. Welton, T. Room-Temperature Ionic Liquids. Solvents for Synthesis and Catalysis - Chemical Reviews (ACS Publications). *Chem. Rev.* (1999). doi:10.1021/cr1003248

59. Welton, T. & Wasserscheid, P. *Ionic Liquids in Synthesis*. (Wiley-VCH Verlag GmbH & Co., 2002).

60. Handy, S. H. Room temperature ionic liquids: different classes and physical properties. *Curr. Org. Chem.* **9,** 959–988 (2005).

61. Endres, F. & Zein El Abedin, S. Air and water stable ionic liquids in physical chemistry. *Phys. Chem. Chem. Phys.* **8,** 2101–2116 (2006).

62. Zhang, S., Sun, N., He, X., Lu, X. & Zhang, X. Physical Properties of Ionic Liquids: Database and Evaluation. *J. Phys. Chem. Ref. Data* **35,** 1475 (2006).

63. Stark, A. & Seddon, K. R. Ionic Liquids. *Kirk-Othmer Encycl. Chem. Technol.* **26,** 836–920 (2007).

64. Tsuda, T. & Hussey, C. L. Electrochemistry of Room-Temperature Ionic Liquids and Melts. *Mod. Asp. Electrochem.* **45,** 63–174 (2009).

65. Armand, M., Endres, F., MacFarlane, D. R., Ohno, H. & Scrosati, B. Ionic-liquid materials for the electrochemical challenges of the future. *Nat. Mater.* **8,** 621–9 (2009).

66. Endres, F. Physical chemistry of ionic liquids. *Phys. Chem. Chem. Phys.* **12,** 1648 (2010).

67. Angell, A. C., Ansari, Y. & Zhao, Z. Ionic Liquids: Past, present and future. *Faraday Discuss.* **154,** 9–27 (2012).

68. Fedorov, M. V & Kornyshev, A. A. Ionic liquids at electrified interfaces. *Chem. Rev.* **114,** 2978–3036 (2014).

69. MacFarlane, D. R. *et al.* Energy applications of ionic liquids. *Energy Environ. Sci.* **7,** 232–250 (2014).

70. Narayanan, N. S. V., Ashok Raj, B. V. & Sampath, S. Physicochemical, spectroscopic and electrochemical characterization of magnesium ion-conducting, room temperature, ternary molten electrolytes. *J. Power Sources* **195,** 4356–4364 (2010).

71. Venkata Narayanan, N. S., Ashok Raj, B. V. & Sampath, S. Magnesium ion conducting, room temperature molten electrolytes. *Electrochem. commun.* **11,** 2027–2031 (2009).

72. ‘Aluminum.’ Chemicool Periodic Table. 1 (2015). at <http://www.chemicool.com/elements/aluminum.html>

73. ‘Carbon.’ Chemicool Periodic Table. 1 (2015). at <http://www.chemicool.com/elements/carbon.html>

74. ‘Magnesium.’ Chemicool Periodic Table. 1 (2015). at <http://www.chemicool.com/elements/magnesium.html>

75. ‘Lithium.’ Chemicool Periodic Table. 1 (2015). at <http://www.chemicool.com/elements/lithium.html>

76. ‘Zinc.’ Chemicool Periodic Table. 1 (2015). at <http://www.chemicool.com/elements/zinc.html>

77. ‘Calcium.’ Chemicool Periodic Table. 1 (2015). at <http://www.chemicool.com/elements/calcium.html>

CHAPTER 2

ELECTROCHEMISTRY OF MAGNESIUM ELECTROLYTES IN "CONVENTIONAL" ROOM TEMPERATURE IONIC LIQUIDS

2.1 Introduction

In many high temperature halide salt melts, involving Mg halides, Mg electrodeposition and subsequent dissolution (stripping) is a chemically reversible process, and well understood.[1–4] Many fundamental characteristics of these high temperature melts have been studied, and corresponding mechanisms for the electrodeposition and stripping of Mg have been proposed. One interesting point of note is the observation that exchange current densities in $MgCl_2$-NaCl eutectics at 755°C were found to increase in correlation with the activity of $MgCl_2$, up to a 75% $MgCl_2$ composition.[2] This phenomenon was attributed to the dissociation of polynuclear $(MgCl_2)_n$ clusters by the NaCl salt; clusters that otherwise exist in the pure $MgCl_2$ melt.[2,5–7] Raman spectra for a full compositional range of the molten salt systems informed the researchers of the correlation between the physicochemical complexation of Mg^{2+} and the resultant electrochemical behavior. Similar connections between spectroscopically identified Mg complexes and their electrochemical behavior was a primary objective of this thesis work. In Chapters 3, 4, and 5 results from Raman spectroscopic investigations of Mg/IL electrolytes are discussed in detail. The identified Mg^{2+} complexes in these various IL solutions are used in part to explain the differences in observed electrochemical behavior.

In stark contrast to the facile electrochemistry of high temperature Mg salt melts, room temperature ILs—dissolving Mg salts—have not fared so well. As early as 2005 claims of "reversible" and "highly efficient" Mg electrodeposition were made in the literature.[8–10] However, these results were later disputed by multiple sources who had difficulty reproducing those findings. [11–16] Some would further point out a lack of "concrete evidence" for bulk Mg deposition.[14,16] What those first reports were able to show was the onset of faradaic processes when Mg salts were added, with respect to simple double layer charging in the IL backgrounds. They also provided SEM images and EDS spectra from deposition experiments showing Mg was at least involved in the deposition of some type of surface coating.[8–10] Yet, rather than bulk Mg deposition and dissolution, what their data more likely suggests is that a thin layer of Mg containing compounds was deposited and stripped from the surface in their experiments. This interpretation is supported by the low current densities, large over potentials for the redox processes, and acknowledged lack of ability to obtain a thick enough layer to acquire any XRD diffractogram of Mg.[17] Similar results were found for Mg/IL electrolytes in this thesis work.

In this chapter a series of experiments is described in which magnesium salts dissolved within a "conventional" ionic liquid were screened for their ability to electrochemically deposit and strip Mg metal from the surface of an electrode. The term "conventional" is by no means technical and is simply being used here to make a clear distinction between the IL systems in this chapter from those that are described in chapter 4. The PEGylated ILs of chapter 4 were designed with specific functional groups meant

to create appropriate complexation of Mg species for reversible electrodeposition. All experiments described in this chapter were performed with the N-butyl-N-methylpyrrolidinium bis(trifluoromethylsulfonyl)imide (BMPyrTFSI) IL (Figure 15 of chapter 3 shows the structure of the IL). This IL is commercially available; however, we found that synthesizing the IL ourselves was a more reliable way to obtain a highly pure liquid for electrochemical characterizations. BMPyrTFSI is commonly used in the literature for electrochemical applications due to its intrinsic conductivity of 2.2 mS/cm and wide electrochemical window (often quoted to between 3.5–5.5 V, depending on purity, electrode material used, etc.).[18] The abbreviation BMPyrTFSI is chosen here but the attentive reader should be aware that other nomenclatures, like Pyr_{14} for the cation or NTf_2 for the anion, are commonly used throughout the literature.

Prior to discussion of experimental results, a quick word is given on the importance of creating a pure environment for Mg electrochemistry to take place (section 2.2). In section 2.3 experiments are described in which electrolytes of Mg salts in BMPyrTFSI were subject to conditions resulting in highly inert environments in order to eliminate any impurities derived from the atmosphere. In section 2.4 the idea of using chelating agents to improve complexation of electroactive species is discussed, and experiments with chelating oligoether glymes are described. Finally, section 2.5 describes work exploring systems that do in fact allow reversible deposition/dissolution of Mg in the presence of BMPyrTFSI as long as an ethereal co-solvent is also present.

2.2 Considering the Importance of Purity

As mentioned in the introduction, the reversible electrochemical process of Mg deposition/dissolution is sensitive to water and other atmospheric components. For instance, water reacts readily with a pristine Mg surface to create a film of $Mg(OH)_2$ as follows:

$$Mg + 2H_2O \rightarrow Mg(OH)_2 + H_2 \quad (2.1)$$

Similarly, oxygen reacts to form MgO according to:

$$2Mg + O_2 \rightarrow 2MgO \quad (2.2)$$

Like Li, Mg has also been shown to form surface films through reactions of common aprotic solvents, like carbonates, and common salt anions, such as PF_6^- and ClO_4^-.[18] Unlike their analogous Li counterparts, these Mg compounds are ionically insulating. Therefore, creation of such films hinders the capability to deposit, and subsequently re-strip, Mg metal from an electrode's surface. Even trace levels of contaminants can lead to the formation of films that passivate the entire Mg metal surface. For example, a typical laboratory experiment is often performed with a 2 mm electrode (~0.03 cm^2) in an electrolyte volume of no less than 1 mL. To get a sense of just how dry is "dry enough" the following simple calculation may be considered to determine the rough concentration of water necessary to create a monolayer of $Mg(OH)_2$ on a 2 mm disk electrode's surface:

$$\frac{0.03\ \text{cm}^2\ \text{Electrode}}{0.001\ \text{L Solvent}} \text{x} \frac{2.3446\ \text{g Mg(OH)}_2}{\text{cm}^3} \text{x} \frac{3.65*10^{-8}\text{cm}}{\text{monolayer}} \text{x} \frac{1\ \text{mole Mg(OH)}_2}{58\ \text{g Mg(OH)}_2} \text{x} \frac{2\ \text{mole H}_2\text{O}}{1\ \text{mole Mg(OH)}_2} \approx 9 * 10^{-8}\ \text{M} \quad (2.3)$$

This is roughly 0.001 ppm H_2O in BMPyrTFSI (density 1.41 g/mL). In the calculation 2.3446 g/cm^2 and 58 g are the density and molecular weight of $Mg(OH)_2$, respectively. 3.65 Å ($3.65*10^{-8}$ cm) is the average of the a, b, and c lattice constants for the hexagonal $Mg(OH)_2$ unit cell and taken to be the estimated thickness of a single monolayer. So, while it is typically fine to prepare and conduct experiments on conventional Li electrolytes in an Ar filled glove box—with sufficiently low oxygen and water levels—this may not be the case for analogous Mg systems. Thus, only electrolytes with extremely low, or no, atmospheric contamination should be used with Mg anodes. Of course, other detrimental sources of contamination, not from atmospheric origins, should also be avoided.

With the above considerations in mind, as well as the general properties for ILs discussed in Chapter 1 (1.4), Mg/IL electrolytes were pursued. The thermal stability and non-volatile nature of many ILs makes them ideal candidates for studying electrochemistry under extremely inert conditions. High temperatures and low pressures (created from high vacuum) can be used without fear of losing the solvent to evaporation or thermal degradation. Efforts to perform cyclic voltammetry in extremely inert conditions are described below.

2.3 Experimental Methods

BMPyrTFSI was synthesized according to the guidelines of Appetecchi *et al*. with additional BMPyrI recrystallization steps prior to the metathesis reaction with LiTFSI.[21] In order to obtain the highest degree of purity, it was always necessary to use

decolorizing charcoal for at least 5 hours followed by passage through an alumina column as the final steps of the purification process. When stirring the IL with decolorizing charcoal it was best to dissolve/dilute the IL in dichloromethane or stir it neat at 50°C. The synthesized IL was found to be spectroscopically pure and background CVs were acquired for the IL alone in order to assess the "electrochemical purity." The IL was found to have a high degree of purity as no faradaic peaks were observed in CV sweeps within the electrochemical window of the IL (see CV in figure 3 for IL only).

Electrolyte solutions were prepared in an Ar filled Vacuum Atmospheres glovebox maintaining oxygen and water levels below 2 ppm. $Mg(ClO_4)_2$ (Sigma Aldrich) and $MgCl_2$ (ROC/RIC, 98+%) were dried for ≥ 24 hours using different ports of the vacuum line (0.1–0.3 mTorr) at 200°C. Similarly, $Mg(TFSI)_2$ (Strem Chemicals, 97.5%), LiTFSI (TCI, 99.95%) and BMPyrTFSI were dried at 140°C (the IL was vigorously stirred during this process). Oligoether glymes were dried over 3 Å molecular sieves for ≥ 72 hours prior to distillation with sodium and benzophenone. Karl Fischer titrations measured water content of the glymes at less than 5 ppm. For assembly of electrochemical cells materials were moved to the glovebox without breaking the vacuum seal. The Mg salts were dissolved in BMPyrTFSI in 25 mL four neck round bottom flasks, usually using 1–2 mL of volume.

Electrochemistry was conducted either in the glovebox or under dynamic vacuum at 0.1 mTorr, using CH Instruments 618 or 760 potentiostats. Similar results were often observed in either environment but vacuum experiments were more easily reproduced. All data shown in this chapter is taken from experiments under vacuum, except for the

experiments described in section 2.5. All cyclic voltammograms (CVs) were acquired with three electrode setups. The counter and reference electrodes were both flame annealed Pt wires in the vacuum cells and sometimes Mg ribbon in the glovebox experiments. Note that because Mg electrodeposition/dissolution is not a reversible process in the MgX_2/IL electrolytes, both Pt and Mg reference electrodes should be considered quarsi-reference electrodes (QRE) and are subject to some degree of potential drift. In some iterations the working electrode was a polished, sonicated, and oven dried 2 mm Pt disk (see experimental section of chapter 4 for polishing procedures) and in others it was a flame annealed Pt wire (flame annealing Pt wire is the quickest and easiest way to get a reproducibly clean and completely dry electrode surface). The geometrically projected surface areas of working electrodes were used to calculate current densities (surface areas for wires were determined by depth of immersion in solution and were typically close to the areas of the disk electrodes).

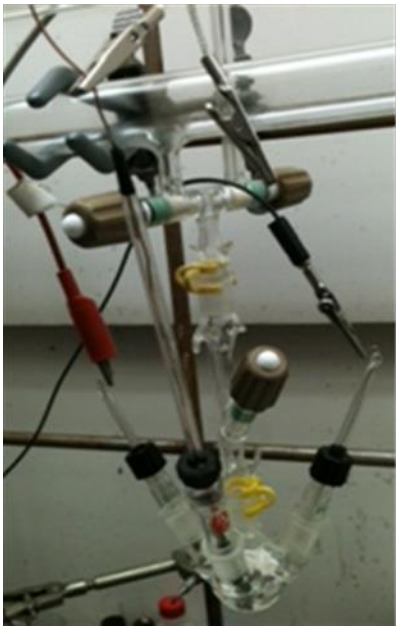

Figure 2: Picture of electrochemical cell set-up attached to the vacuum line. The cell consists of four necks, one for each electrode and one for connecting the cell to the vacuum line. Wires connecting the electrodes to the external circuit were sealed with leaded “flint” glass.

For experiments under vacuum one of the necks of the flask was attached to a Schlenk vacuum line via a greased 14/20 ground glass joint and through a Chemglass airfree Schlenk connecting adapter, as depicted in Figure 2. Three electrode setups were prepared, each electrode being connected to a copper wire that was sealed by a flint glass rod. For potential small leaks through the sealed glass, a small application of Apiezon Sealing Compound Q was applied around the sealed area. The glass rods were fitted through compression O-rings and ground glass inlet adapters to allow the electrodes access to the solution while maintaining a vacuumed seal to the outside. All ground glass joints were properly greased prior to assembly. The apparatus were moved from the glovebox to the Schlenk line without breaking seal. Dynamic pumping on the Schlenk vacuum line with a standard model 8 Edwards Vacuum Pump, aided by an additional oil

diffusion pump, achieved a pressure of 0.1 mTorr. For experiments under vacuum, cyclic voltammograms were only obtained after the solutions had been vigorously stirred under the dynamic vacuum at 140°C overnight. The validity of assuming that conditions were in fact highly inert and devoid of water was tested by quickly removing electrolyte samples from their test cells and dispensing them in a Karl Fischer titrator. Water levels were found to be below the detection limit of the instrument (nominally 1 ppm).

2.4 Cyclic Voltammetry of MgX_2 ($X = TFSI^-, ClO_4^-$) Salts in BMPyrTFSI

As alluded to in the introduction of this chapter, past reports of "reversible" Mg electrodeposition showed CVs with current densities on the order of hundreds of $\mu A/cm^2$ for the anodic stripping peaks. Some voltammograms in those reports look similar to CVs acquired for the work presented in this subsection. As discussed above, CVs in this work were acquired under dynamic vacuum in an attempt to remove all water from the electrolyte. Figure 3 shows a typical CV of a Mg/IL electrolyte under 0.1 mTorr pressure at RT. Although $Mg(TFSI)_2$ was the salt used in this particular experiment, no noticeable difference was observed for $Mg(ClO_4)_2$-based electrolytes ($MgCl_2$/IL electrolytes did not reproduce the same, or any, redox peaks). While the currents and general wave forms for the faradaic processes observed in Figure 3 are representative of most tested samples, it is noted that slight variations in peak behavior for cathodic and anodic processes were observed. For instance, some experiments showed successive increases—to a limit—for the anodic peak current upon consecutive CV cycles after first immersion of the working electrode. This increasing peak behavior was attributed to an electrochemical surface cleaning process on the electrode.

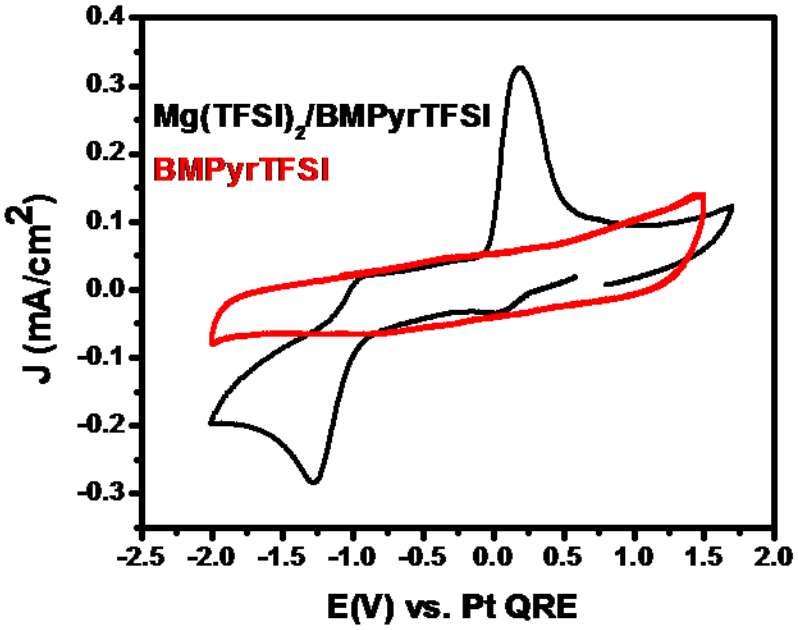

Figure 3: CV of 0.3 M $Mg(TFSI)_2$ in BMPyrTFSI (black), along with a background scan of BMPyrTFSI only (red). CVs were acquired using a Pt disk electrode and Pt wire reference and counter electrodes. The scans were acquired under 0.1 mTorr dynamic vacuum at rates of 200 mV/s.

An important observation is that the anodic peaks of the MgX_2/IL electrolytes were always symmetric like the one observed in Figure 3. Symmetric anodic peaks like this are indicative of electrochemical dissolution of a surface species from the electrode, as opposed to diffusion limited processes that should show an asymmetric diffusion wave as the potential is swept more positive.[22] Thus, it is likely that the faradic currents observed in the MgX_2/IL electrolytes were in fact from deposition and subsequent dissolution of a surface film. However, integrations of the anodic current peaks found charges on the order of hundreds of $\mu C/cm^2$. The charge density associated with a single monolayer of Mg metal is 480 $\mu C/cm^2$. Experiments were also conducted in which CVs were paused for varying lengths of time, at potentials where deposition was presumed to

take place, before allowing the cycle to resume from the paused potential (Figure 4). For potential holds of up to 80 seconds an increase in the anodic peak was observed. Longer holds did *not* continue to give rise to greater currents.

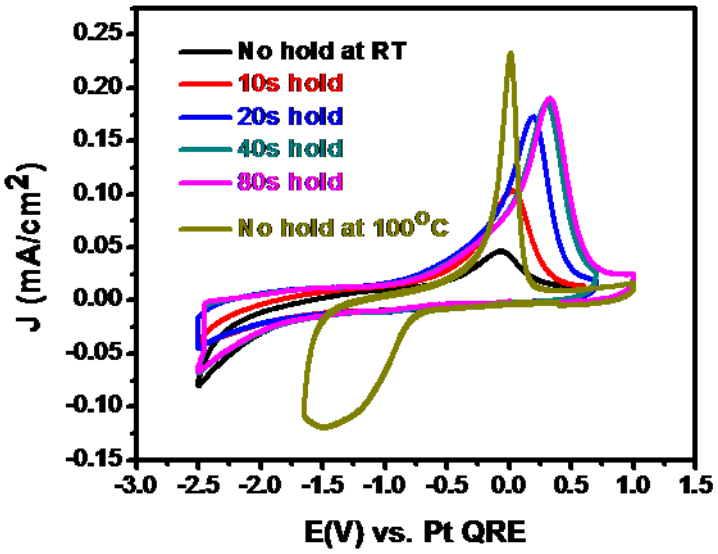

Figure 4: CVs from the same 0.1 M $Mg(TFSI)_2$/BMPyrTFSI electrolyte on a Pt wire working electrode. The CVs are presented in chronological order as a regular voltage sweep taken to a cathodic limit of –2.5 V at 200 mV/s (black) followed by consecutive 200 mV/s sweeps in which the potential was held around –2.5 V vs. a Pt QRE for 10s (red), 20s (blue), 40s (green), and 80s (pink), all at room temperature. Finally, another regular CV taken to a cathodic limit of –1.8 V but at 100°C is shown (gold).

The largest measured currents from the longer hold times were found to have charge densities of only ~1400 $\mu C/cm^2$. Therefore, the data suggests that the observed currents were from extremely thin deposits of Mg (1–3 monolayers). Furthermore, the difference between the potentials of the respective redox processes is about 1.5 V, meaning a large overpotential was required for at least one of the redox processes. Potential differences very close to this value have been measured for the electrochemical

dissolution of Mg electrodes in several aprotic organic electrolytes of MgX_2 salts (X = BF_4^-, ClO_4^-, $SO_3CF_3^-$, PF_6^-, etc.).[19] Together, these results are indicative of formation of a semi-passivated thin deposit capable of being electrochemically dissolved with a large over potential required for the stripping process.

Figure 4 also compares the RT holding scans with a CV acquired at 100ºC. While increasing the temperature did significantly reduce the overpotentials associated with deposition and stripping, true bulk/thick deposits were still elusive at the potentials scanned in the figure.

An SEM image of a potentiostatic deposition, conducted at –2 V vs. a Pt QRE, clearly displays a non-uniform thin deposit not indicative of a metallic layer (Figure 5). EDS elemental analysis showed the presence of Mg but that much higher levels of C, O, and F were also present. This result is consistent with the experimental findings of Howlett *et al.* who showed that the $TFSI^-$ anion is actually reduced at potentials positive to that of Mg^{2+} reduction.[16] Several reductive decomposition pathways were proposed, one of them resulting in the fragmentation of CF_3^- groups. Furthermore, the calculations of Rajput *et al.* predicted a significant weakening of the C-S bond of $TFSI^-$ under ion paired (Mg^+-$TFSI^-$) charge transfer conditions.[23] Thus, the composition of the deposit in Figure 5 can be attributed to the decomposition of $TFSI^-$ as Mg^{2+} is reduced. An electrochemical quartz crystal microbalance (EQCM) was used in an attempt to quantify the mass change on the electrode during the redox processes. Unfortunately, the relatively high viscosity of the solutions and the complicated adsorption and double layer

phenomena of ionic liquids convolutes the data, making it nearly impossible to evaluate.[24]

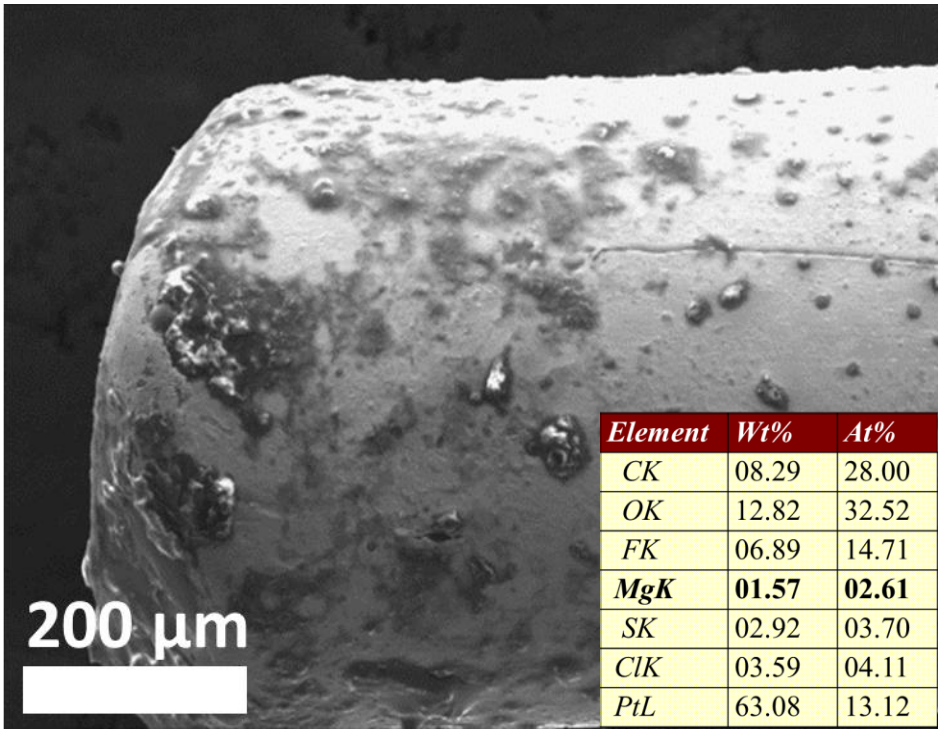

Element	Wt%	At%
CK	08.29	28.00
OK	12.82	32.52
FK	06.89	14.71
MgK	**01.57**	**02.61**
SK	02.92	03.70
ClK	03.59	04.11
PtL	63.08	13.12

Figure 5: SEM image from a 30 minute potentiostatic deposition from a 0.2 M $Mg(ClO_4)_2$/BMPyrTFSI electrolyte, conducted at –2V vs. a Pt QRE. Results from EDS elemental analysis are shown in the inset table.

A CV acquired at room temperature and taken to more negative potentials is shown as a blue trace in Figure 6. Negative of –2.5 V vs. the Pt QRE a faradaic process is turned on and much greater currents are observed than those shown in the previous figures. However, the anodic peak at ~0.0 V was no longer observed when potentials were swept to the point where the larger cathodic currents were observed. The red trace in Figure 6 is from the same experiment described in Figure 3. Both MgX_2/IL CVs are compared against a 0.1 M LiTFSI/IL electrolyte in the figure (black trace). LiTFSI gave rise to clearly reversible deposition/dissolution events, at far greater current densities,

with little overpotential. The difference in potentials for the cathodic currents in the Li and Mg (blue trace) systems (~700 mV) suggests that the cathodic current, negative of –2.5 V, in the MgX_2/IL electrolyte can be attributed to bulk Mg deposition.

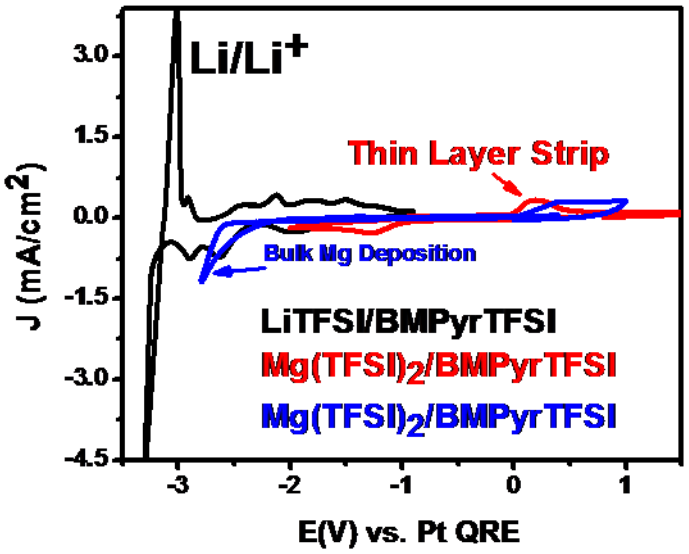

Figure 6: CVs for LiTFSI/BMPyrTFSI (black) and $Mg(TFSI)_2$/BMPyrTFSI (both red and blue) acquired at 200 mV/s on Pt disk working electrodes.

While the above results do appear to tell the story for simple MgX_2/IL electrolytes, it should be noted that when great care was taken to ensure a clean electrode, and extremely dry electrolyte, the result shown in Figure 7 could be obtained. Figure 7 shows a CV acquired under vacuum at 100°C, in which a stripping wave is observed, presumably from a bulk Mg layer. The coulombic efficiency (CE) of the deposition/dissolution process was only 20%. Despite the low CE the observed anodic stripping peak is an interesting result, as this kind of stripping current had not been observed previously. However, it is not clear yet what exactly prevents at least some of the film from being passivated in a way that is observed in RT experiments. It may be

due to a complete removal of water at the temperature and pressure in which the experiment was conducted. It is also possible that the increased temperature "weakens" any passivated layer due to increased solubility of the formed Mg containing compounds. Either way, beyond an interest in the fundamental science of the phenomenon, the point may be moot as subsequent cycles were found to show traces like the blue CV in Figure 6.

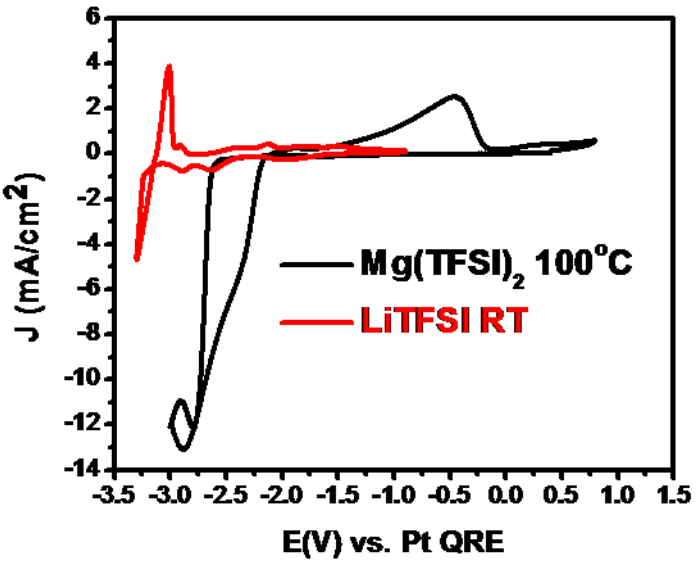

Figure 7: CVs comparing 0.1 M $Mg(TFSI)_2$/BMPyrTFSI at 100°C (black) to that of 0.1 M LiTFSI/BMPyrTFSI at room temperature (red).

Ultimately the take home message from all these experiments is that simple MgX_2/IL electrolytes suffer due to properties intrinsic to the electrolytes themselves, as opposed to trace impurities from outside sources. From observations of the above results, and the mentioned predictions of Rajput *et al.*[23], in mind the following section discusses exploration of chelating oligoether glymes added to the MgX_2/IL electrolytes in an attempt to remove $TFSI^-$ from the Mg^{2+} coordination shell.

2.5 Use of Chelating Agents

Oligoether glymes are well known chelating agents and have been used throughout the Li electrolyte literature to create $LiGm^+$ (Gm = oligoether glyme where m – 1 denotes the number of ether oxygens in the polyether chain) complexes in attempts to create species with improved electrochemical characteristics.[25] An analogous strategy is used here in the MgX_2/IL systems. Some authors have shown bulk deposition/dissolution of Mg to be possible in $Mg(TFSI)_2$/glyme systems, albeit with high overpotentials, low CE, and poor cycling performance.[26–29] Raman spectroscopic data discussed in chapter 3 informed decisions on the use of glymes within the MgX_2/IL systems. It was found that addition of 1 equivalent of triglyme (G3) or tetraglyme (G4) to that of $Mg(TFSI)_2$ created complexes of Mg^{2+} mostly free of coordination with $TFSI^-$.[30] In other words, $Mg(Gm)^{2+}$ species could exist in place of $Mg(TFSI)_3^-$ complexes. A representative CV for a glyme chelated system is shown in red in Figure 8. In this particular case 1 equivalent of G3 was added to a $Mg(TFSI)_2$/IL solution. The CV for the chelated system is compared against the equivalent non-chelated $Mg(TFSI)_2$/IL electrolyte at RT. The result is intriguing as bulk depositon and dissolution currents were observed on the first cycle, even at RT. However, much like the high temperature experiment of Figure 7, subsequent cycles suggested that passivation of the electrode quickly took place.

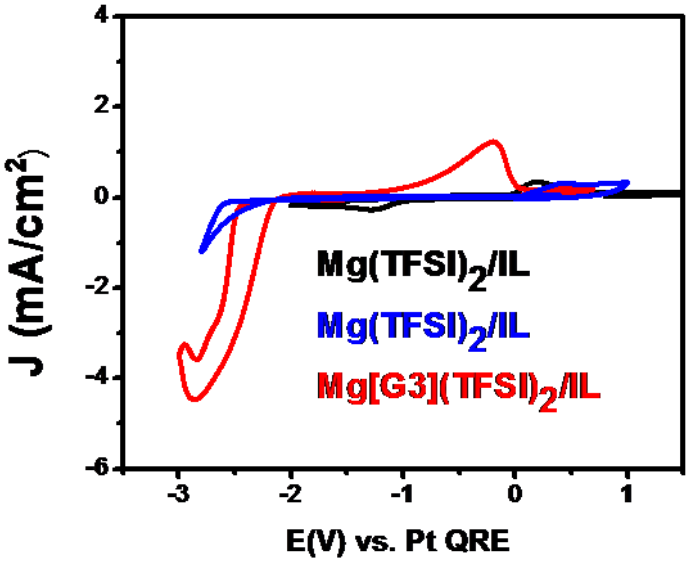

Figure 8: CVs of $Mg(TFSI)_2$/BMPyrTFSI taken to –2 V (black) and –2.8 V (blue) and $Mg[G3](TFSI)_2$/BMPyrTFSI (red). Each CV was acquired on a Pt wire working electrode at 200 mV/s.

To ensure the problem was not from the cation of the IL, efforts were made to create solvate ILs analogous to those reported on by the Watanabe group for Li(Gm)TFSI systems.[25,31–36] It was found that $Mg(Gm)(TFSI)_2$ solvate ILs were in fact possible to form (supported by Raman in chapter 3) that melted at temperatures above 70°C. A representative CV of these systems is shown in Figure 9 for the $Mg(G3)(TFSI)_2$ electrolyte. Again, CE was poor and elemental analysis from EDS spectra of a deposit from this electrolyte showed a significant amount of carbon in the deposit, presumably from glyme decomposition. Furthermore, CVs were run on solvate IL mixtures of Li(G4)TFSI and $Mg(G4)(TFSI)_2$ at 80°C. The results are shown in Figure 10. The black trace in the figure is for Li(G4)TFSI only and shows a high degree of reversibility for Li deposition/dissolution. The red trace is a 90% Li(G4)TFSI and 10% $Mg(G4)(TFSI)_2$ and the blue trace is from a 20% $Mg(G4)(TFSI)_2$ mixture. What is readily apparent from

these data is that not only is there not an obvious Mg deposition/dissolution process, but that when Mg and Li are presumably co-deposited in these systems the passivation layers of Mg deposits shut off the Li electrochemistry as well as the Mg electrochemistry. This is a similar result to that of Shimamura *et al.* who showed suppression of Li deposition in the presence of Mg^{2+} in an IL solution.[14] These results further support the notion that $TFSI^-$ decomposition is detrimental to the reversible Mg/Mg^{2+} redox process.

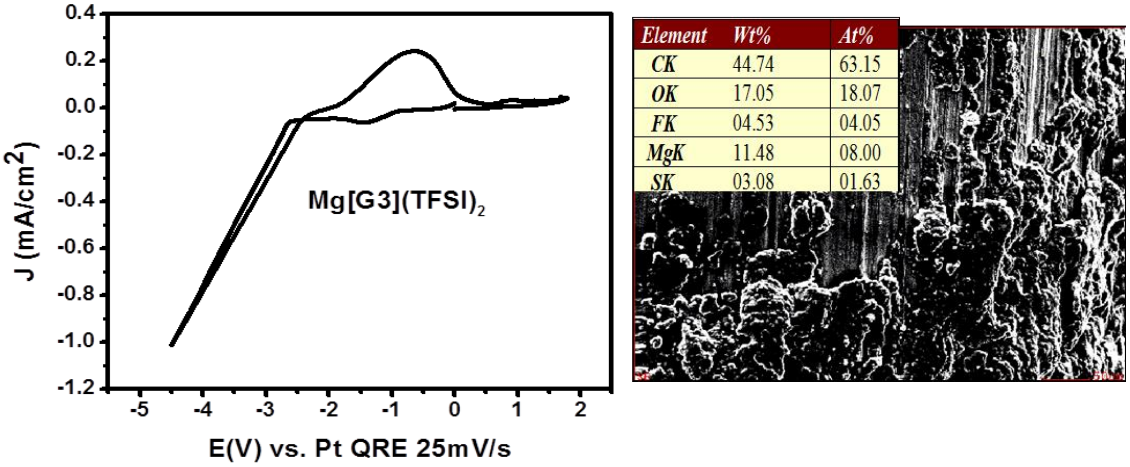

Figure 9: CV of the $Mg[G3](TFSI)_2$ solvate IL taken at 85°C (left) and the SEM image from a 15 minute deposition on a Pt wire at –3.5 V (right). The inset to the SEM image gives the elemental composition as determined via EDS.

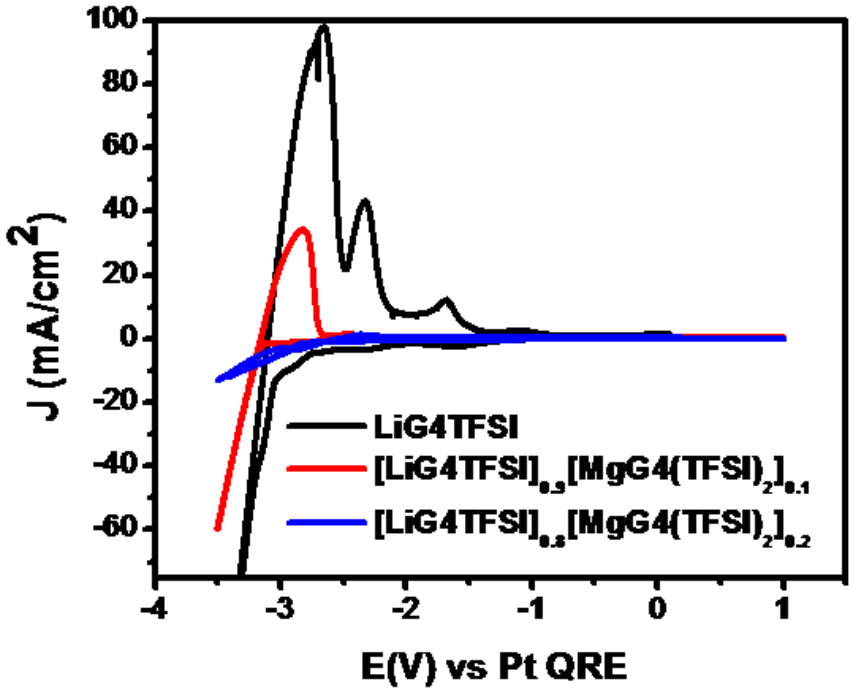

Figure 10: CVs of Li[G4]TFSI + Mg[G4](TFSI)$_2$ mixtures (black = 100% Li[G4]TSI, red = 90% Li[G4]TFSI and blue = 80% Li[G4]TFSI). CVs were acquired at 100 mV/s.

2.6 Organometallic and Mg(BH$_4$)$_2$ Mg sources aided by ethereal co-solvents

Finally, attention was turned to Mg sources known to give reversible electrodeposition. Previous work has shown that Mg can be reversibly deposited in IL electrolytes when Grignard reagents are used. However, what is not always emphasized is that the reversible redox process is only possible when an ethereal co-solvent, like THF, is present. Figure 11 compares a 0.25 M EtMgBr solution in which the solvent is a 4:1 ratio of IL to THF. This is compared against the data from Figure 3 (red trace). Clearly, the Grignard shows a highly reversible electrodeposition and dissolution process; this

was confirmed via XRD of a deposit from this system. This result is intriguing as it demonstrates a true ability to reversibly electrodeposit Mg from an IL medium as long as the "appropriate" conditions are met. On the other hand, Figure12 indicates that those conditions are only met when THF is present to some degree as a co-solvent in the system. The experiment in Figure 12 was conducted by first acquiring a CV of the Grignard solution under normal (Ar atmosphere) conditions. After the initial scan, vacuum was pulled on the system for increasing lengths of time, as indicated in the plots. Obviously, applying a vacuum to the sample removed THF via evaporation so that greater lengths of pumping time meant less THF in the solution. Apparent in the data is that systematic removal of THF led to greater overpotentials and reduced currents until no anodic wave was observed, when all the THF had been removed. Importantly, it was found that re-addition of THF to the electrolyte reproduced the reversible deposition/dissolution currents. The reproduction of redox behavior upon re-addition of THF signifies that the Grignard was not simply decomposed when THF was removed in the first part of the experiment, but instead was forced into a speciation not compatible with reversible electrodeposition. This is unfortunate because volatile solvents like THF can present safety hazards in batteries.[37] A similar result was observed using the APC electrolyte (2-1 PhMgCl-$AlCl_3$), except that the APC electrolyte did show reversible behavior without THF when a saturated APC/IL solution was heated to 55°C (Figure 13). Heating the EtMgBr/IL solution, on the other hand, did not give rise to reversible behavior. The origin of the improved reversibility upon heating for the APC electrolyte is

not yet fully understood, but is again thought to be associated with the formation of a more favorable electroactive Mg species being formed in the warmer solution.

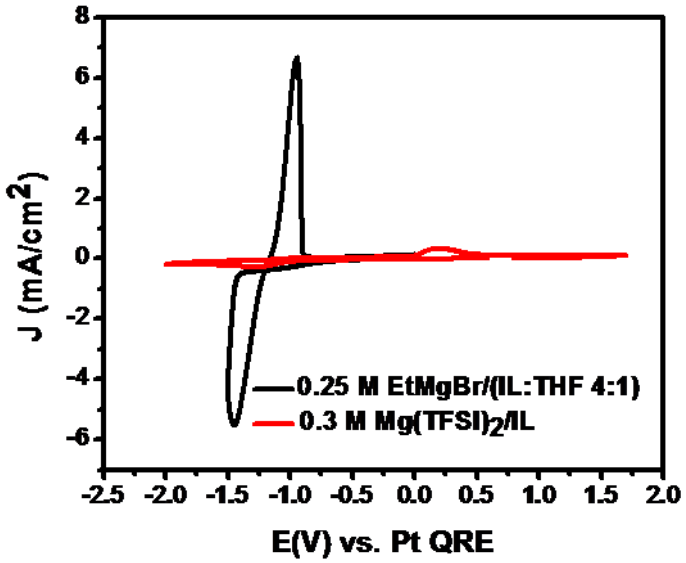

Figure 11: CV of 0.25 M EtMgBr in a solution of BMPyrTFSI and THF with a volume ratio of (4:1 IL:THF). The EtMgBr CV is compared to a 0.3 M $Mg(TFSI)_2$/BMPyrTFSI electrolyte acquired in a similar voltage range (red). Each scan was acquired on a Pt disk electrode at 200 mV/s.

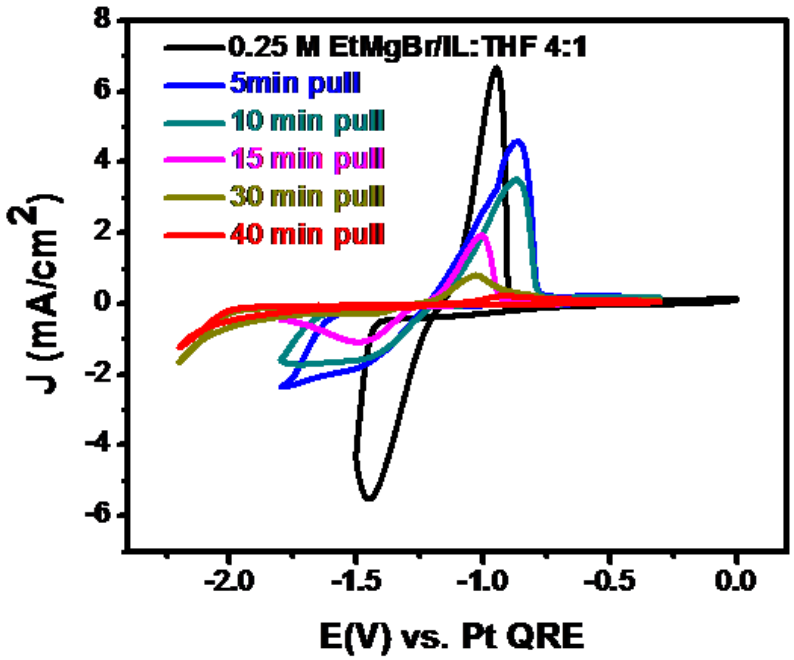

Figure 12: CVs of 0.25 M EtMgBr in a solution of BMPyrTFSI and THF with a volume ratio of (4:1 IL:THF) (black), followed by subsequent removal of THF indicated in the figure by lengths of time applying dynamic vacuum to the system.

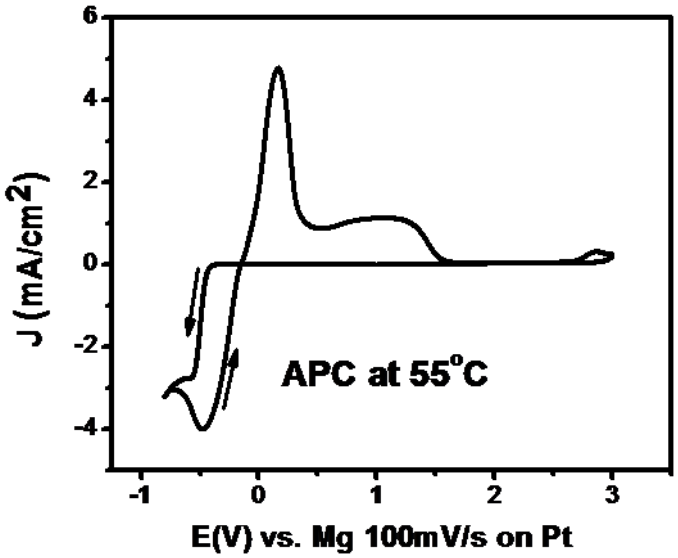

Figure 13: CV of a saturated 2-1 APC/BMPyrTFSI solution at 55°C.

One other Mg electrolyte system discussed recently in the literature—$Mg(BH_4)_2$—was tested in the BMPyrTFSI IL. $Mg(BH_4)_2$/IL systems are discussed with extensive detail in chapter 4. However, not presented in chapter 4 is the result shown in Figure 14. 10 consecutive CV cycles are shown for a 1 M $Mg(BH_4)_2$/IL electrolyte in which 2 molecular equivalents of G4 were added, with respect to $Mg(BH_4)_2$. Each cycle showed a CE of around 97%. This efficiency is far greater than efficiencies reported for $Mg(BH_4)_2$/glyme electrolytes without the aid of $LiBH_4$ as a co-electrolyte.

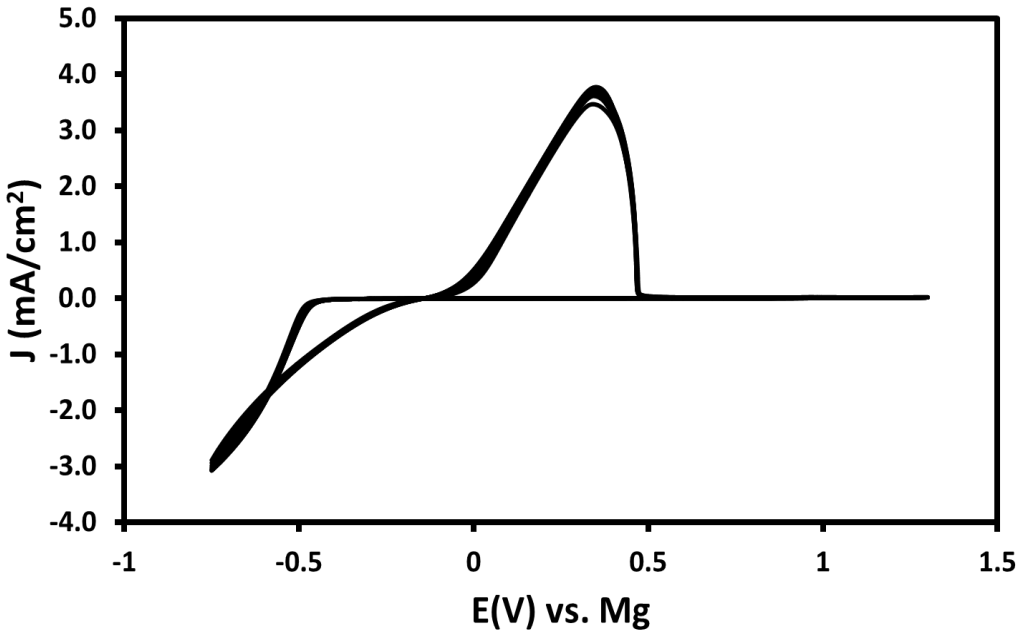

Figure 14: CV of 1 M $Mg(BH_4)_2(G4)_2$/BMPyrTFSI acquired on a 3 mm Pt disk at 25 mV/s.

2.7 Conclusions

Although the electrochemistry of the MgX_2/IL electrolytes can seem frustratingly complex at times, some important conclusions can be drawn from the results discussed above:

First, the low current density faradaic processes observed in figure 1 and 2 should not be associated with bulk Mg deposition. Simple integrations of the peaks to obtain charge values should make this obvious. Also, SEM images, EDS spectra, and a lack of XRD data further disprove the hypothesis that pure Mg metal electrodeposition can be attributed to the redox peaks.

Second, water and other atmospheric contaminants are not the sole issue with respect to poor electrochemistry in the MgX_2/IL electrolyte. $TFSI^-$ clearly decomposes during the Mg deposition process in simple MgX_2/IL electrolytes. Likely explanations come from the works of MacFarlane *et al.* and Rajput *et al.* which showed $TFSI^-$ to be less reductively stable than previously assumed, and especially unstable when complexed with Mg^{2+} and/or the short lifetime Mg^+ species.[16,23] An alternative anion for ILs that would not cause this problem is not obvious as of yet. Removal of $TFSI^-$ from the Mg^{2+} solvation shell is the best explanation for the moderately improved performance upon addition of glyme chelators. However, the glyme systems may not be able to fully prevent $TFSI^-$ contact with Mg and thus $TFSI^-$ is still subject to conditions that lead to the anion's decomposition.

It should also be noted that other water and contaminant removing strategies were briefly attempted in this work. For instance, a thin cell with a secondary sacrificial electrode was designed and used in this work but was not found to improve the Mg electrochemistry. The idea behind the thin cell can be quickly understood by a close look at the variables in equation 3. By simply increasing the surface area of the working electrode—or using a secondary sacrificial electrode—and/or using smaller volumes of electrolyte makes the concentration of water required to form a monolayer of $Mg(OH)_2$ higher. This fact is conceptually the same for any unwanted contaminant that may passivate or otherwise interfere with the electrode surface for any redox system. To this end, some researchers in the field stress the use of thin cells with limiting volumes of electrolyte in order to maximize the ability to electrochemically remove contamination

with sacrificial electrode surface. Attempts were also made to use chemical water scavenger additives like N,N-diethylaminotrimethylsilane (DEATMS), tirfluoroacetic anhydride (TFAA), and $TiCl_4$. Again, no noticeable improvement on the electrochemistry in the IL electrolytes was observed with water scavengers.

Third, reversible electrodeposition of Mg is possible in an IL-based solvent, as long as an ether co-solvent is used to solvate a Mg electrolyte known to prevent passivation of the Mg metal surface. This is not the first report of such an observation but only a few have made a point to emphasize the need for the ether solvent.[37] The emphasis on the presence of an ether co-solvent is important because it informs the researcher that $TFSI^-$-based ILs alone do not provide an appropriate solvation environment for reversible Mg/M^{2+} electrochemistry to take place; not even with Mg salts known for showing highly reversible electrochemistry in ethereal solvents. This point is explored in greater depth in chapter 4 where polyethylene glycol chains pendent from the pyrrolidinium cation were able to chelate $Mg(BH_4)_2$ in such a way as to create an electroactive species capable of reversible Mg electrodeposition from a purely ionic liquid medium.

Many of the results presented in this chapter—as well as the questions and ideas arising from these results—led to the findings discussed in chapters 3, 4 and 5.

2.8 References

1. Kisza, A., Kaźmierczak, J., Børresen, B., Haarberg, G. M. & Tunold, R. Kinetics and mechanism of the magnesium electrode reaction in molten magnesium chloride. *J. Appl. Electrochem.* **25,** 940–946 (1995).

2. Kisza, A., Kazmierczak, J., Borresen, B., Haarberg, G. M. & Tunold, R. Kinetics and Mechanism of the Magnesium Electrode Reaction in Molten MgCl2-NaCl Binary Mixtures. *J. Electrochem. Soc.* **144,** 1646 (1997).

3. Borresen, B., Haarberg, G. M. & Tunold, R. Electrodeposition of magnesium from halide melts-charge transfer and diffusion kinetics. *Electrochem. Acta* **42,** 1613–1622 (1997).

4. Martínez, a. M., Børresen, B., Haarberg, G. M., Castrillejo, Y. & Tunold, R. Electrodeposition of magnesium from the eutectic LiCl-KCl melt. *J. Appl. Electrochem.* **34,** 1271–1278 (2004).

5. Balasubrahmanyam, K. Raman Spectra of Liquid MgCl2 and Liquid MgCl2[Single Bond]KCl System. *J. Chem. Phys.* **44,** 3270 (1966).

6. Maroni, V. A., Hathaway, E. J. & Cairns, E. J. Structural Studies of Magnesium Halide-Potassium Halide Melts by Raman Spectroscopy. *J. Phys. Chem.* **75,** 155–159 (1969).

7. Capwell, R. J. Raman spectra of crystalline and molten MgCl2. *Chem. Phys. Lett.* **12,** 443–446 (1972).

8. NuLi, Y., Yang, J., Wang, J., Xu, J. & Wang, P. Electrochemical Magnesium Deposition and Dissolution with High Efficiency in Ionic Liquid. *Electrochem. Solid-State Lett.* **8,** C166 (2005).

9. NuLi, Y., Yang, J. & Wang, P. Electrodeposition of magnesium film from BMIMBF4 ionic liquid. *Appl. Surf. Sci.* **252,** 8086–8090 (2006).

10. Wang, P., NuLi, Y., Yang, J. & Feng, Z. Mixed ionic liquids as electrolyte for reversible deposition and dissolution of magnesium. *Surf. Coatings Technol.* **201,** 3783–3787 (2006).

11. Cheek, G. T., O'Grady, W. E., El Abedin, S. Z., Moustafa, E. M. & Endres, F. Studies on the Electrodeposition of Magnesium in Ionic Liquids. *J. Electrochem. Soc.* **155,** D91–95 (2008).

12. Murase, K. *et al.* Enhanced Anodic Dissolution of Magnesium in Quaternary-Ammonium-Based Ionic Liquid Containing a Small Amount of Water. *J. Electrochem. Soc.* **160,** D453–D458 (2013).

13. Amir, N., Vestfrid, Y., Chusid, O., Gofer, Y. & Aurbach, D. Progress in nonaqueous magnesium electrochemistry. *J. Power Sources* **174,** 1234–1240 (2007).

14. Shimamura, O., Yoshimoto, N., Matsumoto, M., Egashia, M. & Morita, M. Electrochemical co-deposition of magnesium with lithium from quaternary ammonium-based ionic liquid. *J. Power Sources* **196,** 1586–1588 (2011).

15. Vardar, G. *et al.* Electrochemistry of Magnesium Electrolytes in Ionic Liquids for Secondary Batteries. (2014).

16. Howlett, P. C., Izgorodina, E. I., Forsyth, M. & Macfarlane, D. R. Electrochemistry at Negative Potentials in Bis(trifluoromethansulfonyl)amide Ionic Liquids. *Zeitschrift fur Phys. chemie.* **220,** 1483–1498 (2006).

17. Zhao, Q., NuLi, Y., Nasiman, T., Yang, J. & Wang, J. Reversible Deposition and Dissolution of Magnesium from Imidazolium-Based Ionic Liquids. *Int. J. Electrochem.* **2012,** 1–8 (2012).

18. Galiński, M., Lewandowski, A. & Stępniak, I. Ionic liquids as electrolytes. *Electrochim. Acta* **51,** 5567–5580 (2006).

19. Lu, Z., Schechter, A., Moshkovich, M. & Aurbach, D. On the electrochemical behavior of magnesium electrodes in polar aprotic electrolyte solutions. *J. Electroanal. Chem.* **466,** 203–217 (1999).

20. Peled, E. & Straze, H. The Kinetics of the Magnesium Electrode in Thionyl Chloride Solutions. **834,** 1030–1035 (1977).

21. Appetecchi, G. B., Scaccia, S., Tizzani, C., Alessandrini, F. & Passerini, S. Synthesis of Hydrophobic Ionic Liquids for Electrochemical Applications. *J. Electrochem. Soc.* **153,** A1685–A1691 (2006).

22. Bard, A. J., Faulkner, L. R., Swain, E. & Robey, C. *Electrochemical Methods: Fundamentals and Applications*. (2001).

23. Rajput, N. N., Qu, X., Sa, N., Burrell, A. K. & Persson, K. a. The Coupling between Stability and Ion Pair Formation in Magnesium Electrolytes from First-Principles Quantum Mechanics and Classical Molecular Dynamics. *J. Am. Chem. Soc.* **137,** 3411–3420 (2015).

24. Su, Y.-Z., Fu, Y.-C., Wei, Y.-M., Yan, J.-W. & Mao, B.-W. The electrode/ionic liquid interface: electric double layer and metal electrodeposition. *Chemphyschem* **11,** 2764–78 (2010).

25. Zhang, C. *et al.* Chelate Effects in Glyme/Lithium Bis(trifluoromethanesulfonyl)amide Solvate Ionic Liquids. I. Stability of Solvate

Cations and Correlation with Electrolyte Properties. *J. Phy* **118,** 5144–5153 (2014).

26. Kitada, A. *et al.* Room Temperature Magnesium Electrodeposition from Glyme-Coordinated Ammonium Amide Electrolytes. *J. Electrochem. Soc.* **162,** D389–D396 (2015).

27. Kitada, A., Kang, Y., Uchimoto, Y. & Murase, K. Room-Temperature Electrodeposition of Mg Metal from Amide Salts Dissolved in Glyme-Ionic Liquid Mixture. *J. Electrochem. Soc.* **161,** D102–D106 (2014).

28. Fukutsuka, T. *et al.* New Magnesium-ion Conductive Electrolyte Solution Based on Triglyme for Reversible Magnesium Metal Deposition and Dissolution at Ambient Temperature. *Chem. Lett.* **43,** 1788–1790 (2014).

29. Ha, S. *et al.* Magnesium(II) Bis(trifluoromethane sulfonyl) Imide-Based Electrolytes with Wide Electrochemical Windows for Rechargeable Magnesium Batteries. *Appl. Mater. Interfaces* **6,** 4063–4073 (2014).

30. Watkins, T. & Buttry, D. a. Determination of Mg(2+) Speciation in a TFSI- Based Ionic Liquid With and Without Chelating Ethers Using Raman Spectroscopy. *J. Phys. Chem. B* (2015). doi:10.1021/acs.jpcb.5b00339

31. Ueno, K. *et al.* Anionic Effects on Solvate Ionic Liquid Electrolytes in Rechargeable Lithium–Sulfur Batteries. *J. Phys. Chem. C* **117,** 20509–20516 (2013).

32. Yoshida, K., Tsuchiya, M., Tachikawa, N., Dokko, K. & Watanabe, M. Correlation between Battery Performance and Lithium Ion Diffusion in Glyme-Lithium Bis(trifluoromethanesulfonyl)amide Equimolar Complexes. *J. Electrochem. Soc.* **159,** A1005–A1012 (2012).

33. Yoshida, K., Tsuchiya, M., Tachikawa, N., Dokko, K. & Watanabe, M. Change from Glyme Solutions to Quasi-ionic Liquids for Binary Mixtures Consisting of Lithium Bis(trifluoromethanesulfonyl)amide and Glymes. *J. Phys. Chem. C* **115,** 18384–18394 (2011).

34. Mandai, T. *et al.* Effect of ionic size on solvate stability of glyme-based solvate ionic liquids. *J. Phys. Chem. B* **119,** 1523–34 (2015).

35. Serizawa, N. *et al.* EQCM Measurement of Deposition and Dissolution of Lithium in Glyme-Li Salt Molten Complex. *J. Electrochem. Soc.* **160,** A1529–A1533 (2013).

36. Ueno, K. *et al.* Glyme-lithium salt equimolar molten mixtures: concentrated solutions or solvate ionic liquids? *J. Phys. Chem. B* **116,** 11323–31 (2012).

37. Mohtadi, R. & Mizuno, F. Magnesium batteries: Current state of the art, issues and future perspectives. *Beilstein J. Nanotechnol.* **5,** 1291–311 (2014).

CHAPTER 3

DETERMINATION OF MG^{2+} SPECIATION IN A $TFSI^-$-BASED IONIC LIQUID WITH AND WITHOUT CHELATING ETHERS USING RAMAN SPECTROSCOPY

3.1 Introduction

Figures and text in this chapter were reprinted with permission from Watkins, T.; Buttry, D. A. Determination of Mg^{2+} Speciation in a $TFSI^-$-Based Ionic Liquid With and Without Chelating Ethers Using Raman Spectroscopy. *J. Phys. Chem. B* **2015**, 119, 7003–7014. Copyright 2015 American Chemical Society.

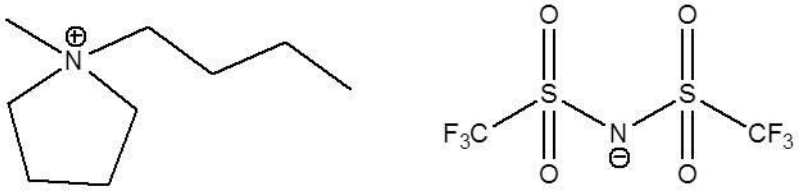

Figure 15: Schematic representation of the BMPyrTFSI RTIL used in this study.

With an ever greater demand for off-grid energy storage and non-fossil fuel burning vehicles, there is increasing hope for better Li-ion batteries, or batteries beyond Li-ion technology. One such prospect is a secondary battery with a pure Mg anode. Magnesium has several advantages over LiC_6 electrodes found in typical Li-ion cells today.[20–23] However, the chemistries for such an innovation have been explored for some time now without the successful design of a prototype with true commercial interest. To date, the most favorable electrolytes and electrodes for Mg electrochemistry still lack the necessary requirements to produce a viable product. Despite the advantages they might bring, ionic liquid based electrolytes have received only a small fraction of the attention in this area.[20–23,18,19,15,24–33] Here, we have studied the complex environment of Mg^{2+} in

the room temperature ionic liquid (RTIL) N-butyl-N-methylpyrrolidinium bis(trifluoromethylsulfonyl)imide (BMPyrTFSI or $Pyr_{14}TFSI$) (shown in figure 15), with the effects on the electrochemical behavior in mind.

There has been a good deal of work studying the speciation of Li^+ in RTILs, especially those containing the bis(trifluoromethylsulfonyl)imide ($TFSI^-$) anion.[34–51] LiTFSI dissolved in pyrrolidinium or imidazolium based TFSI RTILs are notable examples. This work is relevant to the analogous speciation of Mg^{2+} in ionic liquids containing $TFSI^-$, so we briefly review it here. These past reports have used a myriad of techniques to assess the complexation environment for Li^+ with $TFSI^-$ in these RTILs. Various values have been given for the average number of $TFSI^-$ surrounding Li^+ (n) in $[Li(TFSI)_n]^{-(n-1)}$ complexes formed under these conditions. The general consensus is $n \geq 2$ for lower LiTFSI concentrations ($x \leq 0.2$ in $[LiTFSI]_x[IL]_{1-x}$). An n value of 2 or greater is not surprising as a single $TFSI^-$ anion would not be suitable for the coordination conditions necessary for a single Li^+ cation. There is some ambiguity in the literature concerning the nature of coordination of $TFSI^-$ with Li^+ in ionic liquid environments, particularly at higher concentrations of LiTFSI. Most of the disagreement can be attributed to the limitations of the various techniques used to determine the number of $TFSI^-$ surrounding Li^+, or the various geometries for the coordinated anions. For instance, it is not entirely clear from Raman spectra of liquid samples whether a coordinated $TFSI^-$ exists in an aggregate network (AGG — coordinating multiple metal cations) or in a contact ion pair (CIP — coordinating a single metal cation).[36] Single

crystal X-ray measurements have shed light on the issue, but are limited to the solid state and distinct crystallizing compositions.[45–48]

The number of $TFSI^-$ involved in a Li^+ complex is important because if n is 2 or greater anionic complexes are the predominant species. These complexes are likely the cause of the low solution conductivities, Li^+ self-diffusion coefficients and Li^+ transference numbers in such systems.[34,46,47] The same logic can be applied to Mg^{2+} complexes, discussed below. Thus, we focus here on the speciation of Mg^{2+} in RTIL's containing $TFSI^-$. Giffin *et al*. also recently reported on the speciation for Mg^{2+} in BMPyrTFSI.[50] The analysis here confirms many of their conclusions but offers a slightly different analysis.

A second topic described here is the use of chelating agents to replace the $TFSI^-$ coordinating shell around Mg^{2+} with neutral ligands, which changes the charge of the species involved in Mg^{2+} transport. This concept has been extensively explored mainly in the Li electrolyte literature—other salts like those of Na^+, K^+, etc. have been investigated as well—for over a decade.[52–68] We focus specifically on ether based chelators in this study. Although they were not the pioneers of this area, Watanabe *et al.* have recently contributed significantly through their exploration of conditions in which oligoether glymes, with chemical structure $CH_3O–(CH_2–CH_2–O)_m–CH_3$, were used to create solvates with LiTFSI and a few other LiX salts.[61–66] In these materials, Li^+ is preferentially coordinated by one or more glyme ligands rather than the RTIL anions. For instance, at a 1:1 ratio of Li^+ with triglyme (G3) or tetraglyme (G4), Li^+ ions exist in cationic complexes $[Li(Gm)]^+$. The effects of the glyme coordination are so pronounced

that the mixtures result in the creation of room temperature liquids, dubbed solvate ionic liquids.[62]

The idea of chelating groups acting as ligands surrounding ions in a salt, so that the new ion-ligand species creates a lower melting salt with the counter ion, was first introduced by Angell in 1965 but was relatively unexplored until recently, mainly with the interest of pursuing better Li battery electrolytes (the term "solvate IL" was coined by Angell *et al*. in their 2012 review article).[67,17] A solvate IL (sometimes referred to as a "chelate" IL) is a material resembling conventional ILs but in which one or more of the ions exists as a complex with a neutral ligand (for example, the $[Li(Gm)]^+$ complex as the cation and $TFSI^-$ as the anion). Strictly speaking, formation of a solvate compound is only one requirement for the classification of solvate ILs; a more rigorous discussion on what qualifies a solution to be classified as a solvate IL can be found in reference 45. These systems can have attractive properties. For example, Li^+-glyme complexation has been shown to increase the Li^+ transference number by 4–6 times compared to Li^+ complexed with $TFSI^-$ in conventional RTIL solutions, and to give reversible Li deposition and dissolution with nearly 100% coulombic efficiency.[61–65] Coordination with Li^+ was also observed to enhance the oxidative stability of the glymes and allows for the possible implementation of $\geq$ 4V class cathodes for Li^+ intercalation.[63] These findings prompted the present investigation to study analogous $Mg(L)_y(TFSI)_2$ solvates, as well as $[Mg(L)y(TFSI)_2]_x[BMPTFSI]_{1-x}$ (L = Gm, THF or 18-crown 6 ether) solutions. The chelating effects found for Li(L)yTFSI and $[Li(L)_y(TFSI)]_x[IL]_{1-x}$ solutions appear to be very similar in the Mg analogues, which suggests that the higher order glyme

$Mg(Gm)(TFSI)_2$ solutions, in particular, meet the criteria to be defined as solvate ILs. Such chelated systems may provide promising chemical routes for Mg battery electrolytes.

3.2 Experimental

N-butyl-N-methylpyrrolidinium bis(trifluoromethylsulfonyl)imide (BMPyrTFSI) was synthesized and purified in a similar manner to reported procedures with additional recrystallizations of the precursor, N-butyl-N-methylpyrrolidinium iodide, prior to a metathesis reaction with LiTFSI (used as received from TCI, 99.95%).[69] BMPyrTFSI was also purchased in ultrapure form (99.95%) from IoLiTec® and used as received. Both sources of the RTIL were shown to be suitably pure using spectroscopic measurements (NMR, IR, and Raman). Magnesium salts, $MgCl_2$ (ROC/RIC, 98+%), MgI_2 (Alfa Aesar, 99.996%), $MgBr_2$ (Alfa Aesar), $Mg(ClO_4)_2$ (Sigma Aldrich) and $Mg(TFSI)_2$ (Strem Chemicals 97.5%) were dried under high dynamic vacuum (0.1–0.3 mTorr) and high temperatures (>120°C) for generally ≥ 16hrs on a vacuum line, equipped with a diffusion pump, prior to use. The BMPyrTFSI was separately dried at ≥ 130°C for ≥ 16hrs. Karl Fischer titrations (Mettler Toledo C20) were used to measure water concentrations at ppm levels for the RTIL alone as well as for solutions containing the salts (water levels were found to be below the limit of detection for the instrument, nominally below 1 ppm). Oligoether glymes and THF (Sigma Aldrich) were distilled using sodium and benzophenone followed by storage over 3 Å molecular sieves. Water was found to be in the 3-5 ppm range for both glymes and THF. Prior to measurements, solutions were

prepared in an inert Ar atmosphere VAC MO-10 glove box with monitored water and oxygen levels (each held around or below 2 ppm).

For Raman spectroscopy, solutions were prepared in sealable quartz cuvettes and transferred from the glove box to the Raman instrument. A wide compositional range, $0 \leq x \leq 0.55$ for $[Mg(TFSI)_2]_x[BMPyrTFSI]_{1-x}$, was evaluated. Samples were prepared by adding the appropriate amount of $Mg(TFSI)_2$ and BMPyrTFSI and stirring for several minutes to hours, sometimes applying mild heat to speed up dissolution. Above $x = 0.4$, $Mg(TFSI)_2$ was dissolved with applied heat (approximately 60-80°C), subsequently allowed to cool to room temperature and spectra were soon after acquired in the liquid state. Glyme-$Mg(TFSI)_2$ mixtures (solvate ILs) were prepared in a similar way. Stoichiometric amounts of each component were mixed at approximately 70–100°C until homogenous mixtures/solutions were produced. Raman data shown in the figures were acquired at room temperature, no major effect was observed when increasing the temperature up to 70°C. Raman data were collected using a custom built Raman spectrometer in a 180° geometry. The samples were excited using a 100 mW Compass 532 nm laser for all but the yellow tinted MgI_2 samples which required a red 632 nm, 40 mW line. The laser power was controlled using neutral density filters. The laser was focused onto the sample using a 50X super long working distance Mitutoyo objective lens with a numerical aperture of 0.42. The signal was discriminated from the laser excitation using a Kaiser Laser band pass filter followed by a Semrock edge filter. The data were collected using an Acton 300i spectrograph and a back thinned Princeton Instruments liquid nitrogen cooled CCD detector. For the regions of interest,

measurements were made with an 1800 nm grating from 50-1200 cm^{-1} (1 cm^{-1} resolution). Spectra were acquired for 30 seconds five times to obtain an acceptable signal to noise level. A custom made Matlab GUI was used to fit pseudo Voigt functions, in which the Lorentzian/Gaussian characters and FWHM could be varied manually, to the raw data. Raw spectra were corrected with use of a cyclohexane standard for accurate frequency determination. Spectra shown in the figures were normalized to the highest peak and fluorescent backgrounds (usually not that intense) were subtracted.

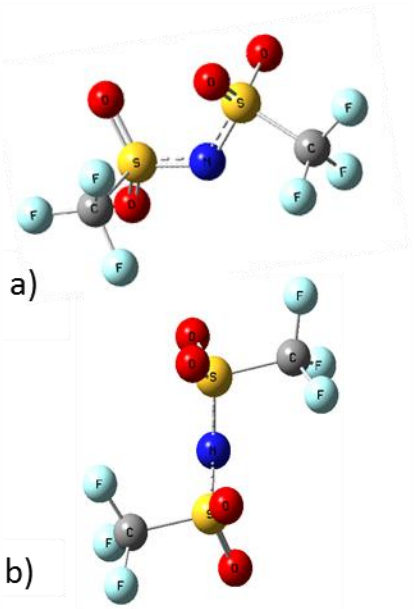

Figure 16: $TFSI^-$ conformers a) Cis conformation with *C*1 symmetry b) Trans conformation with *C*2 symmetry.

Linear sweep voltammograms were acquired using a Pt wire working electrode, cleaned by annealing with a Bunsen burner, and a Mg ribbon counter electrode (polished with coarse sand paper and wiped with a Kim Wipe). A luggin capillary was built by sealing glass around a small piece of Pt and polished Mg ribbon was immersed in a 0.3 M

EtMgBr/BMPyrTFSI:THF (3:1) solution within the reference electrode container to give a reversible, and therefore stable, Mg/Mg^{2+} reference couple. Oxidative stabilities of electrolyte solutions were assessed at 1 mV/s scan rates.

3.3 Results and Discussion:

3.3.1 The $TFSI^-$ Anion

The $TFSI^-$ anion has been widely employed in electrochemical research due to its relatively high anodic stability, and tendency to create ILs with low viscosity with respect to other IL anions paired with equivalent cations—a condition which tends to produce ILs with higher molar conductivities. It is also used in the plasticizing of linear polymers like PEO.[70,71] LiTFSI, in particular, has been a commonly studied salt in amorphous polymer electrolyte systems, in which it produces a relatively high ionic conductivity.[70,72] Conformational flexibility of $TFSI^-$ arises from a small energy barrier, ~3.5 kJ/mole, between the two calculated conformers (the minimum energy, trans *C*2 state, and the slightly higher local minimum, cis *C*1 state (see figure 16).[70,71,73,74] A third intermediate conformational state has been predicted by some computational models but rarely observed experimentally, perhaps only being definitively identified in the $[LiTFSI]_{0.67}[Pyr15TFSI]_{0.33}$ single crystal.[47,75,76] Calculations predict the negative charge in $TFSI^-$ to be highly delocalized, which rationalizes TFSI's relatively weak coordinating ability. However, the notion of weak coordination of the $TFSI^-$ anion with metal cations has been contested by some studies showing considerable contact ion pairing with Li^+ in acetonitrile and glyme solvents even at relatively dilute concentrations.[76–78] Furthermore,

a report by Rajput *et al*., published as this paper was under review, used computational simulations to predict the degree of $TFSI^-$ anion coordination with Mg^{2+} in various solvents.[79] That study suggests considerable ion pair formation may occur between Mg^{2+} and $TFSI^-$, even at "modest" concentrations in many organic solvents, but very little ion pairing was predicted for the higher order oligoethers G2 and G4. It was concluded that Mg^{2+} speciation in a solvent is determined by not only the dielectric constant but by the size, denticity and coordinating properties of the chelating ligands as well.

3.3.2 Complexation and Coordination Numbers

In considering metal cation speciation in RTIL's containing $TFSI^-$, it is useful to distinguish between n (average number of $TFSI^-$ anions around the metal center) and coordination number (CN, average number of atoms coordinated to the metal center). Sometimes n is referred to as the solvation number; however, others reserve the term specifically for coordination with neutral solvent molecules. With respect to the complex environment, $TFSI^-$ anions can coordinate to a single metal cation in isolated metal-$TFSI^-$ contact ion pairs (CIPs), multiple metal cations in aggregate ion networks (AGGs) or not coordinate at all and exist as solvent separated ion pairs (SSIPs). Based on the measured populations of each of these speciation conditions, an average number of $TFSI^-$ coordinating the metal cations is determined. Alternatively, the coordination number is usually a consequence of the preferred coordination geometry around the metal center. For instance, in aprotic solvents used for Li-ion battery electrolytes, such as propylene carbonate, Li^+ often adopts a tetrahedral geometry in which it is coordinated by four oxygens. Several studies of Li-glyme solvates have also shown Li^+ existing in

octahedral/distorted octahedral coordination geometries in the crystalline state.[53,54,59,77,80] For $TFSI^-$ the coordination number is given by the average number of oxygen atoms coordinated to the metal cation, regardless of the number of $TFSI^-$ anions from which the oxygens originate.

The average number of $TFSI^-$ surrounding the metal cation has a pronounced impact on physical properties. For example, if n is 2 or greater, Li^+ ions exist in anionic complexes. Similarly, for ILs containing Mg^{2+}, if n is 3 or greater, Mg^{2+} ions exist in anionic complexes. Such anionic speciation can influence the metal cation transference number. In addition, the denticity of the anion may affect its rate of dissociation from the metal center, potentially influencing the electrochemical rates, as understood through Marcus Theory.[34] Thus, there is value in assessing the details of the interactions between metal cations and RTIL anions and of finding ways to influence those interactions.

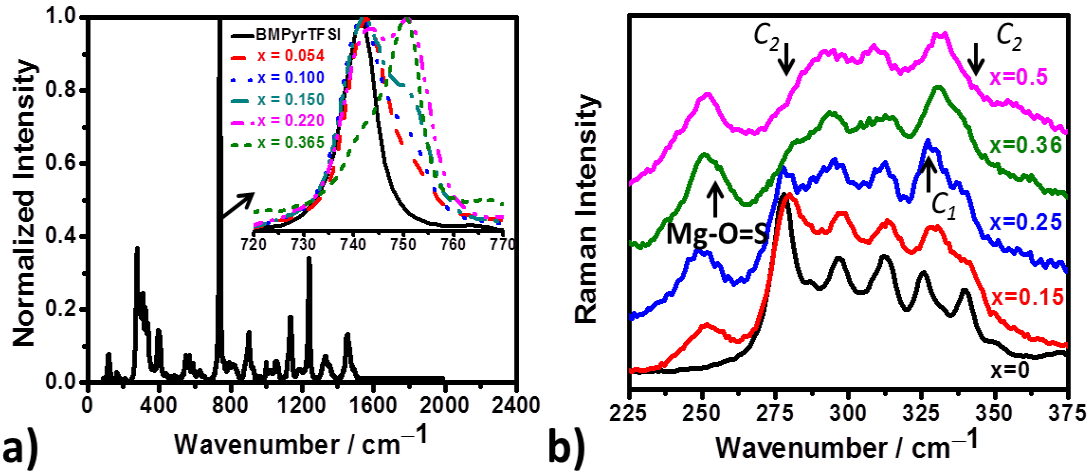

Figure 17: a) BMPyrTFSI Raman spectrum from 87–2000cm^{-1}. Inset displays 720 cm^{-1} to 770 cm^{-1} region at varying compositions of $Mg(TFSI)_2$. b) Spectra in the 225 cm^{-1} to 375 cm^{-1} region. Spectral intensities are shifted for clarity. C_1 and C_2 highlight the bands belonging to cis and trans conformers respectively. The composition is described by the formula $[Mg(TFSI)_2]_x[BMPyrTFSI]_{1-x}$.

3.3.3 Coordination Environment of Mg^{2+}

It has been shown that Li^+ and most other metal cations exist in coordination with $TFSI^-$ through interactions with the oxygen atoms, as opposed to the nitrogen or fluorine.[34–45,49,50] In fact, only the CsTFSI salt shows coordination to the metal cation through nitrogen.[45,75] For the analysis below, we assume Mg^{2+} interactions with $TFSI^-$ occur exclusively through oxygens.

Raman spectroscopy was used here to assess the Mg^{2+} complexation environment. We adopt the notation conventions from previous studies on Li^+ speciation for ease of comparison.[34–50] Figure 17a shows the Raman spectrum for pure BMPyrTFSI. The most intense peak at 742cm^{-1} is from a vibrational band originating from a complex breathing

mode of the $TFSI^-$ anion in which the entire anion is expanding and contracting, giving a large change in polarizability and an intense Raman band.[71] The mode contains SNS stretching and bending, OSO scissors motion, and CF_3 deformation. This frequency corresponds to that for a "free" $TFSI^-$, meaning a $TFSI^-$ that is not strongly associated to any cations.[34–41] The peak was best fit with a pseudo Voigt function employing an 85% Lorentzian and 15% Gaussian character with a full width at half maximum (FWHM) of 6.3–7 cm^{-1}; which is consistent with previous reports.[36] The two $TFSI^-$ conformational states cannot be resolved under these conditions and each contributes to the peak broadening. The inset in figure 17a shows that progressive addition of $Mg(TFSI)_2$ to the RTIL gives rise to a new distinct peak centered at 752 cm^{-1}, attributed to Mg^{2+}-$TFSI^-$ coordination. As the concentration of $Mg(TFSI)_2$ in $[Mg(TFSI)_2]_x[BMPyrTFSI]_{1-x}$ increases, the 752 cm^{-1} peak becomes increasingly intense. Similar behavior is observed on addition of Li^+ to ILs containing $TFSI^-$.[34–41] The frequency shift due to coordination for $TFSI^-$ bound to Mg^{2+} (10–11 cm^{-1}) is slightly larger than that for $TFSI^-$ bound to Li^+ (6–7 cm^{-1}). This larger blue shift suggests a stronger coordination.[81] This is expected due to the higher charge to radius ratio of Mg^{2+}, Mg^{2+} being a much harder ion than Li^+. These results suggest that the Raman shift to a higher frequency can be used as a spectroscopic signature of $TFSI^-$ tightly bound to Mg^{2+}, analogous to the case for Li^+.

A lower energy region of the spectrum is shown in figure 17b. The observed bands are all attributed to $TFSI^-$ modes and have been assigned in previous reports.[39,71,74] Several vibrations in this region are sensitive to the particular conformational states of the anion. As stated above, the trans *C*2 state is slightly lower in energy than the cis *C*1

conformer, yet cis appears to be the preferred geometry for $TFSI^-$ when coordinated with Li^+, as experimentally verified.[35,36,38,45,82] Preference for the cis conformer appears to be the case for coordination with Mg^{2+} as well, as indicated by a decrease in the trans dominant bands at 279 cm^{-1}, 297 cm^{-1} and 341 cm^{-1}, and an increase in the cis band at 326 cm^{-1} as the $Mg(TFSI)_2$ concentration increased. The preference of the $TFSI^-$ anion to take on a cis conformation when coordinated to the metal cation was attributed to a stabilizing effect from the IL cations in the second solvation sphere by Umebayashi *et al*, but may also be due to the greater dipole moment of the cis conformer.[82,83] Furthermore, we tentatively attribute a peak centered at 250 cm^{-1}, not seen in LiTFSI samples, to a Mg^{2+}–O=S mode as it is similar to the mode at 245 cm^{-1} ascribed to Mg^{2+}–OSO_3^{2-} for magnesium-sulfate contact ion pairs in aqueous $MgSO_4$ solutions.[84]

3.3.4 Determination of the Average Number of $TFSI^-$ Coordinated to Mg^{2+}

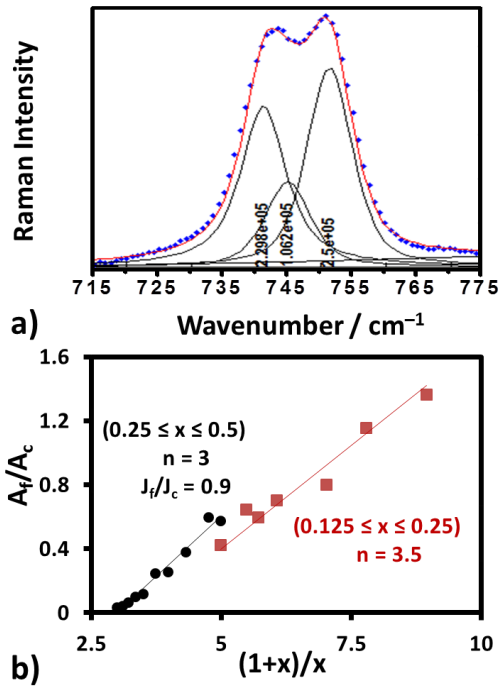

Figure 18: a) Pseudo-Voigt function fits of the raw Raman data between 715 cm^{-1} and 775 cm^{-1}. Numbers under the curves depict the respective intensities of each peak. b) Ratio of the free $TFSI^-$ to coordinated $TFSI^-$ vs. (1+x)/x for two separate compositional regions.

The fractional populations of $TFSI^-$ anions in free and coordinated states were determined using integrated areas under fitted curves. In figure 18a the raw data collected between 715 cm^{-1} and 775 cm^{-1} for $[Mg(TFSI)_2]_{0.2}[BMPyrTFSI]_{0.8}$ were manually fit by three modeled curves with equivalent FWHM values (~7 cm^{-1}). Peaks were modeled with pseudo Voigt functions: $f(\upsilon) = lL(\upsilon) + (1-l)G(\upsilon)$, where L and G stand for Lorentzian and Gaussian components, respectively, and l is the weighted Lorentzian

average. The Lorentzian characters (l) were held constant at 0.85, 0.5, and 0.5 for the peaks centered at 742 cm^{-1}, 746 cm^{-1} and 752 cm^{-1}, respectively. This treatment is justified when considering that weakly interacting (non-coordinating) $TFSI^-$ are able to move less impeded by the medium than $[Mg(TFSI)_n]^{(2-n)}$ CIPs or $Mg_z(TFSI)_n^{(2z-n)}$ AGGs and would thus be expected to have a more Lorentzian like line shape.[85] Initial attempts at data fitting used a two peak fit model, as reported for LiTFSI in RTILs.[34–41,50] However, three peaks more reliably gave the best fits of the raw data. A three peak model is in contrast to the two peak fit model of Fujii *et al*. used for divalent transition metal ions in a $TFSI^-$ RTIL.[83] However, Giffin *et al*. also used a three peak treatment for $[Mg(TFSI)_2]_x[BMPyrTFSI]_{1-x}$ and justified this by suggesting the low, mid, and high frequency bands belonged to free $TFSI^-$, monodentate coordinated $TFSI^-$ in CIPs and/or AGGs, and bidentate coordinated CIP $TFSI^-$, respectively. Those workers noted a difficulty in distinguishing between CIP and AGG structures in the mid frequency band.[50] Their report included DFT simulations that supported this model. Bidentate CIP coordination was calculated to have a vibrational mode at least 5 cm^{-1} higher than the free anion, while monodentate CIP coordination was calculated to have a mode no more than 2 cm^{-1} higher than the free anion. We similarly assigned free, monodentate CIP/AGG and bidentate CIP/AGG coordination to the low, mid and high frequency peaks in the 715–775 cm^{-1} region, respectively. Assigning the bands to these geometries aligns well with the assignments given for Raman spectra of single crystal compositions of $[LiTFSI]_x[Pyr_{15}TFSI]_{1-x}$.[47] We believe this model is further supported by considering the resulting average coordination numbers determined from the relative fractions of

monodentate and bidentate associations (5.5–6 at all compositions as determined using equation 12), described below.

For $[LiTFSI]_x[RTIL]_{1-x}$ systems, two related approaches have been reported for determining the average number of $TFSI^-$ coordinating Li^+. In one method, described by Umebayashi *et al*., the spectra were normalized using cation bands from the two RTIL media studied, EMImTFSI and BMPyrTFSI.[38] The average number of $TFSI^-$ surrounding Li^+, assumed to be constant in the examined concentration range, was determined by integrating under the pseudo-Voigt functions for fitting the respective vibrational bands (742 cm^{-1} and 748 cm^{-1}). The integrated areas represent populations of each species so that:

$$A_f = J_f C_f \qquad (3.1)$$

Where A_f is the integrated area under the free $TFSI^-$ peak, J_f is the molar Raman scattering coefficient of the free $TFSI^-$ band and C_f is the concentration of free $TFSI^-$ in the solution. Note that equation 1 must hold true for any IL-salt mixture. The concentration of free $TFSI^-$ can then be expressed in terms of the metal cation concentration as:

$$C_f = C_{tot} - C_c = C_{tot} - nC_M \qquad (3.2)$$

Where C_{tot} is the total concentration of $TFSI^-$, C_c is the concentration of $TFSI^-$ coordinated to the metal cation, C_M is the concentration of metal cation and n is the average number of $TFSI^-$ coordinating Li^+ (Note: concentrations were corrected for

changing densities in their study). Using C_f, as expressed in equation 2, in equation 1 and rearranging the formula gives rise to the following relationship:

$$\frac{A_f}{C_M} = J_f(R - n) \tag{3.3}$$

where $R = C_{tot}/C_M$. Therefore, the molar Raman scattering coefficient for free $TFSI^-$ is found from the slope of A_f/C_M with respect to R. The average number of $TFSI^-$ around Li^+ cations was then found from:

$$n = \frac{-\beta}{J_f} \tag{3.4}$$

Where β is the y intercept. Using this approach Umebayahsi *et al*. found n to be 1.86(8) and 1.86(3) for LiTFSI in EMImTFSI and BMPyrTFSI, respectively (for $C_{Li} \leq 565$mM i.e. $x \leq 0.14$). They also found $J_c/J_f = 0.9$ for both solutions. It was thus concluded that $TFSI^-$ is not strongly polarized in the Li^+ solvation sphere (i.e. coordination does not strongly influence the Raman scattering cross-section). It is important to note that equations 3 and 4 are only true when n is constant across the measured concentration range. Furthermore, for a first approximation, equation 3 can be rewritten using compositional fractions, thereby eliminating a need to correct concentrations for changing densities. For $[LiTFSI]_x[BMPyrTFSI]_{1-x}$, the population of total $TFSI^-$ in the system can be assigned by $(1 - x) + x = 1$; the fraction of $TFSI^-$ in the material being $1/[2x+2(1-x)] = ½$, always. The fraction of *free* $TFSI^-$ is equal to $1 - nx$ (n representing the number of coordinated $TFSI^-$). Therefore, the area under the free peak is given by:

$$A_f = J'_f(1 - nx) \tag{3.5}$$

Equation 5 is analogous to equation 1 but J_f is no longer a *molar* scattering coefficient but instead a "fractional" scattering coefficient and given the prime label to differentiate it from the molar scattering coefficient. Equation 5 can thus be rearranged to give:

$$\frac{A_f}{x} = J'_f\left[\left(\frac{1}{x}\right) - n\right] \quad (3.6)$$

However, equation 6 does not hold true for $Mg(TFSI)_2$, or any other divalent metal-$TFSI^-$ salt, because additions of $Mg(TFSI)_2$ differ from molar equivalent additions of LiTFSI. Each Mg^{2+} comes with a pair of $TFSI^-$, as opposed to just one of the counter ions added with each Li^+. Therefore, an alternative formula to that of equation 6 is derived for the $[Mg(TFSI)_2]_x[BMPyrTFSI]_{1-x}$ system. Here, the population of $TFSI^-$ is alternatively given by $(1 - x) + 2x = 1 + x$. So, for divalent cation-$TFSI^-$ salts equation 6 becomes:

$$\frac{A_f}{x} = J'_f\left[\left(\frac{1+x}{x}\right) - n\right] \quad (3.7)$$

From this, the fractional scattering coefficient for free $TFSI^-$ (J'_f) can be found. Furthermore, the fractional scattering coefficient for coordinated $TFSI^-$ (J'_c) dictates the area under the *coordinated* peak in a similar way:

$$A_c = J'_c nx \quad (3.8)$$

From these expressions we can determine whether or not the free and coordinated $TFSI^-$ have similar fractional scattering coefficients. We may, therefore, divide equation 7 by equation 8 to obtain:

$$\frac{A_f}{A_c} = \frac{J'_f}{J'_c}\frac{(1+x)}{nx} - \frac{J'_f}{J'_c} \quad (3.9)$$

Thus, J'_f/J'_c is found from the intercept (β) of A_f/A_c vs. (1+x)/x. The average number of $TFSI^-$ surrounding Mg^{2+} (n) is given by –β/s (s = slope). To determine J'_f/J'_c we analyzed the data using equation 9 in a compositional region in which n seemed to be fairly constant ($0.25 \leq x \leq 0.5$) (see figure 18b). In this region, J'_f/J'_c and n were found to be 0.90 ± 0.1 and 3.0 ± 0.3, respectively. Therefore, it is concluded that the Raman scattering coefficients are indeed nearly identical. Plotted along with the ($0.25 \leq x \leq 0.5$) compositional region is the ($0.125 \leq x \leq 0.25$) region. Fixing J'_f/J'_c at 0.9 gave n = 3.5 ± 0.4 for these compositions. Not shown in figure 18b, is the ($0 \leq x \leq 0.125$) region which gave n = 4.5 ± 0.6.

In separate work from Lassègues *et al*. the validity of the above approach was verified for $[LiTFSI]_x[RTIL]_{1-x}$ systems. They also showed the initial assumption of equal scattering coefficients did, in fact, result in the same conclusions for n.[35–37] Assuming equal scattering coefficients:

$$\frac{A_c}{A_{tot}} = nx \qquad (3.10)$$

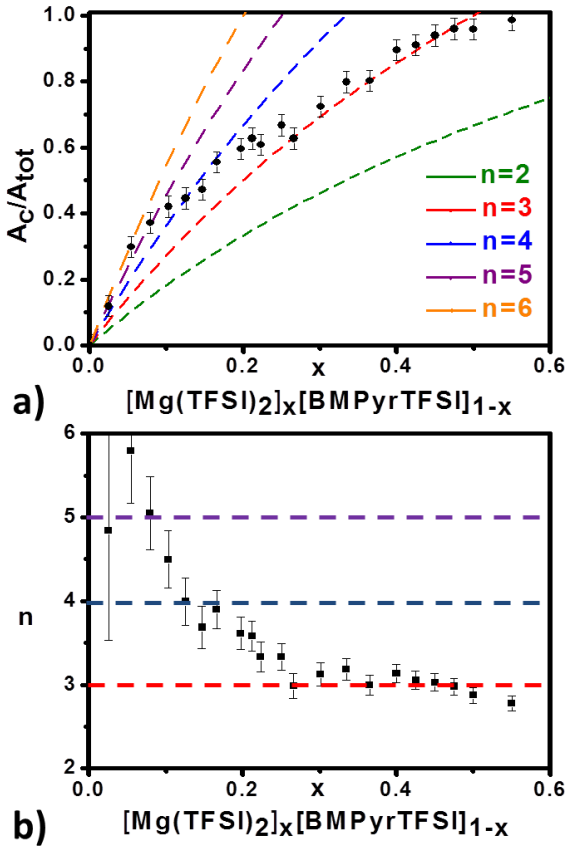

Figure 19: a) Fraction of $TFSI^-$ coordinated to Mg^{2+} with respect to the mole fraction of $Mg(TFSI)_2$ in the solution. Dashed curves follow theoretical trends for n values, as determined using equation 11. b) Calculated n as a function of x, using equation 11.

where x is the molar fraction of LiTFSI and n is the average number of $TFSI^-$ around Li^+ cations, as defined earlier. Equation 10 is derived by considering the population of coordinated $TFSI^-$ to be equal to nx (A_c = nx, so A_f = 1-nx). In other words, every mole of LiTFSI added results in n moles of $TFSI^-$ in the Li^+ solvation shell. Thus, the area of the higher frequency peak, having an equal scattering coefficient, must be related to the number of coordinated $TFSI^-$ in this way. Then, the slope of A_c/A_{tot} vs. x gives n. In

testing a larger concentration range, $0.08 \leq x \leq 0.5$, Lassègues *et al*. came to essentially the same conclusion for n, further noting its decline at higher concentrations of LiTFSI; suggesting a higher degree of AGG clusters as suggested from the MD simulations performed by Borodin *et al*.[36,41]

Equation 10 does not hold for $[Mg(TFSI)_2]_x[BMPyrTFSI]_{1-x}$, for the same reason alluded to above for equations 6 and 7. The relationship between A_c/A_{tot} and x, in $[Mg(TFSI)_2]_x[BMPyrTFSI]_{1-x}$, is alternatively derived as follows: $A_c = nx$ (as is the case for LiTFSI) and $A_{tot} = 2x + (1-x) = 1+x$ (as opposed to $A_{tot} = 1$ for LiTFSI). Therefore:

$$\frac{A_c}{A_{tot}} = \frac{nx}{1+x} \tag{3.11}$$

This formula introduces a slight downward bowing in the theoretical n curves as observed in figure 19a, which plots the fraction of coordinated $TFSI^-$ anions (includes areas from both 746 cm^{-1} and 752 cm^{-1} peaks) as a function of the $Mg(TFSI)_2$ molar concentration (x) (vertical error bars denote a combined standard deviation in the measurements and fits of ± 0.03 for A_c/A_{tot}; errors in x are contained within the data markers). Calculated n values are plotted in figure 19b. Error bars reflect the fact that at lower concentrations, uncertainty in A_c/A_{tot} magnifies the uncertainty associated with the calculated n values. We found a similar yet slightly altered trend to that of Giffin *et al.* as they assumed a linear relationship between A_c/A_{tot} and x to hold for the $Mg(TFSI)_2$ system as it does for LiTFSI. This is a good approximation but is not strictly true, as shown in equation 11. With the determination of n values, the complex species can be described by the formula $Mg[TFSI]_n^{(2-n)}$, for CIPs, or $Mg_z[TFSI]_n^{(2z-n)}$, for AGGs.

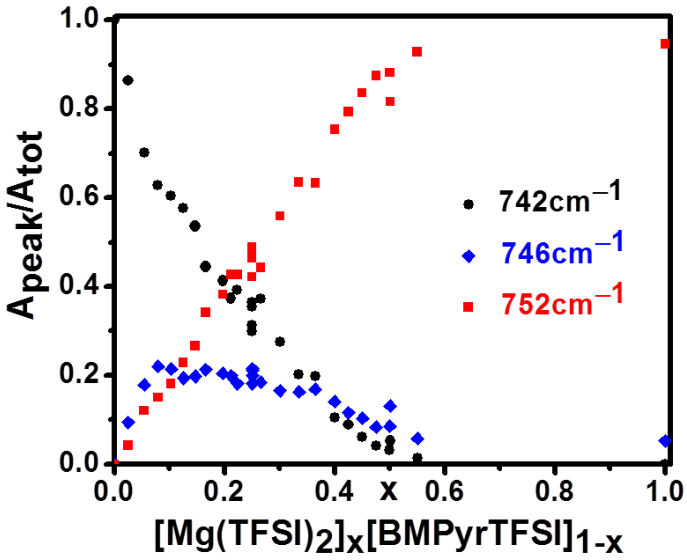

Figure 20: Fractional area of each of the three fit peaks.

The difficulty with differentiating between CIPs and AGGs, especially in the liquid state, using vibrational spectroscopy has been noted in the literature.[36,50] However, it does appear that monodentate ligands (in either CIPs or AGGs) can be distinguished from bidentate ligands in the $[Mg(TFSI)_2]_x[BMPyrTFSI]_{1-x}$ system, since the vibrational energies of the coordinated peaks are well separated from each other, as well as being adequately separated from the energy of the free $TFSI^-$ vibration. Figure 20 shows how the free (742 cm^{-1}), monodentate coordinated (746 cm^{-1}) and bidentate coordinated (752 cm^{-1}) $TFSI^-$ peaks' integrated areas changed with respect to x. A linear increase in the 752 cm^{-1} peak up to x = 0.48, followed by a shallower slope up to x = 0.55, was observed. At x = 0.55 (the solubility limit) the speciation appeared to reach a maximum of 95% $TFSI^-$ existing in bidentate coordination and no free $TFSI^-$. The fraction of the area under the 742 cm^{-1} peak drops abruptly between pure BMPyrTFSI and x = 0.05

followed by a monotonic decline until it reaches zero at x = 0.55. The corresponding change in the 746 cm^{-1} peak is interesting in that it quickly rises to x = 0.08 before slowly declining thereafter. This indicates that there is a preference for bidentate coordination for $TFSI^-$ with Mg^{2+} at higher Mg^{2+} concentrations. This is reasonable given that increasing the $Mg(TFSI)_2$ fraction of the solution eventually approaches a limit in which the $TFSI^-/Mg^{2+}$ ratio reaches 2 at pure $Mg(TFSI)_2$. If the coordination number around Mg^{2+} is to remain around 5 or 6, as expected from several previous Mg^{2+} speciation studies, bidentate ligands would be required to provide a sufficient number of oxygens to coordinate each Mg^{2+} cation.[20,84,86] At the highest $Mg(TFSI)_2$ concentrations in particular, a high degree of aggregation would also be necessary to provide the appropriate coordinating conditions. Coordination numbers were calculated using weighted averages from bidentate (A_2) and monodentate (A_1) coordination peak areas, with the calculated values for n at given compositions, given by:

$$CN = n[2\left(\frac{A_2}{A_c}\right) + \left(\frac{A_1}{A_c}\right)] \quad (3.12)$$

Values were calculated to be between 5.5 and 6.0 for most concentrations examined, consistent with expectations.

Table 2: Solubility limits with respect to the mole fraction of the dissolved salt in BMPyrTFSI.

Salt	Solubility limit at RT
$Mg(ClO_4)_2$	x = 0.3
MgI_2	x = 0.13
$MgBr_2$	x = 0.05
$MgCl_2$	x = 0.03

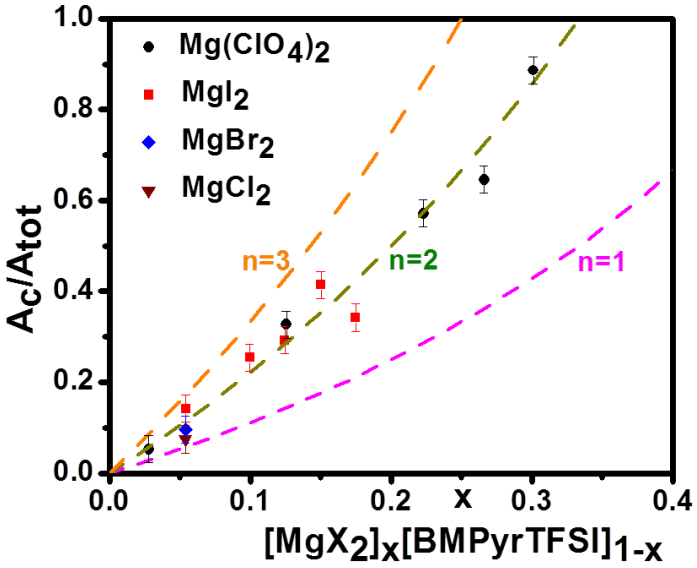

Figure 21: Fraction of coordinated $TFSI^-$ anions as a function of the molar fractions of given Mg^{2+} salts.

Plotted in figure 21 are measurements made for other $[MgX_2]_x[BMPyrTFSI]_{1-x}$ salts ($X = ClO_4^-$, I^-, Br^-, Cl^-). These MgX_2 salts varied in their solubility with BMPyrTFSI as depicted in table 1. The lower solubility limits are likely due to higher lattice energies of those salts. $MgCl_2$ and $MgBr_2$ saturate the solution at x = 0.05 and do

not show an increased Mg^{2+}-$TFSI^-$ peak above this concentration. However, MgI_2 does show an increase in the coordinated peaks up to x = 0.13. $Mg(ClO_4)_2$ was much more soluble than the halide salts, with a limit at x = 0.3, but still well below that for $Mg(TFSI)_2$. An important difference for these salts from $Mg(TFSI)_2$ is that addition of MgX_2 salt adds no additional $TFSI^-$ to the solution. So, using the formula $[MgX_2]_x[BMPyrTFSI]_{1-x}$, gives $A_c = nx$ and $A_{tot} = 1-x$. Therefore, the following equation is obtained:

$$\frac{A_c}{A_{tot}} = \frac{nx}{1-x} \tag{3.13}$$

Equation 13 results in a slight upward bowing in the theoretical n curves as displayed in figure 21. The plots suggest Mg^{2+} is coordinated by approximately 2 $TFSI^-$ for MgI_2 and $Mg(ClO_4)_2$. The situation is less clear for $MgCl_2$ and $MgBr_2$, due to their limited solubility. One might expect that fewer $TFSI^-$ coordinate the Mg^{2+} in RTIL solutions of these salts as the corresponding anions of the magnesium salt likely form stronger contact ion pairs with Mg^{2+} than does $TFSI^-$.

3.3.5 Chelating Agents

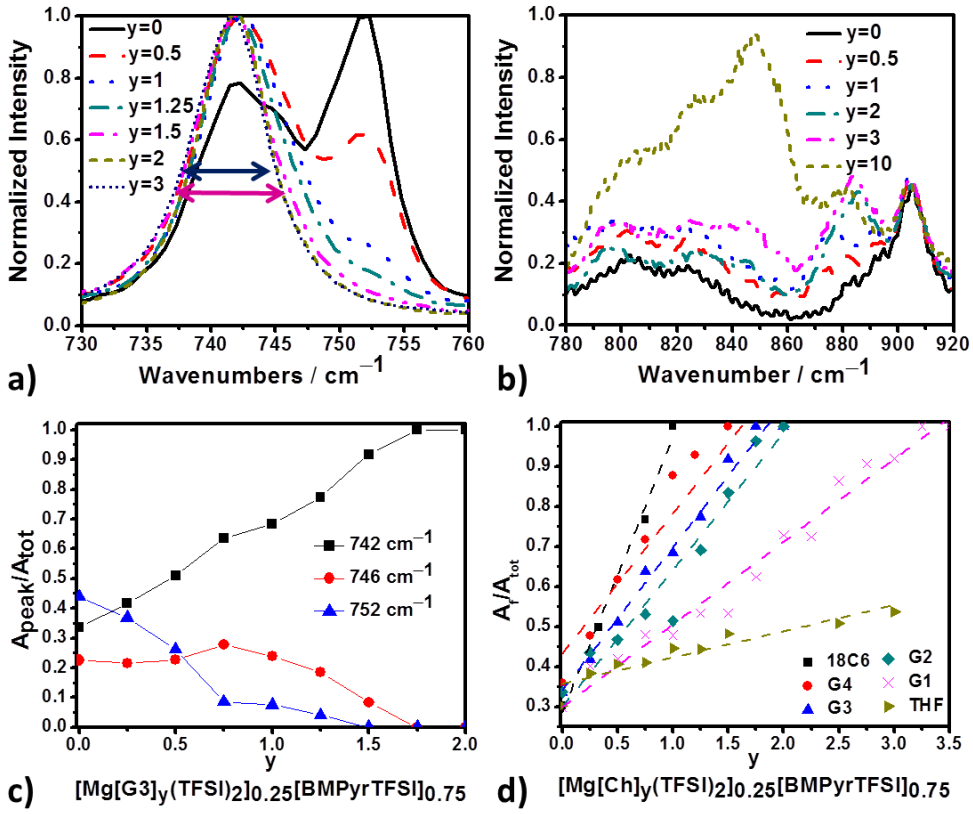

Figure 22: a) 730 cm^{-1} to 760 cm^{-1} Raman shift spectral region. Spectra compare vibrational excitations from additions of G3 to an initial $[Mg(TFSI)_2]_{0.25}[BMPyrTFSI]_{0.75}$ composition. b) Region of the spectra in which ether oxygen vibrational modes are prevalent. c) Fractional areas under the three fit peaks. d) Fraction of $TFSI^-$ that are free vs. added chelator.

The coordination of the metal cations with $TFSI^-$ can be varied drastically by adding species with a higher affinity for the metal cations.[52–66] Oligoether glymes (Gm), in particular, are known to coordinate well with Li^+ and have been extensively studied for their use in several electrolyte systems. As demonstrated previously, the preferential coordination of Li^+ with neutral glyme ethers (Gm) over $TFSI^-$ produces a reduction in

the coordinated $TFSI^-$ Raman peak.[35,53] The idea that a neutral molecule can preferentially coordinate a metal cation in favor of an anion is somewhat counterintuitive, but essentially demonstrates just how weakly coordinating $TFSI^-$ is. Bayley *et al*. have shown improved transport properties for LiTFSI/IL electrolytes when oligoethers were added.[68] Addition of the chelating groups to LiTFSI/IL electrolytes increased conductivities, decreased viscosities, increased diffusion coefficients and even increased the ionicities. Glymes, and glyme/IL mixtures have also recently been reported as potential solvents for Mg batteries, especially with $Mg(TFSI)_2$ as the salt.[26,87,88]

With the chelating strategy in mind, we investigated the addition of chelating agents to RTIL media containing Mg^{2+} salts. The chemical formula now becomes $[Mg(L)_y(TFSI)_2]_x[BMPyrTFSI]_{1-x}$, where L stands for a chelating ligand and y gives the molar ratio of the chelator with respect to Mg^{2+}. We primarily focused on glymes but also explored THF and 18-crown-6 ether (18C6) for comparison. Figure 22a-c uses triglyme (G3) as a representative example but similar trends were observed for each chelator. To acquire the data in figure 22a we began with $[Mg(TFSI)_2]_{0.25}[BMPyrTFSI]_{0.75}$ (y = 0 in above formula) solutions and subsequently added aliquots of the G3 chelating agent. It can clearly be seen that addition of G3 reduced the 752 cm^{-1} peak, indicating removal of Mg^{2+}-$TFSI^-$ bidentate pairs. Less apparent is the trend in the 746 cm^{-1} peak. The double sided arrows in 8a point out that at y = 1.5 the vibrational band is wider than at higher mole fractions of G3, indicating contributions from the 746 cm^{-1} (monodentate) band. The spectral region observed in figure 22b, 780 cm^{-1} to 920 cm^{-1}, provides further evidence for Mg^{2+}-Gm coordination. The bands below 900 cm^{-1} arise from C-O-C

stretching and CH_2 rocking modes and are broader and much weaker than the intense $TFSI^-$ bands in figure 22a.[53] The peak at 905 cm^{-1} is from the $BMPyr^+$ cation. A peak around 885 cm^{-1} is attributed to C-O-C symmetric stretching around Mg^{2+} for G3 in a Mg^{2+}-G3 complex. The 885 cm^{-1} Mg^{2+}-G3 peak is about 15 cm^{-1} higher than the equivalent Li^+-G3 complex in LiTFSI/G3 solutions reported on by Brouillette *et al*., and is 10 cm^{-1} higher than the Mg^{2+}-G2 peak found by Ha *et al*. for much more dilute $Mg(TFSI)_2$/G2 solutions.[53,87] A broad set of peaks, with the most intense band centered at 845 cm^{-1}, can be attributed to C-O-C stretching and CH_2 rocking modes for free G3, and is only observed when there is an excess of G3. Due to the weak intensities and broad nature of the peaks in this region it is much more difficult to quantify populations using these bands.

Figure 22c shows the trend from fitting the three peak model for $TFSI^-$ as a function of y for G3 additions. It is evident from the plot that bidentate coordination decreases before monodentate coordination as G3 is added. This trend was found for the other chelators as well with the "cross over point" shifting to lower L/Mg^{2+} ratios as the number of ether oxygens in the chelator increased. Interestingly, for additions of G1, the fraction of coordinated $TFSI^-$ that are bidentate is equal to the fraction that are monodentate when the ratio of G1 to Mg^{2+} is about 1.3:1. This is slightly higher than for Li[G1]TFSI (crystal refinements from single crystal X-ray diffraction data showed Li^+ in Li[G1]TFSI to be coordinated by two ether oxygens from G1, two oxygens from a bidentate $TFSI^-$ anion and one oxygen from a monodentate $TFSI^-$ anion).[53] Li^+ in Li[G1]TFSI crystals were found to exist in a slightly distorted square pyramidal

geometry. To the contrary, the measured bidentate/monodentate coordinated $TFSI^-$ ratio from the Raman data indicates that Mg^{2+} cations in $[Mg[G1](TFSI)_2]_{0.25}[BMPyrTFSI]_{0.75}$—a solution in which the G1:Mg^{2+} ratio is 1:1—likely sit in a 6-fold coordinated geometry in which two ether oxygens come from G1 and four oxygens come $TFSI^-$ anions, with about 56% of the $TFSI^-$ coordinating with bidentate interactions and 44% with monodentate interactions. The 6-fold coordinated geometry is determined by considering the coordination number of oxygens from $TFSI^-$ anions in this solution, as determined from equation 12. From the fraction of free, monodentate coordinated, and bidentate coordinated $TFSI^-$, compared with the concentration of $Mg(TFSI)_2$, equation 12 dictates that on average 4 oxygens from $TFSI^-$ anions coordinate Mg^{2+} in the $[Mg[G1](TFSI)_2]_{0.25}[BMPyrTFSI]_{0.75}$ electrolyte. From analysis of the non-glyme containing Mg^{2+}/IL solutions discussed above we know that 2 oxygens from $TFSI^-$ anions have been removed from the first coordination shell, and conclude that they must be replaced by the two G1 ether oxygens. In fact, the same analysis on each of the Gm:Mg^{2+} 1:1 solutions is consistent with the number of oxygens coming from $TFSI^-$ anions being equal to 6 – (m + 1); meaning each ether oxygen from the respective glyme occupies a spot in the 6-fold coordination shell around Mg^{2+} and that oxygens from $TFSI^-$ anions fill in the remaining coordination sites. We believe such consistency further supports the band assignments given to the respective $TFSI^-$ vibrational modes.

The trend of monodentate becoming the preferred orientation of $TFSI^-$ CIPs as more chelator ligands are added—and/or as the order of the glyme increases—seems

reasonable when considering the geometric limitation imposed by a favored octahedral coordinating arrangement. As chelating ligands crowd the space around Mg^{2+}, $TFSI^-$ anions may only be able to be in contact with Mg^{2+} through a single oxygen coordination rather than two. The declining trend of the 752 cm^{-1} mode with added ether oxygens from the chelating ligands is similar to results from an IR study of $PEO_mMg(TFSI)_2$ (PEO being poly(ethylene oxide) m = 6–40) electrolytes reported by Bakker *et al.*[89] In those PEO systems, no 752 cm^{-1} equivalent mode was observed, but a mode 3 cm^{-1} higher than the free $TFSI^-$ was observed. This indicates monodentate CIP coordination with no bidentate coordination in the PEO system, according to the present interpretation, and would make sense from a geometric standpoint, as mentioned above. The plots in figure 22d show the overall trends for each of the chelating agents and highlight the varying abilities for each chelator to form fully solvent separated ion pairs. Clearly, the more ether oxygens in the chelating molecule, the lower is the required mole fraction needed to fully remove $TFSI^-$ from Mg^{2+}. Interestingly, a solid-liquid phase separation occurred above y = 3 in some samples when THF was added as the chelating agent. The nature of the two phases is yet to be elucidated but the phase separation explains why A_f/A_{tot} does not increase much above y = 3 (we do not show THF additions above y = 3). Also, samples with G1 were found to have just under 1% of $TFSI^-$ with monodentate coordination to Mg^{2+} even at a G1:Mg^{2+} ratio of 5:1 (the linear trend in table 2 was only evaluated up to y = 3.5 for the G1 series). This is not surprising considering the findings of Rajput *et al.*, mentioned above, who predicted considerable Mg-TFSI CIPs in a 0.4M $Mg(TFSI)_2$/G1 electrolyte.[79]

Table 3: Molar ratios of chelating agents to Mg^{2+} at which all $TFSI^-$ are free, and the corresponding coordination numbers (CN) calculated from the linear trends. *Linear trend for THF only considered through y = 3.

Chelator	Ch/Mg^{2+} for $A_f/A_{tot} = 1$	CN
THF*	6.6 ± 1.0	6.6 ± 1.0
G1	3.4 ± 0.3	6.7 ± 0.6
G2	2.0 ± 0.2	6.1 ± 0.7
G3	1.8 ± 0.1	7.1 ± 0.3
G4	1.3 ± 0.1	6.7 ± 0.6
18Cr6	1.0 ± 0.1	6.2 ± 0.5

Table 2 quantifies the chelators' "strengths" from an evaluation of the linear slopes as a function of their mole fractions with respect to Mg^{2+} (y in said formula). Given are the mole fractions at which all $TFSI^-$ are free from Mg^{2+} coordination according to the respective linear trends. From these mole fractions the corresponding coordination numbers were determined by the number of available ether oxygens from each chelator (Note: standard errors depict deviations from the linear trends, as obtained through a linear regression analysis, and are a result of experimental and peak fitting uncertainties). For example, G4 has 5 ether oxygens and "frees" all $TFSI^-$ when G4/Mg^{2+} is 1.34, according to the slope, or 1.3 ± 0.1 when rounded to the nearest significant figure. So, the coordination number (CN) is given by 1.3(4)*5 = 6.7 ± 0.6 (again rounding to the nearest significant figure). These trends further suggest Mg^{2+} requires an environment in which it is coordinated by 6 oxygens, likely in an octahedral or distorted octahedral

geometry. In fact, this is consistent with several previously reported Mg^{2+} complexes.[20,84,86] With the preferred 6-coordinate complex in mind, it is not surprising that 18C6 would behave in a very similar way to a 6-ether oxygen glyme, despite the geometry difference. The Mg^{2+} cation is easily accommodated within the 18C6 cavity, becoming fully coordinated by the neutral ligand at a 1:1 18C6:Mg^{2+} ratio (the 18C6 cavity diameter is 2.68–2.86 Å and the Mg^{2+} ionic diameter is 1.44 Å).[90]

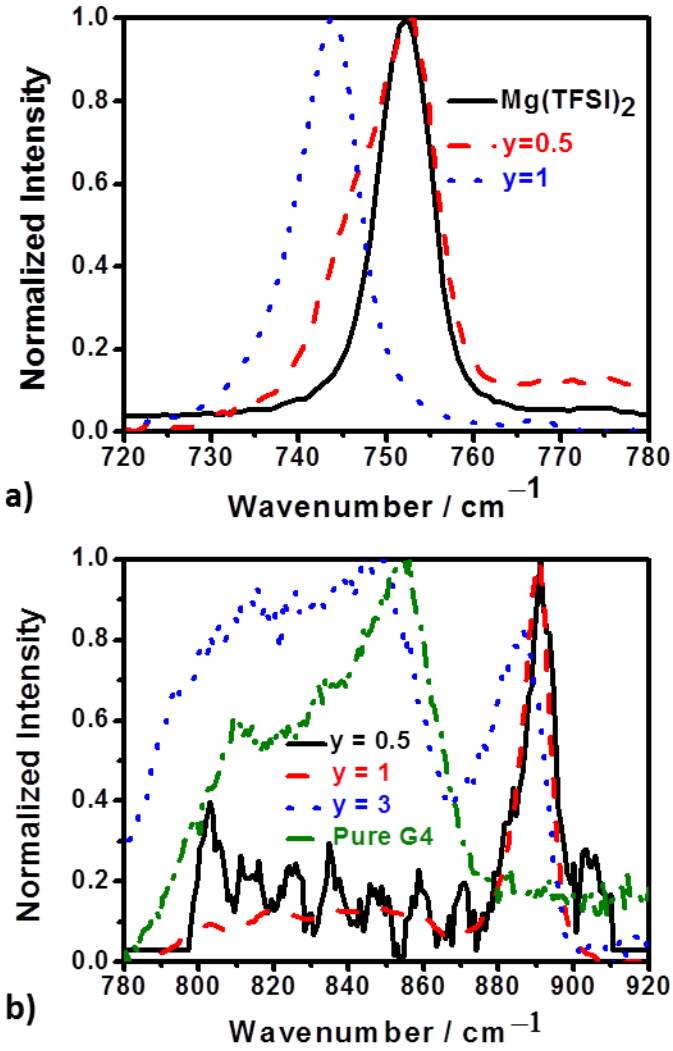

Figure 23: a) $TFSI^-$ peaks, showing the chelating ability of G4 when added to pure $Mg(TFSI)_2$. b) Region showing ether oxygen vibrational modes of $Mg(G4)_y(TFSI)_2$.

The analogous experiments using $Mg(ClO_4)_2$ as the Mg^{2+} source, and THF or diglyme as the chelators, revealed a trend in which only 3 ether oxygens were required to fully remove $TFSI^-$ coordination. This further supports the hypothesis discussed above

that solvated Mg^{2+} ions in the $Mg(ClO_4)_2$ system exist in complexes with ClO_4^- contact ion pairs, rather than being fully complexed by $TFSI^-$ alone.

3.3.6 Mg^{2+} Solvate ILs

The chelating effect of glymes is so pronounced Watanabe *et al*. were able to prepare solvate ILs by simply mixing glymes with solid LiTFSI in a 1:1 Gm:Li^+ ratio (m = 3,4).[62] Homogeneous liquids at room temperature were created, formulated by Li(Gm)TFSI. Thus, a 1:1 Li^+:Gm ratio was sufficient to remove most, if not all, $TFSI^-$ from the Li^+ coordination shell and replace them with a single glyme. $[Li(Gm)]^+$ was the suggested complexation for lithium as diffusion coefficients measured by NMR showed values for Li^+ to be very close to those of the glymes, thus inferring Li^+ ions diffuse along with their glyme ligands.[62] These glyme based solvate ILs showed significantly greater Li^+ transference numbers in comparison to Li^+ in $TFSI^-$ based ILs without neutral chelates.[62]

Here, we further report on the creation of low melting liquids comprised of mixtures of glymes (G2–G4) with $Mg(TFSI)_2$. $Mg(Gm)_y(TFSI)_2$ homogeneous liquids were prepared relatively quickly at temperatures between 70°C and 100°C by simple addition of glyme to solid $Mg(TFSI)_2$ (melting between 40°C and 80°C). These are analogous to the solvate ILs studied by Watanabe *et al*.[61–65] Figure 23 shows the Raman spectra for the $Mg(TFSI)_2$ solid salt compared to $Mg(G4)_y(TFSI)_2$. In figure 23a a drastic reduction in the coordinated $TFSI^-$ peak is observed as G4 is mixed with $Mg(TFSI)_2$. At a 1:1 G4:Mg^{2+} ratio nearly all $TFSI^-$ are spectroscopically free. Figure 23b shows Mg^{2+}-G4 coordination at 890 cm^{-1} while a broad band from 780 cm^{-1} to 870 cm^{-1} was attributed to

free G4 solvent. This is similar to the spectra of figure 22b but without the $BMPyr^+$ peak at 905 cm^{-1}. Complementing figure 23a, all G4 in the material appears to be coordinated up to a 1:1 G4:Mg^{2+} ratio. By 3:1 G4:Mg^{2+}, excess G4 clearly exists as free solvent. These findings are consistent with those of Brouillette *et al*. who were able to deduce different structural arrangements for $Li(Gm)_yTFSI$ materials, as they varied by the amount and type of glyme, using Raman as well as single crystal XRD.[53] Such solvate ILs may offer an interesting chemical route to Mg battery electrolytes as they are highly concentrated with respect to Mg^{2+} and may have improved transference numbers for the Mg^{2+} cation compared to $[Mg(TFSI)_2]_x[BMPyrTFSI]_{1-x}$ solutions. We are currently exploring the electrochemical behavior of such materials and will report on this in the near future.

Finally, we used linear sweep voltammetry (LSV) to explore the enhanced stability for glyme oxidation offered by coordination with Mg^{2+}. Figure 10a shows two distinct compositional regions with different behavior after additions of G2 to a $[Mg(TFSI)_2]_{0.25}[BMPyrTFSI]_{0.75}$ solution. In the first region, adding a half molar ratio of G2 (G2/Mg^{2+} = ½), and up to 3:1 G2:Mg^{2+}, the oxidative stability of the solution is close to 4V vs Mg. This is only about 0.25V below that of the $[Mg(TFSI)_2]_{0.25}[BMPyrTFSI]_{0.75}$ solution and about 0.5V below the pure IL. In contrast, for $y > 3$, glyme oxidizes at potentials closer to 3V, suggesting much lower glyme stability toward oxidation. Figure 10b shows similar data for $Mg(G4)_y(TFSI)_2$ solutions. In this case, at $y = 1$, good oxidative stability is observed, while for $y > 1$, poor stability is observed.

The data in figures 10a and 10b are consistent with the spectroscopic findings that a 1:1 G4:Mg^{2+} ratio has all G4 fully coordinated to Mg^{2+} while higher ratios lead to free G4. Similarly, at least 2 G2 molecules are needed to obtain a 6-fold ether oxygen coordination condition around Mg^{2+}. Beyond a 2:1 G2:Mg^{2+} ratio some G2 molecules are expected to be free in the solution. Thus, lower oxidative stability for $y \geq 3$ for G2 is expected. The oxidative stability of the glymes reported here agrees well with the findings of Watanabe *et al*.[63]

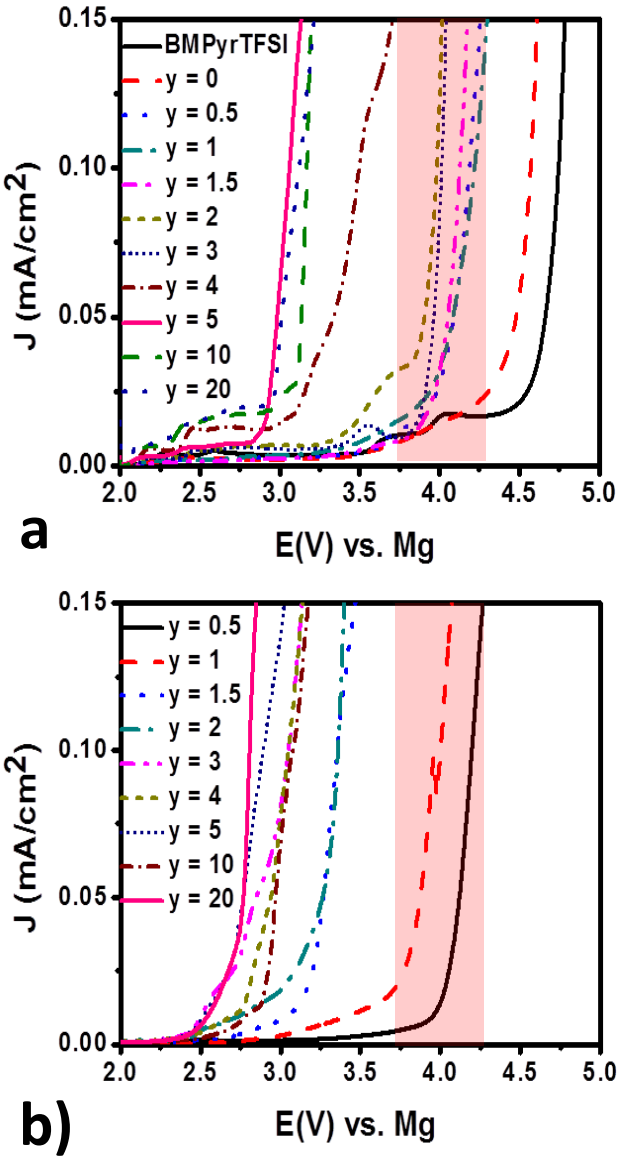

Figure 24: Linear sweep voltamograms at 1mV/s on Pt vs. a true Mg reference for a) $[Mg(G2)_y(TFSI)_2]_{0.25}[BMPyrTFSI]_{0.75}$ solutions at 25°C and b) Mg(G4)y(TFSI)2 solutions at 65°C (y = 0.5 was obtained at 80°C). The shaded areas depict oxidative stabilities of Mg^{2+} coordinated glymes. Pure BMPyrTFSI and $[Mg(TFSI)_2]_{0.25}[BMPyrTFSI]_{0.75}$ with no glyme are shown for comparison in a).

3.4 Conclusions:

Modeled fits for the intense $TFSI^-$ vibrational bands in the 715–775 cm^{-1} region have revealed the changing complexation environment as the concentration of $Mg(TFSI)_2$ is altered in $[Mg(TFSI)_2]_x[BMPyrTFSI]_{1-x}$. Measured anion populations suggest that Mg^{2+} ions exist in anionic complexes for most, if not all, of the compositional range. It was further shown that at higher $Mg(TFSI)_2$ concentrations, coordinated $TFSI^-$ prefer bidentate over monodentate interactions with Mg^{2+}. Spectral behavior for non-$TFSI^-$ containing salts suggest the salt anions remain in contact with Mg^{2+} so that the average number of $TFSI^-$ anions coordinating Mg^{2+} is reduced with respect to equivalent concentrations of $Mg(TFSI)_2$.

Furthermore, Raman data have clearly shown glymes and 18-crown-6 can be used to drastically alter the complexation environment for Mg^{2+}. Loss of $TFSI^-$ coordination as a function of added chelator is consistent with Mg^{2+} favoring oxygen coordination from ether ligands. The ability of glymes to preferentially coordinate Mg^{2+}, and to displace $TFSI^-$, is so great that $Mg(Gm)(TFSI)_2$ (m = 2–4) solvate ILs can be prepared. These were found to melt in the range 40–80°C. Raman spectra confirmed the displacement of $TFSI^-$ by glymes, consistent with expectations based on previous work with Li^+ and Mg^{2+}. Linear sweep voltammograms correlated well with the Raman data and showed that the glymes exhibit enhanced oxidative stability when complexed with Mg^{2+}.

3.5 References:

1. Yoo, H. D. *et al.* Mg rechargeable batteries: an on-going challenge. *Energy Environ. Sci.* **6,** 2265–2279 (2013).

2. Muldoon, J. *et al.* Electrolyte roadblocks to a magnesium rechargeable battery. *Energy Environ. Sci.* **5,** 5941–5950 (2012).

3. Muldoon, J., Bucur, C. B. & Gregory, T. Quest for Nonaqueous Multivalent Secondary Batteries: Magnesium and Beyond. *Chem. Rev.* **114,** 11683–11720 (2014).

4. Shterenberg, I., Salama, M., Gofer, Y., Levi, E. & Aurbach, D. The challenge of developing rechargeable magnesium batteries. *MRS Bull.* **39,** 453–460 (2014).

5. Fedorov, M. V & Kornyshev, A. A. Ionic liquids at electrified interfaces. *Chem. Rev.* **114,** 2978–3036 (2014).

6. MacFarlane, D. R. *et al.* Energy applications of ionic liquids. *Energy Environ. Sci.* **7,** 232–250 (2014).

7. Armand, M., Endres, F., MacFarlane, D. R., Ohno, H. & Scrosati, B. Ionic-liquid materials for the electrochemical challenges of the future. *Nat. Mater.* **8,** 621–9 (2009).

8. Cheek, G. T., O'Grady, W. E., El Abedin, S. Z., Moustafa, E. M. & Endres, F. Studies on the Electrodeposition of Magnesium in Ionic Liquids. *J. Electrochem. Soc.* **155,** D91–95 (2008).

9. Zhao, Q., NuLi, Y., Nasiman, T., Yang, J. & Wang, J. Reversible Deposition and Dissolution of Magnesium from Imidazolium-Based Ionic Liquids. *Int. J. Electrochem.* **2012,** 1–8 (2012).

10. Kitada, A., Kang, Y., Uchimoto, Y. & Murase, K. Room-Temperature Electrodeposition of Mg Metal from Amide Salts Dissolved in Glyme-Ionic Liquid Mixture. *J. Electrochem. Soc.* **161,** D102–D106 (2014).

11. Lu, Z., Schechter, A., Moshkovich, M. & Aurbach, D. On the electrochemical behavior of magnesium electrodes in polar aprotic electrolyte solutions. *J. Electroanal. Chem.* **466,** 203–217 (1999).

12. Vardar, G. *et al.* Electrochemistry of Magnesium Electrolytes in Ionic Liquids for Secondary Batteries. (2014).

13. Amir, N., Vestfrid, Y., Chusid, O., Gofer, Y. & Aurbach, D. Progress in nonaqueous magnesium electrochemistry. *J. Power Sources* **174,** 1234–1240 (2007).

14. Lodovico, L., Martins, V. L., Benedetti, T. M. & Torresi, R. M. Electrochemical Behavior of Iron and Magnesium in Ionic Liquids. *J. Braz. Chem. Soc.* **25,** 460–468 (2014).

15. Yoshimoto, N., Matsumoto, M., Egashia, M. & Morita, M. Mixed electrolyte consisting of ethylmagnesiumbromide with ionic liquid for rechargeable magnesium electrode. *J. Power Sources* **195,** 2096–2098 (2010).

16. Shimamura, O., Yoshimoto, N., Matsumoto, M., Egashia, M. & Morita, M. Electrochemical co-deposition of magnesium with lithium from quaternary ammonium-based ionic liquid. *J. Power Sources* **196,** 1586–1588 (2011).

17. Kakibe, T., Hishii, J., Yoshimoto, N., Egashira, M. & Morita, M. Binary ionic liquid electrolytes containing organo-magnesium complex for rechargeable magnesium batteries. *J. Power Sources* **203,** 195–200 (2012).

18. Monteiro, M. J., Bazito, F. F. C., Siqueira, L. J. a, Ribeiro, M. C. C. & Torresi, R. M. Transport coefficients, Raman spectroscopy, and computer simulation of lithium salt solutions in an ionic liquid. *J. Phys. Chem. B* **112,** 2102–2109 (2008).

19. Lassègues, J.-C., Grondin, J. & Talaga, D. Lithium solvation in bis(trifluoromethanesulfonyl)imide-based ionic liquids. *Phys. Chem. Chem. Phys.* **8,** 5629–32 (2006).

20. Lassègues, J., Grondin, J., Aupetit, C. & Johansson, P. Spectroscopic Identification of the Lithium Ion Transporting Species in LiTFSI-Doped Ionic Liquids. *J. Phys. Chem. A.* **113,** 305–314 (2009).

21. Duluard, S. *et al.* Lithium solvation and diffusion in the bis(trifluoromethanesulfonyl)imide ionic liquid. *J. Raman Spectrosc.* **39,** 627–632 (2008).

22. Umebayashi, Y. *et al.* Lithium ion solvation in room-temperature ionic liquids involving bis(trifluoromethanesulfonyl) imide anion studied by Raman spectroscopy and DFT calculations. *J. Phys. Chem. B* **111,** 13028–32 (2007).

23. Castriota, M. *et al.* Raman Investigation of the Ionic Liquid N -Methyl- N -propylpyrrolidinium Bis (trifluoromethanesulfonyl) imide and Its Mixture with LiN (SO 2 CF 3) 2. 92–96 (2005).

24. Hardwick, L. J., Holzapfel, M., Wokaun, A. & Petr, N. Raman study of lithium coordination in EMI-TFSI additive systems as lithium-ion battery ionic liquid electrolytes. *J. Raman Spectrosc.* **38,** 110–112 (2007).

25. Borodin, O., Smith, G. D. & Henderson, W. Li+ Cation Environment, Transport, and Mechanical Properties of the LiTFSI Doped N-Methyl-N-alkylpyrrolidinium+TFSI- Ionic Liquids. *J. Phys. Chem. B.* **110,** 16879–16886 (2006).

26. Nicotera, I., Oliviero, C., Henderson, W. A., Appetecchi, G. B. & Passerini, S. NMR Investigation of Ionic Liquid-LiX Mixtures: Pyrrolidinium Cations and TFSI- Anions. *J. Phys. Chem. B.* **109,** 22814–22819 (2005).

27. Saito, Y., Umecky, T., Niwa, J., Sakai, T. & Maeda, S. Existing condition and migration property of ions in lithium electrolytes with ionic liquid solvent. *J. Phys. Chem. B* **111,** 11794–802 (2007).

28. Umecky, T., Saito, Y., Okumura, Y., Maeda, S. & Sakai, T. Ionization condition of lithium ionic liquid electrolytes under the solvation effect of liquid and solid solvents. *J. Phys. Chem. B* **112,** 3357–64 (2008).

29. Matsumoto, K., Hagiwara, R. & Tamada, O. Coordination environment around the lithium cation in solid Li2(EMIm)(N(SO2CF3)2)3 (EMIm=1-ethyl-3-methylimidazolium): Structural clue of ionic liquid electrolytes for lithium batteries. *Solid State Sci.* **8,** 1103–1107 (2006).

30. Zhou, Q., Fitzgerald, K., Boyle, P. D. & Henderson, W. A. Phase Behavior and Crystalline Phases of Ionic Liquid-Lithium Salt Mixtures with 1-Alkyl-3-methylimidazolium Salts. *Chem. Mater.* **22,** 1203–1208 (2010).

31. Zhou, Q. *et al.* Phase Behavior of Ionic Liquid-LiX Mixtures: Pyrrolidinium Cations and TFSI- Anions - Linking Structure to Transport Properties. *Chem. Mater.* **23,** 4331–4337 (2011).

32. Henderson, W. A. & Passerini, S. Phase Behavior of Ionic Liquid - LiX Mixtures : Pyrrolidinium Cations and TFSI - Anions. 2881–2885 (2004).

33. Nowinski, J. L., Lightfoot, P. & Bruce, P. G. Structure of LiN(CF3S02)2, a Novel Salt for Electrochemistry. *J. Mater. Chem.* **4,** 1579–1580 (1994).

34. Giffin, G., Moretti, A., Jeong, S. & Passerini, S. Complex Nature of Ionic Coordination in Magnesium Ionic Liquid-Based Electrolytes: Solvates with Mobile Mg2+ Cations. *J. Phys. Chem. C* **118,** 9966–9973 (2014).

35. Shirai, A. *et al.* Solvation of Lithium Ion in N,N-Diethyl-N-methyl-N-(2-methoxyethyl)ammonium Bis(trifluoromethanesulfonyl)-amide Using Raman and Multinuclear NMR Spectroscopy. *Anal. Sci.* **24,** 1291–1296 (2008).

36. Dillon, R. E. A. & Shriver, D. F. Ion Transport in Cryptand and Crown Ether Lithium Salt Complexes. *Chem. Mater.* **11,** 3296–3301 (1999).

37. Brouillette, D. *et al.* Stable solvates in solution of lithium bis(trifluoromethylsulfone)imide in glymes and other aprotic solvents: Phase diagrams, crystallography and Raman spectroscopy. *Phys. Chem. Chem. Phys.* **4,** 6063–6071 (2002).

38. Henderson, W. A., Brooks, N. R., Brennessel, W. W. & Young, V. G. Triglyme-Li+ Cation Solvate Structures: Models for Amorphous Concentrated Liquid and Polymer Electrolytes (I). *Chem. mater.* **15,** 4679–4684 (2003).

39. Choquette, Y. *et al.* Sulfamides and Glymes as Aprotic Solvents for Lithium Batteries. *J. Electrochem. Soc.* **145,** 3500–3507 (1998).

40. Dillon, R. E. A. & Shriver, D. F. Influence of cation size on ionic glass formation and ionic conductivity. *Solid State Ionics* **132,** 93–99 (2000).

41. Dillon, R. E. A., Stern, C. L. & Shriver, D. F. Influence of the Anion on the Formation of Amorphous Ionically Conducting Lithium Salt Complexes with 18-C-6 and 2.2.2-Cryptand Macrocycles. *Chem. Mater.* **13,** 2516–2522 (2001).

42. Hayamizu, K., Akiba, E., Bando, T. & Aihara, Y. 1H, 7Li, and 19F nuclear magnetic resonance and ionic conductivity studies for liquid electrolytes composed of glymes and polyetheneglycol dimethyl ethers of CH3O(CH2CH2O)n CH3 (n=3–50) doped with LiN(SO2CF3)2. *J. Chem. Phys.* **117,** 5929–5939 (2002).

43. Henderson, W. A. Glyme-Lithium Salt Phase Behavior. *J. Phys. Chem. B.* **110,** 13177–13183 (2006).

44. Pappenfus, T. M., Henderson, W. A., Owens, B. B., Mann, K. R. & Smyrl, W. H. Complexes of Lithium Imide Salts with Tetraglyme and Their Polyelectrolyte Composite Materials. *J. Electrochem. Soc.* **151,** A209–A215 (2004).

45. Mandai, T., Yoshida, K., Ueno, K., Dokko, K. & Watanabe, M. Criteria for solvate ionic liquids. *Phys. Chem. Chem. Phys.* **16,** 8761–72 (2014).

46. Ueno, K. *et al.* Glyme-lithium salt equimolar molten mixtures: concentrated solutions or solvate ionic liquids? *J. Phys. Chem. B* **116,** 11323–31 (2012).

47. Yoshida, K. *et al.* Oxidative-stability enhancement and charge transport mechanism in glyme-lithium salt equimolar complexes. *J. Am. Chem. Soc.* **133,** 13121–9 (2011).

48. Yoshida, M., Tsuchiya, M., Tachikawa, N., Dokko, K. & Watanabe, M. Solvate Ionic Liquids and Their Application to Li Batteries: Glyme-Li Bis(fluorosulfonyl)amide Equimolar Complexes. *Mater. Res. Soc. Symp. Proc.* **1473,** (2012).

49. Zhang, C. *et al.* Chelate Effects in Glyme/Lithium Bis(trifluoromethanesulfonyl)amide Solvate Ionic Liquids. I. Stability of Solvate Cations and Correlation with Electrolyte Properties. *J. Phy* **118,** 5144–5153 (2014).

50. Zhang, C. *et al.* Chelate Effects in Glyme/Lithium Bis(trifluoromethanesulfonyl)amide Solvate Ionic Liquids, Part 2: Importance of Solvate-Structure Stability for Electrolytes of Lithium Batteries. *J. Phys. Chem. C* **118,** 17362–17373 (2014).

51. Angell, C. A. A New Class of Molten Salt Mixtures The Hydrated Dipositive Ion as an Independent Cation Species. *J. Electrochem. Soc.* **112,** 1224 (1965).

52. Bayley, P. M., Lane, G. H., Lyons, L. J., MacFarlane, D. R. & Forsyth, M. Undoing Lithium Ion Association in Ionic Liquids through the Complexation by Oligoethers †. *J. Phys. Chem. C* **114,** 20569–20576 (2010).

53. Angell, A. C., Ansari, Y. & Zhao, Z. Ionic Liquids: Past, present and future. *Faraday Discuss.* **154,** 9–27 (2012).

54. Appetecchi, G. B., Scaccia, S., Tizzani, C., Alessandrini, F. & Passerini, S. Synthesis of Hydrophobic Ionic Liquids for Electrochemical Applications. *J. Electrochem. Soc.* **153,** A1685–A1691 (2006).

55. Johansson, P., Gejji, S. P., Tegenfeldt, J. & Lindgren, J. The imide ion: potential energy surface and geometries. *Electrochim. Acta* **43,** 1375–1379 (1998).

56. Herstedt, M. *et al.* Spectroscopic characterization of the conformational states of the bis(trifluoromethanesulfonyl)imide anion (TFSI−). *J. Raman Spectrosc.* **36,** 762–770 (2005).

57. Shin, J.-H., Henderson, W. A. & Passerini, S. An Elegant Fix for Polymer Electrolytes. *Electrochem. Solid-State Lett.* **8,** A125–A127 (2005).

58. Fujii, K. *et al.* Conformational equilibrium of bis(trifluoromethanesulfonyl) imide anion of a room-temperature ionic liquid: Raman spectroscopic study and DFT calculations. *J. Phys. Chem. B* **110,** 8179–83 (2006).

59. Rey, I. *et al.* Spectroscopic and Theoretical Study of (CF3SO2)2N- (TFSI-) and (CF3SO2)2NH (HTFSI). *J. Phys. Chem. A* **102,** 3249–3258 (1998).

60. Xue, L., Padgett, C. W., DesMarteau, D. D. & Pennington, W. T. Synthesis and structures of alkali metal salts of bis[(trifluoromethyl)sulfonyl]imide. *Solid State Sci.* **4,** 1535–1545 (2002).

61. Seo, D. M., Borodin, O., Han, S.-D., Boyle, P. D. & Henderson, W. A. Electrolyte Solvation and Ionic Association II. Acetonitrile-Lithium Salt Mixtures: Highly Dissociated Salts. *J. Electrochem. Soc.* **159,** A1489–A1500 (2012).

62. Seo, D. M. *et al.* Solvate structures and spectroscopic characterization of LiTFSI electrolytes. *J. Phys. Chem. B* **118,** 13601–13608 (2014).

63. Qian, J. *et al.* High rate and stable cycling of lithium metal anode. *Nat. Commun.* **6,** 6362 (2015).

64. Rajput, N. N., Qu, X., Sa, N., Burrell, A. K. & Persson, K. a. The Coupling between Stability and Ion Pair Formation in Magnesium Electrolytes from First-Principles Quantum Mechanics and Classical Molecular Dynamics. *J. Am. Chem. Soc.* **137,** 3411–3420 (2015).

65. Henderson, W. A. *et al.* Glyme-Lithium Bis(trifluoromethanesulfonyl)imide and Glyme-Lithium Bis(perfluoroethanesulfonyl)imide Phase Behavior and Solvate Structures. *Chem. Mater.* **17,** 2284–2289 (2005).

66. Gutman, V. *The Donor-Acceptor Approach to Molecular Interactions*. (Plenum Press, 1987).

67. Umebayashi, Y. *et al.* Raman spectroscopic studies and ab initio calculations on conformational isomerism of 1-butyl-3-methylimidazolium bis-(trifluoromethanesulfonyl)amide solvated to a lithium ion in ionic liquids: effects of the second solvation sphere of the lithium ion. *J. Phys. Chem. B* **114,** 6513–21 (2010).

68. Fujii, K., Nonaka, T., Akimoto, Y., Umebayashi, Y. & Ishiguro, S. Solvation Structures of Some Transition Metal(II) Ions in a Room-Temperature Ionic Liquid , 1-Ethyl-3-methylimidazolium Bis(trifluoromethanesulfonyl) amide. *Anal. Sci.* **24,** 1377–1380 (2008).

69. Rudolph, W. W., Irmer, G. & Hefter, G. T. Raman spectroscopic investigation of speciation in MgSO4(aq). *Phys. Chem. Chem. Phys.* **5,** 5253–5261 (2003).

70. Bradley, M. S. & Krech, J. H. High-pressure Raman Spectra of the Acetone C-C Stretch in Binary Liquid Mixtures with Methanol. *J. Phys. Chem.* **96,** 75–79 (1992).

71. Bock, C. W., Kaufman, A. & Glusker, J. P. Coordination of water to magnesium cations. *Inorg. Chem.* **33,** 419–427 (1994).

72. Ha, S. *et al.* Magnesium(II) Bis(trifluoromethane sulfonyl) Imide-Based Electrolytes with Wide Electrochemical Windows for Rechargeable Magnesium Batteries. *Appl. Mater. Interfaces* **6,** 4063–4073 (2014).

73. Kim, I.-T., Yamabuki, K., Morita, M., Tsutsumi, H. & Yoshimoto, N. Effects of alkoxide addition on the electrochemical deposition and dissolution in triglyme-based solution dissolving magnesium bis(trifluoromethanesulfonyl)amide. *J. Power Sources* **278,** 340–343 (2015).

74. Bakker, A., Gejji, S., Lindgren, J. & Hermansson, K. Contact Ion Pair Formation and Ether Oxygen Coordination in the Polymer Electrolytes M[N(CF3SO2)2]2PEOn for M = Mg, Ca, Sr and Ba. *Polymer (Guildf).* **36,** 4371–4378 (1995).

75. Izatt, R. M., Bradshaw, J. S., Nielsen, S. A., Lamb, J. D. & Christensen, J. J. Thermodynamic and Kinetic Data for Cation-Macrocycle Interaction. *J. Chem. Rev.* **85,** 271–339 (1985).

CHAPTER 4

DESIGNER IONIC LIQUIDS FOR REVERSIBLE ELECTROCHEMICAL DEPOSITION/DISSOLUTION OF MAGNESIUM

4.1 Introduction

Figures and text in this chapter were reprinted (adapted) with permission from Watkins, T.; Kumar, A.; Buttry, D. A. Designer Ionic Liquids for Reversible Electrochemical Deposition/Dissolution of Magnesium. *J. Am. Chem.. Soc.* **2016**, 138, 641–650.

The realization of reliable battery chemistries beyond the present Li-ion systems is an important goal in the field of energy conversion and storage. The theoretical metrics of a rechargeable battery using a metallic magnesium anode (3832 mAh/cm^3 volumetric and 2205 mAh/g gravimetric capacities) have motivated significant efforts to develop electrolytes and cathode materials for secondary Mg batteries.[1–4] The fundamental requirement for an electrolyte to be compatible with the (electro)chemistries of both the cathode and anode is not trivially met in Mg-based systems. For instance, simple Mg electrolytes analogous to those of typical Li battery chemistries have yet to show reversible electrodeposition of Mg metal. To date, most reported Mg electrolytes have been derived from organometallic sources, predominantly Grignard reagents or analogues, often in concert with AlR_xCl_{3-x} (R = alkane or aryl group) to provide increased oxidative stability. In some recent systems, the $[(\mu\text{-}Cl)_3Mg_2(THF)_6]^+$ dimer and/or the $[MgCl(THF)_5]^+$ monomer have been implicated in producing reversible electrochemical deposition and dissolution.[5] These various systems have shown reversible electrodeposition of dendrite-free Mg with high coulombic efficiencies and reasonable oxidative stabilities.[4] However, halide electrolytes can be corrosive toward typical current

collecting metals, limiting their commercial applicability.[6–9] Many Mg electrolytes also have unattractive safety characteristics due to use of Grignards and/or tetrahydrofuran (THF) in the electrolyte.[2] Oligoether glymes have also been proposed as solvent systems for Mg electrolytes due in part to their lower volatility and higher thermal stabilities compared to THF.[10–13] We describe here an effort to develop Mg battery electrolytes that mitigate the above drawbacks.

In 2012 Mohtadi *et al.* demonstrated $Mg(BH_4)_2$ in tetrahydrofuran (THF) and dimethoxyethane (DME, also known as monoglyme or glyme) as the first fully inorganic and non-halide containing Mg electrolytes to show reversible Mg deposition and stripping.[14] The $Mg(BH_4)_2$ solutions were also compatible with Mg^{2+} insertion into a Mo_6S_8 Chevrel cathode—one of the only cathodes reported to have good reversibility for Mg^{2+} insertion.[15] Other reports on $Mg(BH_4)_2$ electrolytes have followed with particularly interesting insights into the solvated structure dependence on the electrochemistry and the synergistic role played by $LiBH_4$ when added to enhance the current response.[11–13,16–18] Specifically, it has been argued that longer chain oligoether glyme solvents enhance the electrochemical Mg deposition/dissolution process due to increased electron donicity and chelating abilities of the chains.[17]This suggests that solvent systems containing polyethers may be attractive for reversible Mg deposition/dissolution. It has also been shown that $LiBH_4$ aids the Mg deposition/dissolution process by co-depositing a small quantity of Li, providing another strategy for improving reversible deposition and dissolution.[17,18]

While the ether and polyether electrolytes appear promising, ideal electrolytes would be completely nonvolatile, nonflammable and thermally stable up to high

operating temperatures. This has led many groups to explore the use of ionic liquids (ILs) as electrolytes for a variety of battery systems. Many IL-based electrolytes have advantageous properties for Li-ion and post Li-ion battery chemistries.[19] For instance, many tend to be nonvolatile and nonflammable, with high thermal stability, good conductivity and a wide electrochemical window. However, despite these strengths, IL-based electrolytes have so far been hindered by high costs, relatively low rate capabilities, or generally poor performance, and have yet to find true commercial interest.

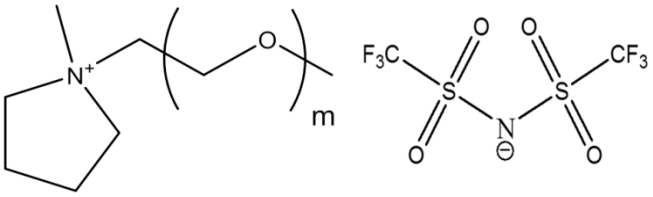

Figure 25: General molecular structure for PEGylated ionic liquids used in this study.

Ionic liquids have recently been explored as electrolytes for Mg battery systems, but so far with only limited success.[20–29] We report here for the first time reversible Mg electrodeposition/dissolution from a purely ionic liquid medium—designed to specifically enhance the Mg deposition/dissolution process. These results were achieved by synthesizing task specific ILs to meet the specific coordination conditions required for Mg deposition/dissolution from a $Mg(BH_4)_2$ source. A previous Raman spectroscopic study of the speciation state of Mg^{2+} in IL and glyme-containing IL electrolytes informed the structures of the ILs reported here, one of which has not yet been reported.[26] IL cations were synthesized in which methoxy terminated polyethylene glycol (PEG) chains were made pendent on methylpyrrolidinium cations (labeled $MPEG_mPyr^+$ where M =

methyl, m = number of ether oxygens in the PEG chain and Pyr = pyrrolidinium) in ionic liquids containing bis(trifluoromethylsulfonyl)imide ($TFSI^-$) anions as the counterion. We show that these "PEGylated" ILs (Figure 25) facilitate Mg deposition/dissolution. These task specific ILs are shown to chelate Mg^{2+} and are therefore termed "chelating ILs." This is consistent with previous terminology used by Kar *et al*., in which chelating ILs were used in electrolytes containing Zn^{2+}.[30]

The results presented here are informed by recent work from Giffin *et al.* on crystal structures and liquid state properties of materials containing $Mg(TFSI)_2$ and N-methoxyethyl-N-methylpyrrolidinium TFSI,[31] and also by a recent Raman study reported by us on speciation of Mg^{2+} in ILs containing $TFSI^-$ and various ether and polyether solvents.[26] Here we compare the electrochemical characteristics of task specific, chelating ILs, containing $Mg(BH_4)_2$ to an analogous, non-chelating, IL electrolyte. We show that proper control of Mg^{2+} speciation can provide reversible electrochemical deposition and dissolution with coulombic efficiencies over 90% and dendrite-free morphologies. These results represent the first demonstration of reversible electrochemical deposition/dissolution of Mg in an ionic liquid designed specifically for improved Mg electrochemical behavior.

4.2 Experimental

Chemicals:

Lithium bis(trifluorosulfonyl)imide (99.5% TCI America), sodium iodide (99.5% EMD Millipore), 4-toluensulfonyl chloride (≥ 98% Oakwood Chemical), iodobutane

(synthetic grade EMD Millipore), isopropyl alcohol (IPA) (99.7% Alfa Aesar), triethylene glycol monomethyl ether (≥ 97% Sigma Aldrich), sodium thiosulfate (99% Sigma Aldrich), activated carbon (decolorizing, Sigma Aldrich) and methoxypolyethylene glycol M.W. 350 (reagent grade Sigma Aldrich) were used as received. Prior to use in their respective reactions ethyl acetate (99.5% BDH), N-methyl pyrrolidine (97% Sigma Aldrich), pyridine (≥ 99% Sigma Aldrich) and dichloromethane (reagent grade BDH) were distilled over CaH_2. Acetone (Sigma Aldrich) was dried via 3Å molecular sieves prior to a single distillation before use. Toluene (Lab Chem Inc.) was distilled over sodium and benzophenone prior to use.

Synthesis of Ionic Liquids:

1-(2-(2-(2-Methoxyethoxy)ethoxy)ethyl)-1-methylpyrrolidinium bis(trifluoromethylsulfonyl)imide (*MPEG$_3$PyrTFSI*).

The general procedure was a scaled up synthesis taken from Dobbelin *et al*..[32] However, we found work up of the PEG_3I was best performed using a 5% aqueous solution of sodium thiosulfate, as described below for synthesis of $MPEG_7PyrTFSI$. We also added an additional step of dissolving the final product in a small volume of IPA and stirred over activated charcoal at 40°C overnight for purification. The final product was a lightly yellow-tinted liquid. *MPEG$_3$PyrTFSI*: ^{1}H NMR (400 MHz, $(CD_3)_2CO$): δ 4.06–4.01 (m, 2H, NCH_2CH_2O), 3.78–3.74 (m, 6H, NCH_2), 3.69–3.65 (m, 2H, OCH_2CH_2O), 3.63–3.6 (m, 4H, OCH_2CH_2O), 3.58−3.56 (m, 2H, OCH_2CH_2O), 3.48−3.45 (m, 2H,

OCH_2CH_2O), 3.29 (s, 3H, OCH_3), 3.28 (s, 3H, NCH_3), 2.33−2.27 (m, 4H, CH_2CH_2). The ^{1}H NMR spectrum is shown toward the end of the supporting information.

Methoxypolyethylene glycol (M.W. 350) bis(trifluoromethylsulfonyl)imide(MPEG$_7$PyrTFSI).

The general procedure was taken from Ganapatibhotla *et al*. and adapted for pyrrolidinium-based cations as opposed to imidazolium cations.[33] 4-toluensulfonyl chloride in dichloromethane was added dropwise to a solution of methoxypolyethylene glycol M.W. 350 and pyridine in dichloromethane at 0°C to –10°C and subsequently allowed to gradually warm back to room temperature as the reaction progressed overnight. After workup of the PEGylated tosyl (PEG_7Ts) product, described by Ganapatibhotla *et al.,* NaI powder was slowly added to PEG_7TS/acetone at room temperature and allowed to react overnight. The PEGylated iodide (PEG_7I) product was worked up, again as described by Ganapatibhotla *et al.*, by three 50 mL extractions using a 5% aqueous solution of sodium thiosulfate. The PEG_7I/toluene was then added to methylpyrrolidine and allowed to react at room temperature for 2 days. The resulting $MPEG_7PyrI$ IL was separated from the toluene organic phase and extracted 3 times with 50 mL of diethyl ether. It was then dissolved in water and stirred with decolorizing activated carbon overnight. Finally, after filtering the carbon, the $MPEG_7PyrI$ was combined with LiTFSI in water to give $MPEG_7PyrTFSI$. The $MPEG_7PyrTFSI$ was rinsed 3 times with 18 MΩ water, then diluted with IPA and stirred in activated charcoal at 40°C overnight for final purification. The IL was then dried at 80°C, under 0.4 mTorr vacuum, for ≥ 17 hours prior to use. The final product was a clear liquid. *MPEG$_7$PyrTFSI:* ^{1}H

NMR (400 MHz, $(CD_3)_2CO$): δ 4.10–4.05 (m, 2H, NCH_2CH_2O), 3.79–3.77 (m, 6H, NCH_2), 3.70–3.68 (m, 2H, OCH_2CH_2O), 3.63–3.6 (m, 4H, OCH_2CH_2O), 3.58−3.56 (m, 2H, OCH_2CH_2O), 3.48−3.45 (m, 2H, OCH_2CH_2O), 3.29 (s, 3H, OCH_3), 3.28 (s, 3H, NCH_3), 2.33−2.27 (m, 4H, CH_2CH_2). The 1H NMR spectrum is shown at the end of the supporting information.

Raman:

Raman samples were prepared and spectra acquired as described in a recent report on $[Mg(TFSI)_2]_x[BMPyrTFSI]_{1-x}$ ILs.[26] Stoichiometric amounts of $Mg(BH_4)_2$ were combined with each of the ILs and mixing was conducted at 70–100 °C until homogeneous solutions were produced. All Raman spectra were acquired at room temperature. Raman data were collected using a custom built Raman spectrometer in a 180° geometry. The samples were excited using a 100 mW Compass 532 nm laser. The laser power was controlled using neutral density filters. The laser was focused onto the sample using a 50X super long working distance Mitutoyo objective lens with a numerical aperture of 0.42. The signal was discriminated from the laser excitation using a Kaiser Laser band pass filter followed by a Semrock edge filter. The data were collected using an Acton 300i spectrograph and a back thinned Princeton Instruments liquid nitrogen cooled CCD detector. For the regions of interest, measurements were made with an 1800 nm grating from 50-1200 cm^{-1} (1 cm^{-1} resolution). Spectra were acquired for 10 seconds five times for adequate signal-to-noise levels.

A custom made Matlab GUI was used to fit pseudo Voigt functions in the 715–775 cm^{-1} region (described in the results section), in which the Lorentzian/Gaussian

characters and FWHM could be varied manually, to the raw data (fits were made with the same general parameters as described in reference 26). All raw spectra were corrected with use of a cyclohexane standard for accurate frequency determination. Spectra shown in the figures were normalized to specific peaks (indicated in the figure captions) and fluorescent backgrounds (usually not that intense) were subtracted using the baseline function in OriginPro8.

Conductivity Measurements:

Conductivities were measured with a locally designed conductivity cell that consisted of two 0.64 mm diameter Pt wires fused within a 6 mm outer diameter, 4 mm inner diameter, flint glass rod and maintained at a constant distance. The cell constant was found to be 2.9 ± 0.2 cm^{-1}, as determined from a series of 0.01 M and 0.1 M $KCl_{(aq)}$ standards at varying temperatures.

Electrochemistry:

Electrochemical experiments were conducted using CH Instruments 618 or 760 potentiostats. Cyclic voltammograms were acquired on custom made 3 mm Pt disk working electrodes, shrouded in Teflon sheaths, that were polished with 50 μm Al_2O_3, sonicated for 5 minutes in 18 MΩ purified water to remove Al_2O_3 particles, immersed in a 3:1 H_2SO_4:H_2O_2 Pirranha solution for 1 minute to remove any remaining organics, rinsed with 18 MΩ purified water and finally sonicated for an additional 5 minutes in 18 MΩ purified water before being dried in a 120 °C oven for at least 30 minutes prior to use. Three electrode cells were used with Mg ribbon counter and reference electrodes, scrapped with a razor blade prior to immersion in the electrolytes. Electrochemical cells

consisted of 25 mL three neck round bottom flasks using 1–2 mL of electrolyte. Galvanostatic deposition was done on a gold foil substrate, also in a three electrode cell with Mg reference and counter electrodes.

X-ray Diffraction (XRD):

X-ray diffractograms were collected with a PANalytical XPert Pro MRD high resolution X-ray diffractometer with a Cu K_α X-ray source using fixed divergence slits incidence option and an X'Celerator detector.

SEM and EDS:

Surface morphology of electrodeposited magnesium was studied using scanning electron microscopy (SEM-XL 30 Environmental FEG) operating at 20 kV. Elemental analysis and elemental mapping was performed by using the EDX mode (energy-dispersive X-ray spectroscopy).

4.3 Speciation of Mg^{2+} in IL electrolytes as determined by Raman Spectroscopy

Raman spectroscopy was used to study the speciation of Mg^{2+} in the various liquids examined, as well as to understand the solution environments of the other species present, including the $TFSI^-$ anions, the polyether chains and the BH_4^- anions. Figure A1 shows the Raman spectrum of an IL of composition $[Mg(BH_4)_2]_{0.3}[MPEG_7PyrTFSI]_{0.7}$ over the entire spectral range examined. It provides a good overall representation for the spectra observed for the systems explored in this work. Four main regions of interest are highlighted in the figure and are discussed below and in the supporting information.

4.3.1 2000–2700 cm^{-1} B–H stretching

The 2000–2700 cm^{-1} region contains B–H stretching modes that can be used to determine the state of coordination of BH_4^- to Mg^{2+}.[34] Figure 26a shows the spectrum of this region for an IL containing $Mg(BH_4)_2$ dissolved at various mole fractions in BMPyrTFSI. Raman bands are observed at 2200 cm^{-1} and 2363 cm^{-1}. These are similar to those observed in many metal borohydride solutions and arise from BH_4^- coordinated to metal ions. The lower frequency peak has been assigned to bridging B-H_b vibrations while the higher frequency peak has been assigned to terminal B-H_t vibrations.[14,34–37] The spectrum in figure 26a shows that all BH_4^- anions are coordinated in a bidentate fashion to the Mg^{2+} cation. These same spectral features are observed over a range of mole fractions of $Mg(BH_4)_2$ from 0.05 to 0.35, showing that BH_4^- coordination at Mg^{2+} does not change over t

Figure 26b shows the same spectral region for $Mg(BH_4)_2$ in $MPEG_3$PyrTFSI over a range of mole fractions. In addition to the bands for the bridging and terminal B-H vibrations, a new Raman band is observed at 2254 cm^{-1}. This band is more intense (relative to the B-H_b and B-H_t bands) at low mole fractions of $Mg(BH_4)_2$. Figure 26c shows that a similar band is observed for $Mg(BH_4)_2$ in $MPEG_7$PyrTFSI over the entire mole fraction range explored. Again, the band intensity is higher relative to the B-H_b and B-H_t bands at lower mole fractions of $Mg(BH_4)_2$, and is more prominent than is observed in the $MPEG_3$PyrTFSI system at equivalent compositions. We believe this band is due to "free" BH_4^- (i.e. not coordinated to Mg^{2+}). To explore this assignment various materials containing BH_4^- were examined in environments where one might expect "free" (i.e. unbound) BH_4^-.

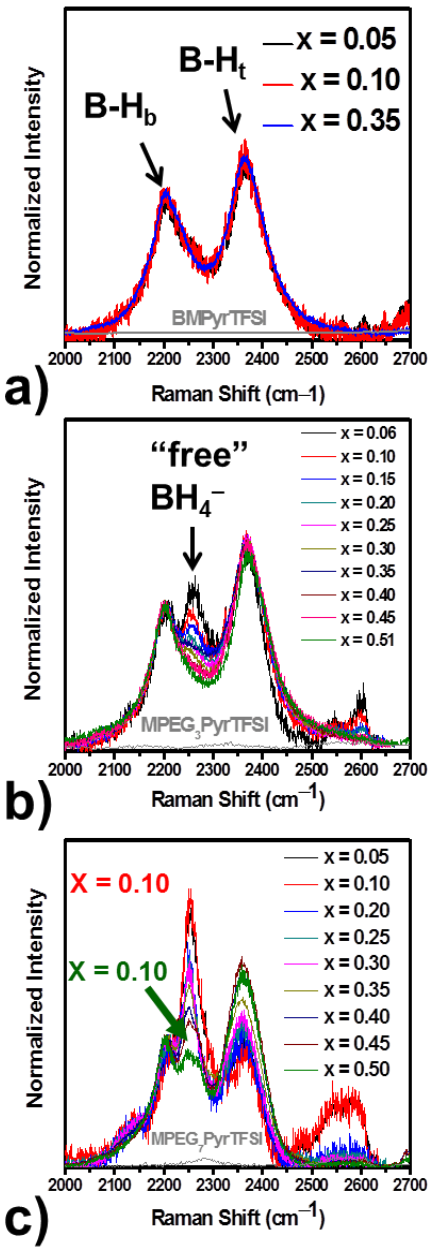

Figure 26: Raman spectra in the B-H stretching region at given molar fractions of $Mg(BH_4)_2$ (x) for a) BMPyrTFSI, b) $MPEG_3PyrTFSI$ and c) $MPEG_7PyrTFSI$. Gray curves, without any peaks, in each figure are the spectra of the respective pure IL. All spectra were normalized using the 2200 cm^{-1} peak.

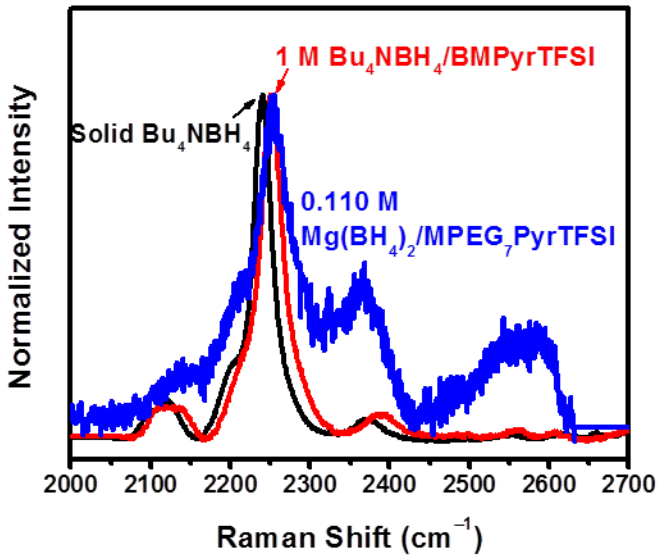

Figure 27: Raman spectra in the B-H stretching region for solid Bu_4NBH_4 (black), 1 M Bu_4NBH_4/BMPyrTFSI (red) and 0.110 M $Mg(BH_4)_2$/$MPEG_7$PyrTFSI (blue). All spectra in this figure were normalized to their most intense peak.

Figure 27 shows the Raman spectrum of solid tetrabutylammonium borohydride (Bu_4NBH_4), 1 M Bu_4NBH_4 dissolved in BMPyrTFSI and 0.110 M $Mg(BH_4)_2$ dissolved in $MPEG_7$PyrTFSI. Solid Bu_4NBH_4 shows a peak at 2250 cm^{-1}. 1 M Bu_4NBH_4 in BMPyrTFSI gives a peak at 2254 cm^{-1}, as does 0.110 M (x = 0.05) $Mg(BH_4)_2$ in $MPEG_7$PyrTFSI. These bands are consistent with those observed in previous Raman spectra for "free" (uncoordinated) BH_4^-. For example, $LiBH_4$ shows a peak at 2247 cm^{-1} in diethyl ether and 2265 cm^{-1} in liquid ammonia.[35,38] A peak equivalent to the 2254 cm^{-1} peak is also observed in solid alkylammonium salts of the tetrahydroborate family.[39] For example, solid tetramethylammonium tetrahydroborate (Me_4NBH_4) shows a peak at 2268 cm^{-1}. Based on these previous observations, we assign the 2254 cm^{-1} band in Figures 26

and 27 to uncoordinated BH_4^-. These results show that some BH_4^- is displaced from the Mg^{2+} center in these PEGylated ILs, with the extent of displacement increasing with the length of the polyether chain. This is consistent with conclusions from previous studies of $Mg(BH_4)_2$ in glyme solvents, and in a polyethylene oxide polymer matrix, which also suggested that some BH_4^- dissociation was being caused by complexation from ether oxygens.[14,17] As described below, we believe this displacement of BH_4^- impacts the electrochemical deposition/dissolution of the Mg^{2+}/Mg redox couple, generally improving the electrochemical behavior.

Comparison of the $MPEG_3$PyrTFSI results (Figure 26b) with the $MPEG_7$PyrTFSI results (Figure 26c) shows that the longer PEG chains in the latter are more effective at inducing displacement of the BH_4^-, as judged by the much more intense band for free BH_4^- in $MPEG_7$PyrTFSI. This will be revisited below in comparing the electrochemical deposition/dissolution of Mg in these two ionic liquids.

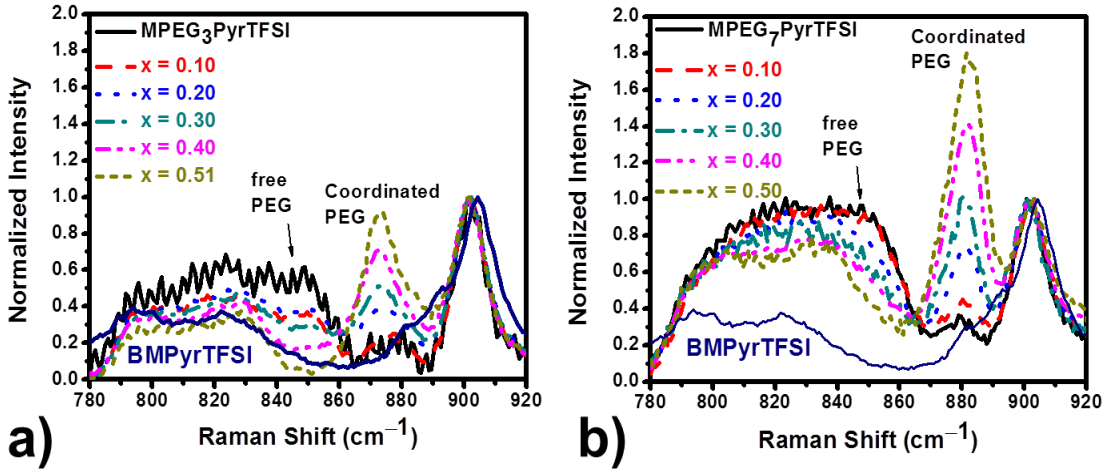

Figure 28: C-O-C stretching and CH_2 rocking regions for the two PEG-IL systems reported in this work. Each shows how the free and coordinated PEG modes change as the mole fraction of $Mg(BH_4)_2$ (x) is varied. a) $[Mg(BH_4)_2]_x[MPEG_3PyrTFSI]_{1-x}$ b) $[Mg(BH_4)_2]_x[MPEG_7PyrTFSI]_{1-x}$. The spectra in this region for BMPyrTFSI is shown in navy blue and labeled in each figure. Each of the spectra were normalized to their respective ca. 902 cm^{-1} (Pyr^+) peaks.

4.3.2 780–920 cm^{-1} C-O-C stretching and Mg-O coordination

The 780–920 cm^{-1} spectral region shows bands associated with CH_2 rocking and C–O–C stretching modes for the PEG-IL systems.[40] Figure 28 shows this region as a function of $Mg(BH_4)_2$ mole fraction (x) in $[Mg(BH_4)_2]_x[MPEG_mPyrTFSI]_{1-x}$ solutions. The Raman band for the pure BMPyrTFSI IL is also shown. The dominant bands in this region in the PEGylated IL are those that make up the broad spectral feature that stretches from 780 to 860 cm^{-1}. These vibrational modes are attributed to the non-coordinating PEG chains, specifically to C-O-C stretches.[40] These were discussed previously by us in a study of polyether interactions with Mg^{2+}, where it was demonstrated that these modes shift when the polyether oxygens are coordinated to Mg^{2+}.[26] There is also a weak, broad feature from 780 to 850 cm^{-1} and a stronger, sharper feature centered at ca. 902 cm^{-1},

both attributed to the parent Pyr^+ cation moiety (both are observed in the BMPyrTFSI IL). Figure 28a shows the variation within this region as the mole fraction of $Mg(BH_4)_2$ is increased in the $MPEG_3$PyrTFSI system. At more dilute concentrations of $Mg(BH_4)_2$, and in the pure PEG-IL, the dominant bands are those that make up the broad feature from 780 to 860 cm^{-1}. These vibrational modes are attributed to the non-coordinating (free) PEG chains. The peak arising at ca. 875 cm^{-1} is produced when the PEG chains are coordinated to Mg^{2+}. Mg^{2+} coordination also causes the broad feature due to vibrations from unbound polyether C-O-C groups to decrease, as can be seen in the figure. This coordination behavior between Mg^{2+} (from $Mg(BH_4)_2$) and the ether oxygen chains is reminiscent of the observations made for $Mg(TFSI)_2$/BMPyrTFSI, to which glyme chelators were added.[26] In Figure 28b the same region is shown for the $MPEG_7$PyrTFSI system. Again, it is evident that free PEG modes are reduced, and the coordinated PEG mode(s) enhanced, as the $Mg(BH_4)_2$ mole fraction is increased. However, the increase in the coordinated peak (ca. 880 cm^{-1}) in the $MPEG_7$PyrTFSI system is more dramatic, while the decrease in the free PEG band is more subtle, as the fraction of $Mg(BH_4)_2$ is increased. This suggests that the fraction of ether oxygens involved in coordinating Mg^{2+} is higher in the $MPEG_7$PyrTFSI system, meaning that this fraction depends on the chain length and coordination from other ligands. The present results show that the PEG chains do in fact chelate the Mg^{2+} species, despite the close proximity of the positive charge from the parent pyrrolidinium moiety.

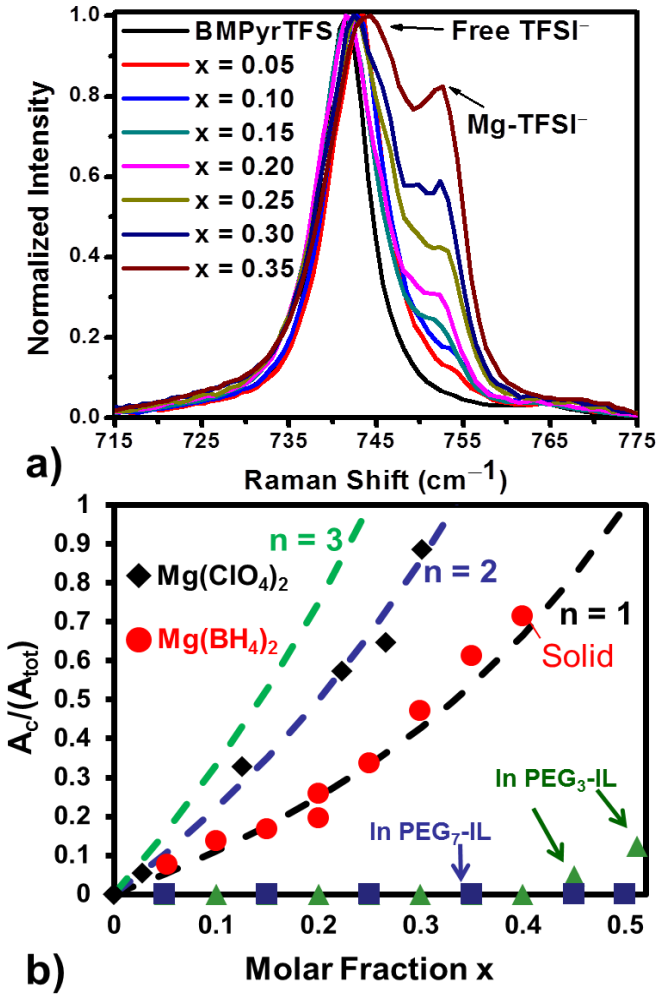

Figure 29: a) Raman spectra (715–775 cm^{-1}) for $[Mg(BH_4)_2]_x[BMPyrTFSI]_{1-x}$ electrolytes. b) Fraction of $TFSI^-$ in coordination with Mg^{2+} (A_c/A_{tot}) as a function of the molar fraction (x) of $Mg(BH_4)_2$ (**red circles**) and $Mg(ClO_4)_2$ (**black diamonds**) in BMPyrTFSI. Also shown are values for a series of $Mg(BH_4)_2$/$MPEG_3$PyrTFSI electrolytes (**green triangles**) and $Mg(BH_4)_2$/$MPEG_7$PyrTFSI electrolytes (**blue squares**). Dashed lines represent the theoretical trends for the average number of $TFSI^-$ coordinating Mg^{2+} (n) for n = 1, 2 and 3.

4.3.3 715–775 cm^{-1} Coordination Sensitive $TFSI^-$

We previously described a Raman study of the coordination of $TFSI^-$ at Mg^{2+} in various ionic liquids.[26] That analysis depends on quantification of several Raman bands in the 715 to 775 cm^{-1} region. Specifically, a band at 742 cm^{-1} is attributed to free (non-metal ion coordinating) $TFSI^-$, and a band at 752 cm^{-1} is attributed to Mg^{2+} coordinated $TFSI^-$.[26,41–49] Analysis of the relative intensities of these bands (and others in this region) provides information about the number of $TFSI^-$ species coordinated per Mg^{2+} (and the state of the coordinated $TFSI^-$ such as mono versus bidentate coordination and coordination in aggregate ion pairs).[26,41–49] We refer to the number of coordinated $TFSI^-$ anions per Mg^{2+} center as the solvation number, n. Figure 29a shows how the 752 cm^{-1} band attributed to $TFSI^-$ coordinated to Mg^{2+} increases as the $Mg(BH_4)_2$ mole fraction is increased in the BMPyrTFSI IL. This shows that $TFSI^-$ coordinates to Mg^{2+} under these conditions. Figure 29b shows a plot derived from these data giving the fraction of coordinated $TFSI^-$ versus mole fraction of $Mg(BH_4)_2$. The fraction of $TFSI^-$ coordinated to Mg^{2+} was found by integrating under the areas of Voigt peak fits for the raw data. An example fit is shown in the supporting information (Figure A3). These fits are consistent with previous work on Mg-TFSI systems.[25,26,31] Also plotted in figure 29b are theoretical curves that correspond to what would be expected for one, two or three coordinated $TFSI^-$ species per Mg^{2+} at given mole fractions of a MgX_2 salt ($X \neq TFSI^-$), obtained using a previously published treatment.[26] The data for $Mg(BH_4)_2$ agree with the n = 1 curve, showing that one $TFSI^-$ coordinates to Mg^{2+} for the full composition range (note: the x = 0.40 composition resulted in a solid at room temperature, all other mixtures were

liquids). This is consistent with a speciation for Mg^{2+} of $[Mg(BH_4)_2TFSI]^-$ in this medium. This speciation is consistent with the data in Figure 26a above showing that, under these conditions, all BH_4^- species are involved in bidentate contact ion pair coordination with Mg^{2+}.

Figure 29b also shows data derived from experiments using $Mg(ClO_4)_2$ as the Mg^{2+} source. These data show that the solvation number for $TFSI^-$ is two in this case, suggesting that ClO_4^- is more weakly bound than BH_4^-, which appears to lead to displacement of one of the two ClO_4^- anions under these conditions. This shows that this speciation analysis allows differentiation of systems that behave differently with respect to anion binding to the metal center.

Figure 29b also shows data for a range of compositions from the $[Mg(BH_4)_2]_x[MPEG_3PyrTFSI]_{1-x}$ and $[Mg(BH_4)_2]_x[MPEG_7PyrTFSI]_{1-x}$ systems. These data show that there is no detectable $TFSI^-$ coordination to Mg^{2+} up to x = 0.4 in the $MPEG_3PyrTFSI$ system, and very little above that value (up to a 1:1 mixture of $Mg(BH_4)_2$ with the $MPEG_3PyrTFSI$ IL). For the $MPEG_7PyrTFSI$, there is no detectable $TFSI^-$ coordination up to x = 0.5. This suggests that the PEGylated ILs are very effective at sequestering Mg^{2+} and preventing its coordination by $TFSI^-$.

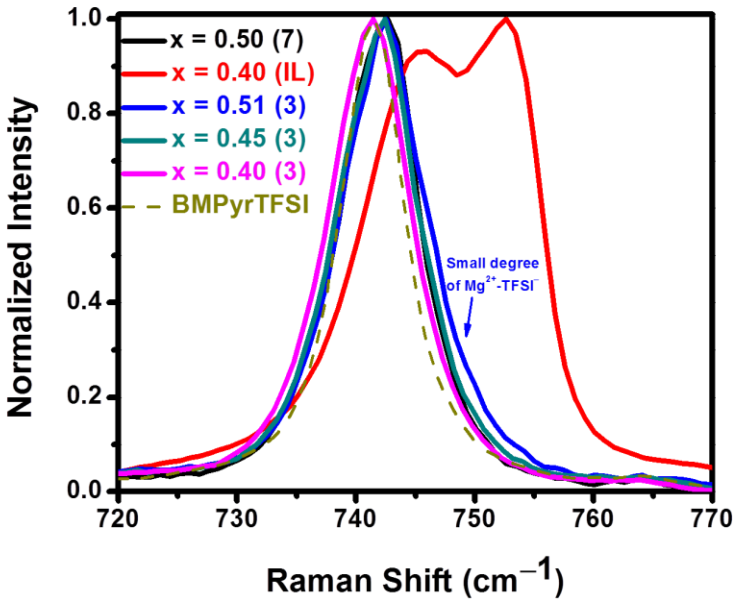

Figure 30: 715–775 cm^{-1} region comparing electrolytes with given mole fractions of $Mg(BH_4)_2$ (indicated by x) in the different IL systems (notated in the figure as (**7**) for $MPEG_7PyrTFSI$, (IL) for BMPyrTFSI and (**3**) for $MPEG_3PyrTFSI$). The 742 cm^{-1} mode is also shown for pure BMPyrTFSI (gold dashed curve).

Figure 30 shows spectra in this same region for a number of different solutions of $Mg(BH_4)_2$ at various (high concentration) mole fractions in BMPyrTFSI, $MPEG_3PyrTFSI$ and $MPEG_7PyrTFSI$. No evidence for coordinated $TFSI^-$ (or a small degree of coordination at high concentrations of $Mg(BH_4)_2$ in $MPEG_3PyrTFSI$) is observed except in BMPyrTFSI, showing that quite high concentrations of Mg^{2+} species can be obtained in the PEG-IL media without inducing $TFSI^-$ coordination. As described below, we believe the suppression of $TFSI^-$ coordination at Mg^{2+} in these PEGylated ILs provides some protection against $TFSI^-$ fragmentation under reducing conditions, which improves the electrochemical performance of Mg cycling.

4.4 Electrochemical Performance of Mg^{2+}/Mg in ILs

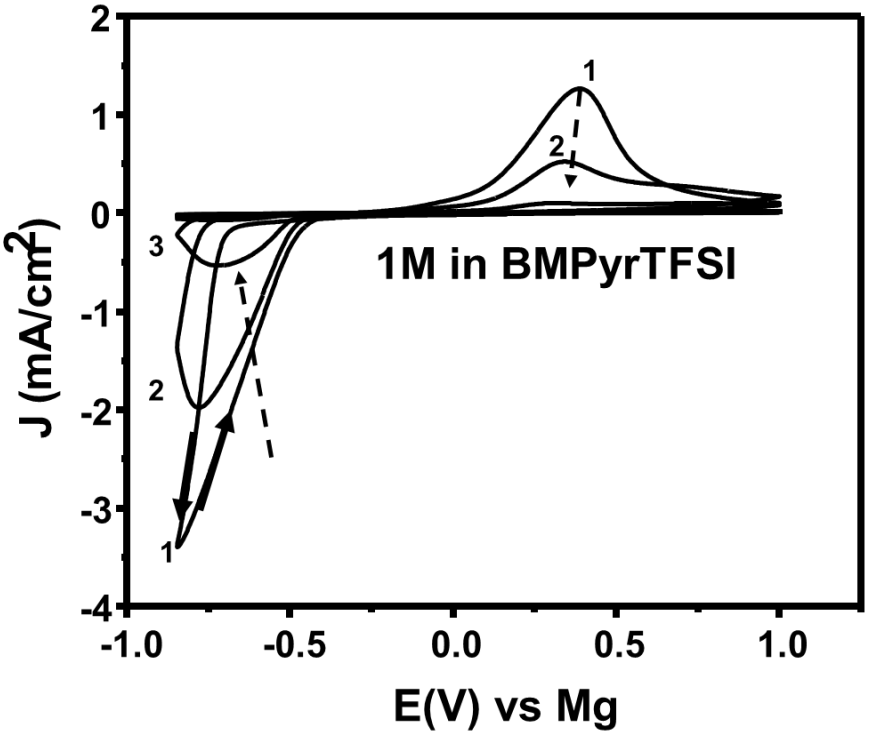

Figure 31: Successive cyclic voltammograms for 1 M $Mg(BH_4)_2$/BMPyrTFSI, at 25 mV/s.

Figure 31 shows repetitive cyclic voltammograms for Mg deposition/dissolution for a solution of $Mg(BH_4)_2$ in BMPyrTFSI along with a plot of charge versus cycle number. As can be seen, the deposition is not reversible, with rapid suppression of the electrochemical response from Mg. This behavior is typical for Mg in systems containing $TFSI^-$.[24] Figure 32 shows the cyclic voltammograms for electrochemical deposition/dissolution of Mg from $Mg(BH_4)_2$ in solutions of either the $MPEG_3TFSI$ IL or the $MPEG_7TFSI$ IL, along with plots of charge versus cycle number for the first ten cycles. Many different mole fractions of $Mg(BH_4)_2$ in these ILs were examined. The data

for other concentrations are given in the supporting information (Figures A4–A6). The concentrations shown in Figures 31 and 32 were the ones that gave the highest current densities. The room temperature conductivities for these solutions were 0.5 ± 0.1 mS/cm^2, 0.38 ± 0.01 mS/cm^2 and 0.24 ± 0.02 mS/cm^2 for the 1 M $Mg(BH_4)_2$/BMPyrTFSI, 0.5 M $Mg(BH_4)_2$/$MPEG_3$PyrTFSI and 0.5 M $Mg(BH_4)_2$/$MPEG_7$PyrTFSI, respectively. These conductivities are an order of magnitude lower than typical Li-ion electrolytes but still relatively high considering the high viscosities of the media. The relationship between current density and mole fraction of $Mg(BH_4)_2$ is complicated for these IL solutions, since increasing $Mg(BH_4)_2$ leads to viscosity increases that can reduce the current density. Figure 33 shows plots of coulombic efficiency and stripping charge versus cycle number for the experiments shown in Figures 31 and 32. These results show a marked improvement in reversibility of the deposition process compared to the data in Figure 31.

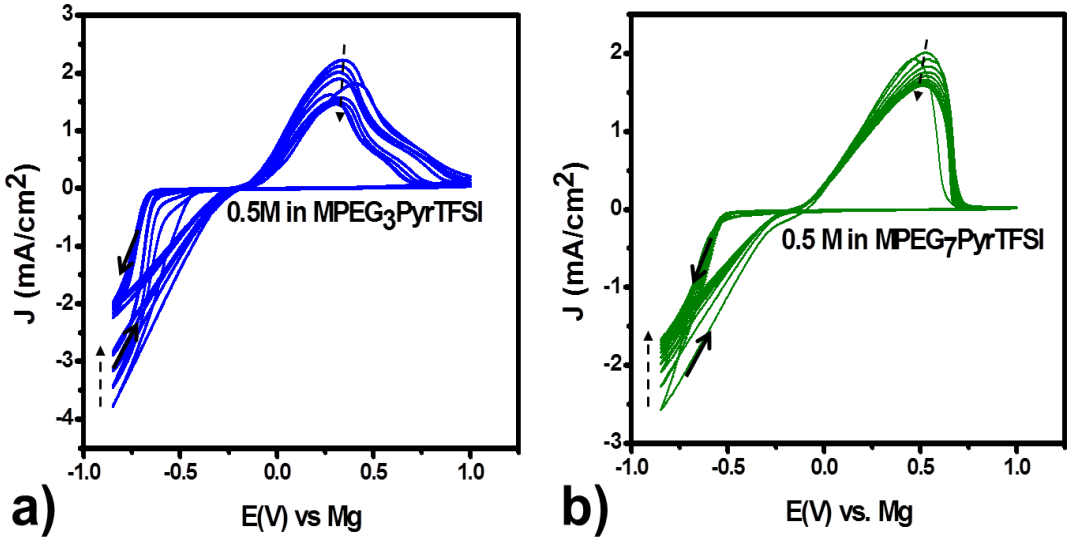

Figure 32: Successive cyclic voltammograms for a) 0.5 M $Mg(BH_4)_2$/MPEG$_3$PyrTFSI and b) 0.5 M $Mg(BH_4)_2$/MPEG$_7$PyrTFSI, at 25 mV/s.

Oxidative stability of the electrolyte is also important to the electrochemical performance of a battery electrolyte. Oxidative stability can affect the choice of cathode material and current collector. We measured the oxidative stability for the 0.5 M $Mg(BH_4)_2$/MPEG$_7$PyrTFSI electrolyte (the electrolyte with the best electrochemical characteristics), using linear sweep voltammetry (LSV). Results show that the potential of oxidation varies with the chosen electrode (Figure A7). We found the $Mg(BH_4)_2$/MPEG$_7$PyrTFSI electrolyte to be most stable on stainless steel 316 followed by glassy carbon. It was least stable on the two noble metal electrodes used (Pt and Au). This oxidative stability trend is actually the opposite of that found for Grignard-based Mg battery electrolytes, as they tend to corrode steel.[9] These oxidative stability findings correlate well with previous findings for $Mg(BH_4)_2$ in ethereal solvents.[14]

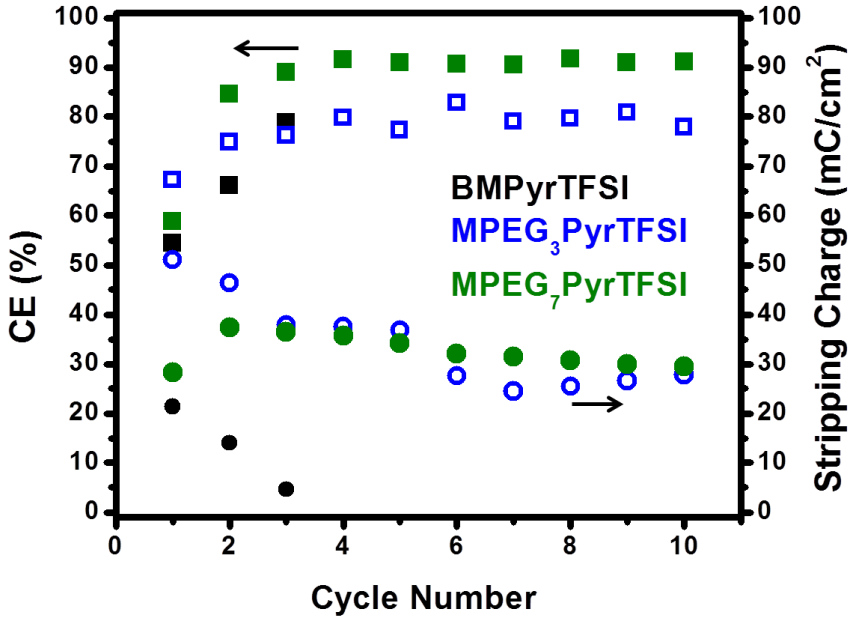

Figure 33: Coulombic efficiencies (CE) (squares) and stripping charges (circles) for each cycle in the given systems (from figures 6 and 7). Data for the **BMPyrTFSI** electrolyte is presented as **solid black** data points. Data for the **MPEG$_3$PyrTFSI** is presented as **open blue** data points. Data for the **MPEG$_7$PyrTFSI** electrolyte is presented as **solid green** data points.

The conditions in Figure 32b were used for a galvanostatic deposition of Mg at 0.1 mA/cm^2 for 16 hours, followed by characterization of the deposit. The first 15 minutes of the potential versus time trace for this experiment is shown in the supporting information Figure A8. Figure 34 shows the XRD for the deposit. The XRD pattern reveals a preferred orientation of the deposited Mg which is consistent with previous literature findings.[50] The Mg(002) diffraction peak is much weaker than the Mg(100), Mg(101) and Mg(110) peaks. The Au K_α peaks from the substrate are far more intense than the Mg peaks and are cut off before their respective peak intensities. The XRD demonstrates deposition of metallic Mg, with no evidence for other phases being present.

Figures 35a-c show successively closer views of the deposit obtained by SEM. Figure 35c gives a good representation of the Mg surface morphology which appears to be relatively smooth, without sign of dendritic growths. Figure 35d gives the EDS spectrum from an area in which no underlying Au substrate is exposed. A very strong Mg peak is observed along with a very weak O peak from the native oxide on the Mg surface, consistent with Mg deposition and absence of oxide precipitation or competing reduction processes such as $TFSI^-$ reduction, which leads to surface fouling (see below). In the supporting information, EDS elemental maps are shown for the area in Figure 35b which reinforce the lack of significant oxygen associated with the deposit (Figure A9). The analogous deposition experiment with 0.75 M $Mg(BH_4)_2$ in BMPyrTFSI gave a deposit with significant C, F, S, and O content as determined by EDS. The EDS spectrum of this deposit is shown in Figure A10. These results suggest that deposition in the $Mg(BH_4)_2$/BMPyrTFSI solution produces substantial decomposition of $TFSI^-$ and consequent surface fouling while the 0.5 M $Mg(BH_4)_2$/$MPEG_7$PyrTFSI deposition condition produces a "clean" Mg deposit with no

evidence of $TFSI^-$ fragmentation or surface fouling.

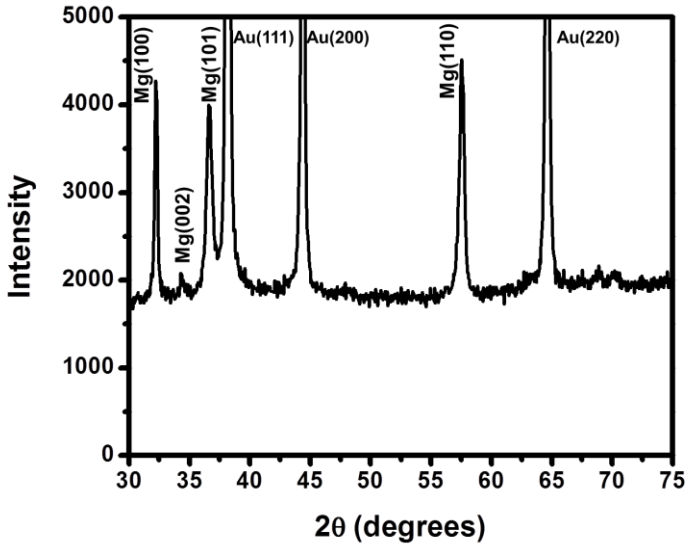

Figure 34: XRD pattern showing Mg deposit and Au substrate peaks.

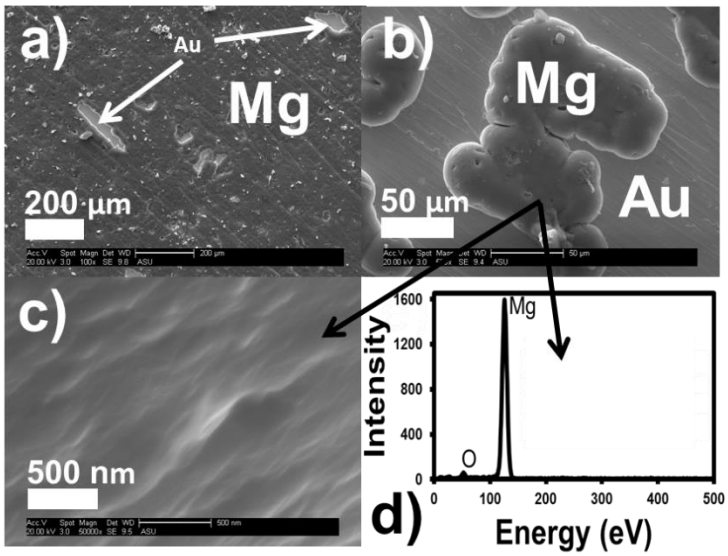

Figure 35: SEM images a), b), c) and e) are SEM images at 39x, 100x, 500x and 50,000x respectively. f) EDS spectrum for sample portion in image (e).

4.5 Effects of Mg^{2+} Speciation on Electrochemical Behavior

The data above represent the first demonstration of reversible electrochemical deposition/dissolution of bulk Mg in a task-specific ionic liquid system. They show that high coulombic efficiencies (≥ 90%) can be obtained under these conditions, and that deposition can be achieved without significant surface fouling. These results are now discussed within the context of past experimental and theoretical studies of Mg^{2+} speciation and resulting reactivity in a variety of systems.

Taken together, the spectroscopic data shown here, and the previous Raman study[26] of $Mg(TFSI)_2$ dissolved in BMPyrTFSI or glyme-containing BMPyrTFSI, reveal that Mg^{2+} speciation in IL systems is both measureable and controllable. For ILs containing only $TFSI^-$ anions and no ether or polyether solvents, Mg^{2+} is typically found as $Mg(TFSI)_3^-$. If polyether solvents or ionic liquid cations bearing pendent polyether chains are added such that the molar ratio of the total number of ether oxygens to Mg^{2+} is large (e.g. > 5 or 6), the ether oxygens displace $TFSI^-$, producing free $TFSI^-$ and Mg^{2+} bound in a neutral coordination environment of ether oxygens. The number of ether oxygens needed to fully displace all $TFSI^-$ anions depends on the length of the polyether chain and its relative concentration. The ease with which ether oxygens displace $TFSI^-$ is due to the relatively weak binding of $TFSI^-$ to Mg^{2+}.[16] For polyether solvents, $TFSI^-$ displacement has been shown to improve the electrochemical behavior of the Mg^{2+}/Mg redox system.[51–53]

The situation when the source of Mg^{2+} is $Mg(BH_4)_2$ rather than $Mg(TFSI)_2$ is similar, though there are important differences. As shown above, when $Mg(BH_4)_2$ is dissolved in ILs containing $TFSI^-$, some $TFSI^-$ coordination will occur. In this case, the predominant speciation for Mg^{2+} appears to be $[Mg(BH_4)_2TFSI]^-$. As shown above, if polyether chains pendent on IL cations are present, $TFSI^-$ will be displaced. If the ratio of ether oxygens to Mg^{2+} is sufficiently high, there is also significant displacement of BH_4^- from the Mg^{2+} center. Without Raman scattering cross-sections for the bound and free BH_4^- species, one cannot quantitatively obtain the degree of dissociation of BH_4^- in these conditions. However, the data in Figure 26c suggests that substantial displacement of at least one of the bound BH_4^- anions occurs when a sufficient number of polyether oxygens are present. In this case one possible speciation for Mg^{2+} would be $[(PEG)Mg(BH_4)]^+$, where PEG represents a generic polyether chain or chains. This type of speciation was suggested in an earlier study of $Mg(BH_4)_2$ in a polyethylene oxide matrix.[17] In that case, reversible electrochemical deposition and dissolution of Mg was observed with good coulombic efficiency. These results suggest that the PEGylated ILs provide a coordination environment conducive to reversible Mg^{2+}/Mg electrochemistry.

Table 4: Comparison of data for Mg deposition/dissolution in $Mg(BH_4)_2$ electrolytes. C is the concentration of $Mg(BH_4)_2$, Cyc 1 and Cyc 10 denote the first and tenth consecutive cycles for acquired CVs, respectively, CE is coulombic efficiency in the respective cycles, J_a is the anodic current density for the stripping current and ν is the scan rate used.

		CE (%)		Cyc 1		
medium	C (M)	Cyc 1	Cyc 10	J_a (mA/C·m^2)	ν (mV/s)	ref
G4	0.01	84	NA	0.3	20	17
G3	0.01	81	NA	0.075	20	17
G2	0.01	77	NA	0.05	20	17
G1 (DME)	0.1	67	NA	0.25	5	14
THF	0.5	40	NA	0.032	5	14
0.6 M $LiBH_4$/G1	0.18	94	NA	25	5	14
1.5 M $LiBH_4$/G2	0.1	99	NA	12.5	20	11
PEO @ 100 °C	10 wt %	98	NA	0.3	20	17
BMPyrTFSI	1	55	NA	1.25	25	present work
$MPEG_3$PyrTFSI	0.5	67	78	2	25	Present work
$MPEG_7$PyrTFSI	0.5	59	90	2	25	Present work

Table 4 compares results from a variety of past studies with those presented here. With the exception of systems containing $LiBH_4$ additive, only one previous study shows a higher CE, which is for the case of $Mg(BH_4)_2$ incorporated into a polyethylene oxide (PEO) matrix.[17] However, even at a temperature of 100°C, that system only provides a current density of 0.3 mA/cm^2, nearly an order of magnitude lower than that reported here. The best current densities for previous studies of $Mg(BH_4)_2$ in ether solvents are also an order of magnitude lower than those reported here. We believe the high currents observed in the present work result from the high concentration of $Mg(BH_4)_2$ that can be dissolved in these PEGylated ILs. Two entries in the table report high CE and current density values for cases with added $LiBH_4$. Those are not discussed further since the presence of Li^+ can lead to a variety of effects not related to Mg^{2+} speciation.[18]

We believe the attractive electrochemical performance observed in the present case is related to Mg^{2+} speciation in the PEGylated ILs. There may be a variety of ways in which speciation influences CE. We speculate on a few here. The first is through displacement of $TFSI^-$ from the Mg^{2+} center to prevent unwanted reactions of $TFSI^-$. There have been previous discussions of the potentially beneficial effects of removal of $TFSI^-$ from the primary coordination sphere of Mg^{2+}. This was discussed by Rajput *et al.* who presented theoretical results suggesting that $TFSI^-$ coordination to Mg^{2+} during the electrodeposition process might lead to transient formation of a Mg(I)-$TFSI^-$ radical intermediate that could lead to reductive fragmentation of the $TFSI^-$ anion.[16] Their quantum chemical calculations predicted that fragmentation of $TFSI^-$ in this intermediate was exothermic, suggesting a likely decomposition pathway. This might lead to coulombic inefficiencies and surface fouling due to accumulation of the resulting fragments at the interface. The present results are entirely consistent with those findings. We observe the highest CE for the $Mg(BH_4)_2$/$MPEG_7PyrTFSI$ system in which $TFSI^-$ displacement from the Mg^{2+} center was essentially complete. EDS examination of the Mg deposit shows no detectable $TFSI^-$ fragmentation products (Figure 35). In contrast, we observe irreversible cycling and high atomic populations of C, O, F and S for deposits formed in cases where $TFSI^-$ is coordinated to the Mg^{2+} center (Figure A10).

A second effect relevant to achievement of high coulombic efficiencies for Mg electrodeposition/dissolution may relate to the elimination of trace water in the electrolyte. Many of the electrolyte systems that have been reported to support reversible Mg deposition/dissolution are ones with intrinsic chemical reactivity toward water. Such

reactivity should scavenge water from the electrolyte, preventing its delivery to the Mg interface and production of a passivating MgO layer. For example, two of the electrolyte systems that have shown good reversibility for Mg include Grignard systems and $Mg(BH_4)_2$, both of which are reactive toward water. We speculate that the achievement here of good coulombic efficiency and lack of surface blocking is likely aided by the consumption of trace water in the electrolyte by BH_4^-. It also seems likely that the $MPEG_7PyrTFSI$ ionic liquid has the best performance due to its higher concentration of free BH_4^-, which is likely to be more reactive toward water than BH_4^- bound to Mg^{2+}.

The third way in which the PEGylated ILs may improve Mg electrochemical performance is through the production of cationic speciation for Mg^{2+} and the favorable impact of this on transport. As discussed above, the Raman data for $Mg(BH_4)_2/MPEG_7PyrTFSI$ electrolytes are consistent with speciation of Mg^{2+} as $(PEG)Mg(BH_4)^+$. This cationic state will facilitate electromigration toward the Mg electrode under deposition conditions and away from it under dissolution conditions, which should favor high currents.

4.6 Conclusions

We have synthesized task specific ILs that bear pendent polyether chains designed to complex Mg^{2+} from a $Mg(BH_4)_2$ source. This complexation changes the speciation of Mg^{2+} in these media, which was characterized using Raman spectroscopy. Specifically, polyether complexation prevents $TFSI^-$ coordination at Mg^{2+} and also generates free BH_4^- for the $Mg(BH_4)_2/MPEG_7PyrTFSI$ IL. These speciation changes

produce superior electrochemical behavior compared to that in BMPyrTFSI or previously reported electrolyte systems containing ether or polyether solvents. These PEGylated IL electrolytes give Mg deposition/dissolution with high CE and very high current density. The Mg deposits are characterized by high purity (i.e. no detectable surface fouling) and lack of dendritic growth. These results represent the first demonstration of reversible electrochemical deposition/dissolution of Mg in an ionic liquid designed specifically for improved electrochemical performance.

We speculate on three specific possible origins of the improved electrochemical performance of these systems that derive from the observed speciation changes. These include suppression of reductive decomposition pathways for $TFSI^-$ that may cause low CE and/or surface fouling, decrease of trace water concentrations in the electrolyte that may react with Mg and produce passivating films of MgO, and the generation of cationic speciation for Mg^{2+} that enhances transport by electromigration. All of these possible mechanisms provide guidance for future efforts to improve Mg battery chemistries.

4.7 References:

1. Yoo, H. D. *et al.* Mg rechargeable batteries: an on-going challenge. *Energy Environ. Sci.* **6,** 2265–2279 (2013).

2. Mohtadi, R. & Mizuno, F. Magnesium batteries: Current state of the art, issues and future perspectives. *Beilstein J. Nanotechnol.* **5,** 1291–311 (2014).

3. Muldoon, J., Bucur, C. B. & Gregory, T. Quest for Nonaqueous Multivalent Secondary Batteries: Magnesium and Beyond. *Chem. Rev.* **114,** 11683–11720 (2014).

4. Park, M.-S., Kim, J.-G., Kim, Y.-J., Choi, N.-S. & Kim, J.-S. Recent Advances in Rechargeable Magnesium Battery Technology: A Review of the Field's Current Status and Prospects. *Isr. J. Chem.* **55,** 570–585 (2015).

5. Liu, T. *et al.* A fundamental study on the [(μ-Cl)3Mg2(THF)6](+) dimer electrolytes for rechargeable Mg batteries. *Chem. Commun. (Camb).* **51,** 2312–5 (2015).

6. Muldoon, J. *et al.* Electrolyte roadblocks to a magnesium rechargeable battery. *Energy Environ. Sci.* **5,** 5941–5950 (2012).

7. Muldoon, J. *et al.* Corrosion of magnesium electrolytes: chlorides – the culprit. *Energy Environ. Sci.* **6,** 482 (2013).

8. Lv, D. *et al.* A Scientific Study of Current Collectors for Mg Batteries in Mg(AlCl2EtBu)2/THF Electrolyte. *J. Electrochem. Soc.* **160,** A351–A355 (2012).

9. Yagi, S., Tanaka, a., Ichikawa, Y., Ichitsubo, T. & Matsubara, E. Electrochemical Stability of Magnesium Battery Current Collectors in a Grignard Reagent-Based Electrolyte. *J. Electrochem. Soc.* **160,** C83–C88 (2013).

10. Aurbach, D. *et al.* Electrolyte Solutions for Rechargeable Magnesium Batteries Based on Organomagnesium Chloroaluminate Complexes. *J. Electrochem. Soc.* **149,** A115 (2002).

11. Shao, Y. *et al.* Coordination chemistry in magnesium battery electrolytes: how ligands affect their performance. *Sci. Rep.* **3,** 3130 (2013).

12. Tuerxun, F. *et al.* High concentration magnesium borohydride/tetraglyme electrolyte for rechargeable magnesium batteries. *J. Power Sources* **276,** 255–261 (2015).

13. Mohtadi, R. Borohydride Solvo-Ionic Liquid Family For Magnesium Battery. **1,** 1–4 (2015).

14. Mohtadi, R., Matsui, M., Arthur, T. S. & Hwang, S.-J. Magnesium borohydride: from hydrogen storage to magnesium battery. *Angew. Chem. Int. Ed. Engl.* **51,** 9780–3 (2012).

15. Shterenberg, I., Salama, M., Gofer, Y., Levi, E. & Aurbach, D. The challenge of developing rechargeable magnesium batteries. *MRS Bull.* **39,** 453–460 (2014).

16. Rajput, N. N., Qu, X., Sa, N., Burrell, A. K. & Persson, K. a. The Coupling between Stability and Ion Pair Formation in Magnesium Electrolytes from First-Principles Quantum Mechanics and Classical Molecular Dynamics. *J. Am. Chem. Soc.* **137,** 3411–3420 (2015).

17. Shao, Y. *et al.* Nanocomposite polymer electrolyte for rechargeable magnesium batteries. *Nano Energy* **12,** 750–759 (2015).

18. Chang, J. *et al.* Synergetic Role of Li(+) during Mg Electrodeposition/Dissolution in Borohydride Diglyme Electrolyte Solution: Voltammetric Stripping Behaviors on a Pt Microelectrode Indicative of Mg-Li Alloying and Facilitated Dissolution. *ACS Appl. Mater. Interfaces* **7,** 2494–2502 (2015).

19. MacFarlane, D. R. *et al.* Energy applications of ionic liquids. *Energy Environ. Sci.* **7,** 232–250 (2014).

20. NuLi, Y., Yang, J., Wang, J., Xu, J. & Wang, P. Electrochemical Magnesium Deposition and Dissolution with High Efficiency in Ionic Liquid. *Electrochem. Solid-State Lett.* **8,** C166 (2005).

21. NuLi, Y., Yang, J. & Wang, P. Electrodeposition of magnesium film from BMIMBF4 ionic liquid. *Appl. Surf. Sci.* **252,** 8086–8090 (2006).

22. Zhao, Q., NuLi, Y., Nasiman, T., Yang, J. & Wang, J. Reversible Deposition and Dissolution of Magnesium from Imidazolium-Based Ionic Liquids. *Int. J. Electrochem.* **2012,** 1–8 (2012).

23. Lodovico, L., Martins, V. L., Benedetti, T. M. & Torresi, R. M. Electrochemical Behavior of Iron and Magnesium in Ionic Liquids. *J. Braz. Chem. Soc.* **25,** 460–468 (2014).

24. Vardar, G. *et al.* Electrochemistry of magnesium electrolytes in ionic liquids for secondary batteries. *ACS Appl. Mater. Interfaces* **6,** 18033–18039 (2014).

25. Giffin, G., Moretti, A., Jeong, S. & Passerini, S. Complex Nature of Ionic Coordination in Magnesium Ionic Liquid-Based Electrolytes: Solvates with Mobile Mg2+ Cations. *J. Phys. Chem. C* **118,** 9966–9973 (2014).

26. Watkins, T. & Buttry, D. A. Determination of Mg2+ Speciation in a TFSI−-Based Ionic Liquid With and Without Chelating Ethers Using Raman Spectroscopy. *J. Phys. Chem. B* **119,** 7003–7014 (2015).

27. Venkata Narayanan, N. S., Ashok Raj, B. V. & Sampath, S. Magnesium ion conducting, room temperature molten electrolytes. *Electrochem. commun.* **11,** 2027–2031 (2009).

28. Narayanan, N. S. V., Ashok Raj, B. V. & Sampath, S. Physicochemical, spectroscopic and electrochemical characterization of magnesium ion-conducting,

room temperature, ternary molten electrolytes. *J. Power Sources* **195,** 4356–4364 (2010).

29. Murase, K. *et al.* Enhanced Anodic Dissolution of Magnesium in Quaternary-Ammonium-Based Ionic Liquid Containing a Small Amount of Water. *J. Electrochem. Soc.* **160,** D453–D458 (2013).

30. Kar, M., Winther-Jensen, B., Forsyth, M. & MacFarlane, D. R. Chelating ionic liquids for reversible zinc electrochemistry. *Phys. Chem. Chem. Phys.* **15,** 7191–7 (2013).

31. Giffin, G. a., Tannert, J., Jeong, S., Uhl, W. & Passerini, S. Crystalline Complexes of Pyr 12O1 TFSI-Based Ionic Liquid Electrolytes. *J. Phys. Chem. C* **119,** 5878–5887 (2015).

32. Dobbelin, M. *et al.* Synthesis of Pyrrolidinium-Based Poly (ionic liquid) Electrolytes with Poly (ethylene glycol) Side Chains. *Chem. Mater.* **24,** 1583–1590 (2012).

33. Ganapatibhotla, L. V. N. R., Zheng, J., Roy, D. & Krishnan, S. PEGylated Imidazolium Ionic Liquid Electrolytes: Thermophysical and Electrochemical Properties. *Chem. Mater.* **22,** 6347–6360 (2010).

34. Marks, T. J., Kolb, J. R. & Introduction, I. Covalent Transition Metal, Lanthanide, and Actinide Tetrahydroborate Complexes. *Chem. Rev.* **77,** 263–293 (1976).

35. Shirk, a. E. & Shriver, D. F. Solvent and cation dependence of the tetrahydroborate, BH4-, Raman spectrum. *J. Am. Chem. Soc.* **95,** 5901–5904 (1973).

36. Marks, T. J., Kennelly, W. J., Kolb, J. R. & Shimp, L. a. Structure and dynamics in metal tetrahydroborates. II. Vibrational spectra and structures of some transition metal and actinide tetrahydroborates - NO COPY. *Inorg. Chem.* **11,** 2540–2546 (1972).

37. Davies, N., Bird, P. H. & Wallbridge, M. G. H. Spectroscopic Studies on Derivatives of Aluminium Borohydride. *J. Chem. Soc. A* 2269–2272 (1968).

38. Emery, A. R. & Taylor, R. C. Raman Spectroscopy in Liquid Ammonia Solutions. Vibrational Frequencies and Force Constants for Isotopic Species of the Borohydride Ion Having Tetrahedral Symmetry. *J. Chem. Phys* **3848,** 1953–1956 (1958).

39. Dalton, D. A., Somayazulu, M., Goncharov, A. F. & Hemley, R. J. Static compression of tetramethylammonium borohydride. *J. Phys. Chem. A* **115,** 11033–11038 (2011).

40. Brouillette, D. *et al.* Stable solvates in solution of lithium bis(trifluoromethylsulfone)imide in glymes and other aprotic solvents: Phase diagrams, crystallography and Raman spectroscopy. *Phys. Chem. Chem. Phys.* **4,** 6063–6071 (2002).

41. Monteiro, M. J., Bazito, F. F. C., Siqueira, L. J. a, Ribeiro, M. C. C. & Torresi, R. M. Transport coefficients, Raman spectroscopy, and computer simulation of lithium salt solutions in an ionic liquid. *J. Phys. Chem. B* **112,** 2102–2109 (2008).

42. Lassègues, J.-C., Grondin, J. & Talaga, D. Lithium solvation in bis(trifluoromethanesulfonyl)imide-based ionic liquids. *Phys. Chem. Chem. Phys.* **8,** 5629–32 (2006).

43. Lassègues, J., Grondin, J., Aupetit, C. & Johansson, P. Spectroscopic Identification of the Lithium Ion Transporting Species in LiTFSI-Doped Ionic Liquids. *J. Phys. Chem. A.* **113,** 305–314 (2009).

44. Duluard, S. *et al.* Lithium solvation and diffusion in the bis(trifluoromethanesulfonyl)imide ionic liquid. *J. Raman Spectrosc.* **39,** 627–632 (2008).

45. Umebayashi, Y. *et al.* Lithium ion solvation in room-temperature ionic liquids involving bis(trifluoromethanesulfonyl) imide anion studied by Raman spectroscopy and DFT calculations. *J. Phys. Chem. B* **111,** 13028–32 (2007).

46. Castriota, M. *et al.* Raman Investigation of the Ionic Liquid N-Methyl-N-propylpyrrolidinium Bis(trifluoromethanesulfonyl)imide and Its Mixture with LiN(SO2CF3)2. *J. Phys. Chem. A* **109,** 92–96 (2005).

47. Hardwick, L. J., Holzapfel, M., Wokaun, A. & Petr, N. Raman study of lithium coordination in EMI-TFSI additive systems as lithium-ion battery ionic liquid electrolytes. *J. Raman Spectrosc.* **38,** 110–112 (2007).

48. Borodin, O., Smith, G. D. & Henderson, W. Li+ Cation Environment, Transport, and Mechanical Properties of the LiTFSI Doped N-Methyl-N-alkylpyrrolidinium+TFSI- Ionic Liquids. *J. Phys. Chem. B.* **110,** 16879–16886 (2006).

49. Herstedt, M. *et al.* Spectroscopic characterization of the conformational states of the bis(trifluoromethanesulfonyl)imide anion (TFSI−). *J. Raman Spectrosc.* **36,** 762–770 (2005).

50. Tutusaus, O. *et al.* An Efficient Halogen-Free Electrolyte for Use in Rechargeable Magnesium Batteries. *Angew. Chem. Int. Ed. Engl.* 1–6 (2015). doi:10.1002/anie.201412202

51. Ha, S. *et al.* Magnesium(II) Bis(trifluoromethane sulfonyl) Imide-Based Electrolytes with Wide Electrochemical Windows for Rechargeable Magnesium Batteries. *Appl. Mater. Interfaces* **6,** 4063–4073 (2014).

52. Kitada, A., Kang, Y., Uchimoto, Y. & Murase, K. Room-Temperature Electrodeposition of Mg Metal from Amide Salts Dissolved in Glyme-Ionic Liquid Mixture. *J. Electrochem. Soc.* **161,** D102–D106 (2014).

53. Fukutsuka, T. *et al.* New Magnesium-ion Conductive Electrolyte Solution Based on Triglyme for Reversible Magnesium Metal Deposition and Dissolution at Ambient Temperature. *Chem. Lett.* **43,** 1788–1790 (2014).

CHAPTER 5

EVALUATION OF ION PAIRING FOR SOLUTIONS OF $Mg(TFSI)_2$ AND $Mg(BH_4)_2$ IN PEGYLATED IONIC LIQUIDS

5.1 Introduction

As described in chapter 4, PEGylated ILs clearly create an environment far more suitable to Mg electrochemistry than do more conventional IL systems, when dissolving $Mg(BH_4)_2$. Furthermore, not only is $Mg(BH_4)_2$ a better electrolyte for Mg electrodeposition in the PEG-ILs, with respect to BMPyrTFSI, but it appears to be outperform the previously reported $Mg(BH_4)_2$/glyme (without $LiBH_4$) electrolytes as well.

Raman spectroscopy revealed that in the PEG-IL systems a new peak in the B-H stretching region of the spectra could be observed. This peak, at 2256 cm^{-1}, was attributed to freely dissociated BH_4^- anions, as opposed to anions in contact ion pairs with Mg^{2+}. From comparisons of the CVs in chapter 4, it appears there is a link between higher degree of BH_4^- dissociation and improved electrochemical performance. This chapter briefly describes work in progress evaluating in greater detail the ion pairing of Mg^{2+} with $TFSI^-$ and/or BH_4^- anions in the various PEG-IL systems.

5.2 Results and Discussion

Figure 36 shows the fraction of $TFSI^-$ anions in coordination with Mg^{2+} as the $Mg(TFSI)_2$ mole fraction (x in $[Mg(TFSI)_2]_x[IL]_{1-x}$) is varied in ILs with different PEG chain lengths, as well as the BMPyrTFSI IL. It is very apparent from the plot that clear distinctions can be made between the ILs based on the number of ether oxygens in the

pendent PEG chain. Giffin *et al.* recently reported a crystal structure for $[Mg(TFSI)_2]_{0.5}[MPEG_1PyrTFSI]_{0.5}$ and showed that the closest ether oxygen (the only ether oxygen) did not coordinate with Mg^{2+}.[1] Liquid phase Raman spectra support Giffin's finding (note the equivalent trend for $TFSI^-$ coordination in BMPyrTFSI and $MPEG_1PyrTFSI$ shown in figure 36). Thus, assuming the closest ether oxygen cannot coordinate Mg^{2+}, the maximum PEG-IL/Mg ratios needed to achieve a 6/1 ether-oxygen/Mg^{2+} ratio are 1/1, 2/1, 3/1, and 6/1 for the PEG7-IL, PEG4-IL, PEG3-IL, and PEG2-IL, respectively. Arrows indicating these compositions are shown in the figure. Interestingly, for the PEG_7-IL no $TFSI^-$ is coordinated to Mg^{2+} when $x \leq 0.5$. This is

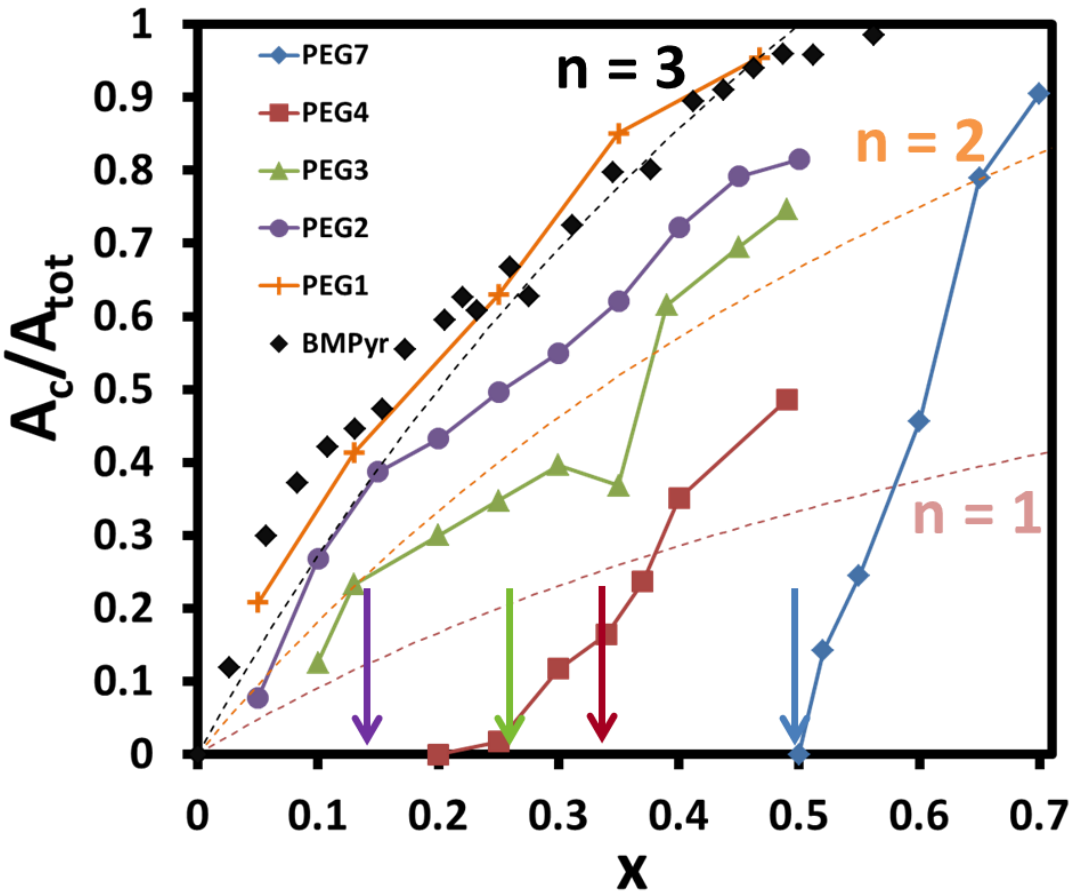

Figure 36: Fraction of $TFSI^-$ coordinated to Mg^{2+} as a function of the mole fraction of $Mg(TFSI)_2$ in $MPEG_7PyrTFSI$ (blue diamonds), $MPEG_4PyrTFSI$ (red squares), $MPEG_3PyrTFSI$ (green triangles), $MPEG_2PyrTFSI$ (purple circles), and MPEG1PyrTFSI (orange crosses). Arrows indicate the compositions at which the ratio ether-oxygen/Mg^{2+} is 6/1. Lines simply connect data points to guide the reader's eye.

consistent with the notion that the PEG_7-IL makes available 6 ether oxygens for coordination to Mg^{2+}, the ether oxygen closest to the parent cation being unavailable due to coulombic repulsion between Mg^{2+} and the charge center of the IL cation. However, for lower order PEG chains the composition at which all $TFSI^-$ are free does not fall directly on the ratios mentioned above. Instead, more than the 6/1 ether oxygen ratio is required to free all $TFSI^-$ from the solvation shell of all Mg^{2+}. This can be rationalized by

considering the fact that for systems with PEG chains containing less than 7 ether oxygens multiple IL cations need to coordinate Mg^{2+} in order to achieve the 6/1 coordinating condition. Such a coordination geometry is likely hindered by coulombic repulsions of multiple positive charge centers. Data to date does, in fact, suggest that full displacement of $TFSI^-$ becomes more difficult as the PEG chains are shortened.

For the case of $Mg(BH_4)_2$ electrolytes, $TFSI^-$ coordination is shown in Figure 37. This is the same plot as Figure 29 in chapter 4 but with the PEG_2-IL added. It is clear from this plot that while the PEG2 chain removes more $TFSI^-$ from the Mg^{2+} solvation shell than does BMPyrTFSI, at equivalent concentrations, it is does not have the same chelation strength as the higher order PEG chains. This result might be explained by the more flexible nature of the longer chelating chains.

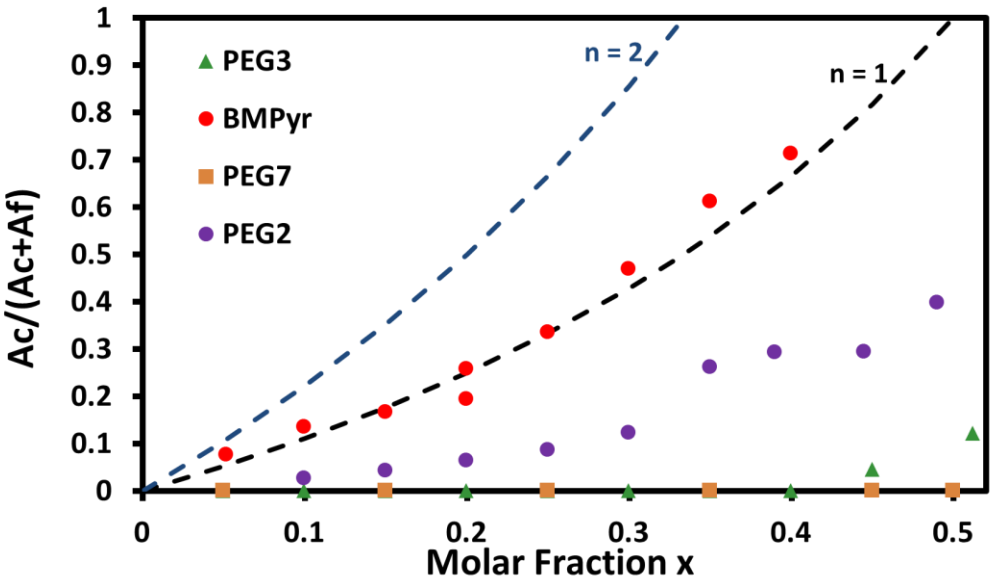

Figure 37: Fraction of $TFSI^-$ coordinated to Mg^{2+} as a function of the mole fraction of $Mg(BH_4)_2$ in $MPEG_7PyrTFSI$ (orange squares), $MPEG_3PyrTFSI$ (green triangles), $MPEG_2PyrTFSI$ (purple circles), and BMPyrTFSI (red circles).

Finally, in chapter 4, Figure 26 showed a distinct Raman band at 2256 cm^{-1} attributed to freely dissociated BH_4^-. It was clear from Figure 26 that the PEG_7-IL dissociated a significantly greater fraction of BH_4^-, at the same concentrations, as the PEG_3-IL. Figure 38 shows the fraction of dissociated BH_4^- anions quantified for $Mg(BH_4)_2$ in the series of PEG-ILs. For the PEG7-IL, the data appears to trend toward 0.45–0.50 for an infinitely dilute solution. This trend seems reasonable as it would suggest that, at most, only one BH_4^- can dissociate from a given Mg^{2+} cation, creating $[MgBH_4]^+$ complexes. A second dissociation becomes exceedingly difficult, energetically, so it is not surprising that $[MgBH_4]^+$ appears to be the limiting case. It also further supports the idea that $[MgBH_4]^+$ might be the electrochemically active species capable of reversible electrodeposition, as opposed to simply being Mg^{2+}.

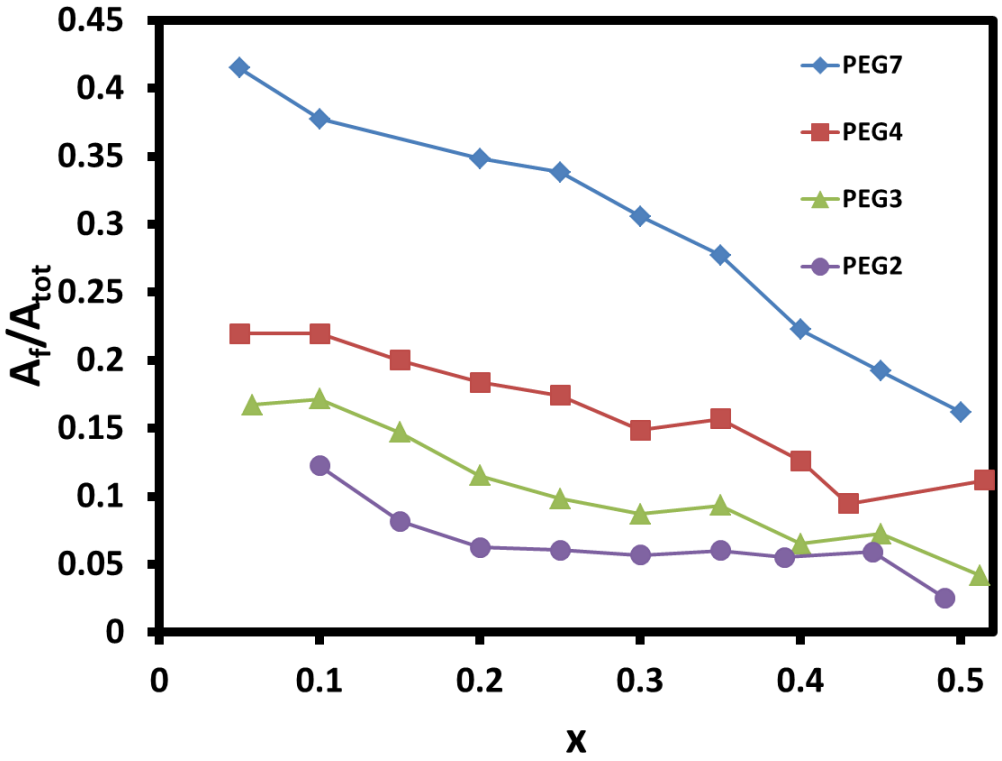

Figure 38: Fraction of BH_4^- in a freely dissociated state as a function of the molar fraction of $Mg(BH_4)_2$ in $MPEG_7PyrTFSI$ (blue squares), $MPEG_4PyrTFSI$ (red squares), $MPEG_3PyrTFSI$ (green triangles), and $MPEG_2PyrTFSI$ (purple circles). Lines connect data points to guide the

5.3 Conclusions

It is stressed that the work presented in this chapter is not final. Future plans are in place to evaluate the solvating power of the PEG-ILs as a function of PEG chain via molecular dynamics simulations. Work is also planned for equivalent assessments to those above for different parent IL cations, such as phosphonium, imidazolium and ammonium.

5.4 References

1. Giffin, G. a., Tannert, J., Jeong, S., Uhl, W. & Passerini, S. Crystalline Complexes of Pyr 12O1 TFSI-Based Ionic Liquid Electrolytes. *J. Phys. Chem. C* **119,** 5878–5887 (2015).

CHAPTER 6

CONCLUDING REMARKS

When I began working on this project, I could not have imagined just how challenging it would prove to be. My primary goal was to achieve reversible Mg electrodeposition in a pure ionic liquid. As a naïve, young graduate student, without a background in the field, I had no idea that many had essentially written ionic liquids off as a viable medium for Mg battery electrolytes. They certainly had good reasons for this, and—to be fair—perhaps still do. The point is, without that original ignorance, I may never have felt that this research was worth pursuing. As I began to immerse myself in the literature, what started as a "guiding" ignorance would soon turn into a stubborn obsession with "finding a way." I thought that with a deeper understanding of the failure mechansisms occurring within Mg/IL solutions, one could conceive of an arrangement that might overcome the obstacles usually in place. With the results from the $Mg(BH_4)_2$/$MPEG_m$PyrTFSI electrolytes, it is clear that at least some of those obstacles have been hurdled, as chemically reversible Mg electrodeposition was clearly demonstrated in an ionic liquid. Figure 39 shows how cyclic voltammetry of 0.5 M $Mg(BH_4)_2$/$MPEG_7$PyrTFSI compares to some of the more promising electrolytes in the field. Each of the CVs in figure 39 were acquired under similar environmental conditions, however, it may be the case that electrolytes were not synthesized with the same care as in their respective literature sources, which may account for minor discrepancies.

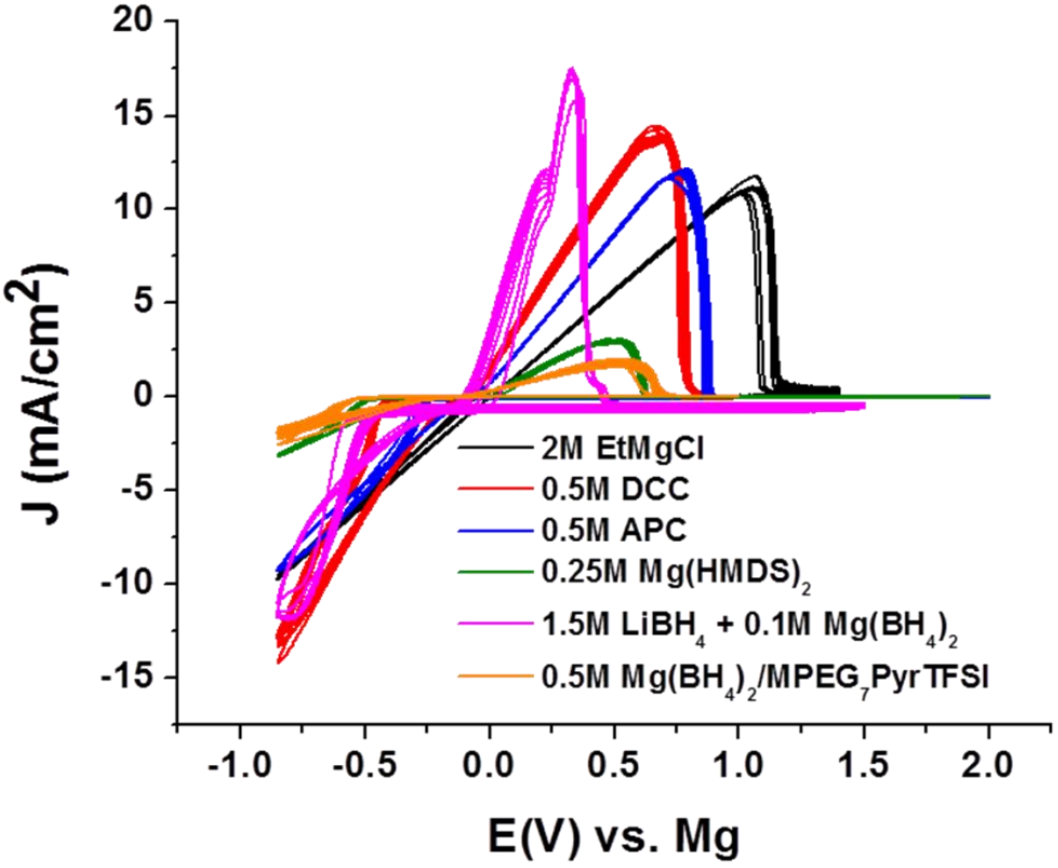

Figure 39: Cyclic voltammetric comparison of notable Mg electrolytes, including **0.5 M $Mg(BH_4)_2$/$MPEG_7$PyrTFSI**. Mg(HMDS) is an electrolyte of magnesium bis(hexamethyldisilazide) with $AlCl_3$ at a 1:2 ratio.

As encouraging as the $Mg(BH_4)_2$/$MPEG_m$PyrTFSI electrolytes are, it is unlikely that the specific systems reported on here will find use outside of the laboratory. However, this should really only be the beginning for PEG-ILs with Mg electrolytes. It is my hope that the work demonstrated in chapter 4, and extended in chapter 5, will open a new direction of exploration for the science of Mg batteries. For instance, $Mg(BH_4)_2$ was shown to be a useful Mg source in this work, but there is no reason to believe more

suitable Mg sources might not also be able to take advantage of the unique coordinating conditions. Other Mg complexes in PEG-ILs, like those mentioned in the introduction, might produce electrolytes with more appropriate metrics for building a commercial device. Furthermore, the $MPEG_mPyrTFSI$ ILs may not be the most ideal PEG-ILs to use. After all, discussions in chapters 2 and 4 pointed out that $TFSI^-$ does not appear to be a good anion for use in Mg electrolyte systems. Thus, a search for alternative anions should be conducted. Alternative parent cations should be tested as well.

Finally, the study of these Mg/PEG-IL systems should be accompanied by theoretical investigations aimed at revealing the underlying principles governing their electrochemical behavior. Future experimental screening of prospective systems can be first carried out with cyclic voltammetry, as was done in chapter 4. When a system has shown that reversible electrodeposition of Mg is possible, efforts should be taken to evaluate the mechanisms of deposition and dissolution with in-situ techniques such as EQCM, STEM, EIS, and spectroelectrochemistry. It is hypothesized here, based on the evidence from chapter 4 and findings from other Mg electrolytes, that electrodeposition of Mg requires electroactive Mg complexes in which Mg is in contact with stable anions—like BH_4^- or Cl^-—that act as protective "shields" from electrolyte components that would otherwise decompose in the presence of the reduced Mg (Mg^0 or short lived Mg^+). The appropriate set of in-situ experiments should be used to confirm or reject this.

References

Chapter 1

1. Bureau, U. S. C. U.S. and World Population Clock. 1 (2015). at <http://www.census.gov/popclock/>

2. Agency, I. E. *Key World Energy Statistics*. (2015).

3. NOAA. CO2 Now.org. 1 (2015). at <http://co2now.org/>

4. Pidwirny, M. Solar Radiation. *Encycl. Earth* 1 (2012). at <http://www.eoearth.org/view/article/156098/>

5. Budikova, D. Albedo The Encyclopedia of Earth. *Encycl. Earth* 1 (2013). at <http://www.eoearth.org/view/article/149954/>

6. Gröger, O., Gasteiger, H. a. & Suchsland, J.-P. Review—Electromobility: Batteries or Fuel Cells? *J. Electrochem. Soc.* **162,** A2605–A2622 (2015).

7. Scrosati, B., Hassoun, J. & Schalkwijk, W. A. Van. *Lithium Batteries: Advanced Technologies and Applications*. (John Wiley & Sons, 2013).

8. Aurbach, D., Zinigrad, E., Cohen, Y. & Teller, H. A short review of failure mechanisms of lithium metal and lithiated graphite anodes in liquid electrolyte solutions. *Solid State Ionics* **148,** 405–416 (2002).

9. Moore, G. E. Cramming more components onto integrated circuits. *Proc. IEEE* **86,** 82–85 (1998).

10. Zu, C.-X. & Li, H. Thermodynamic analysis on energy densities of batteries. *Energy Environ. Sci.* **4,** 2614 (2011).

11. Mizushima, K., Jones, P. C., Wiseman, P. J. & Goodenough, J. B. LixCoO2 (0<x<-1): A new cathode material for batteries of high energy density. *Mater. Res. Bull.* **15,** 783–789 (1980).

12. Muldoon, J., Bucur, C. B. & Gregory, T. Quest for Nonaqueous Multivalent Secondary Batteries: Magnesium and Beyond. *Chem. Rev.* **114,** 11683–11720 (2014).

13. Gao, X.-P. & Yang, H.-X. Multi-electron reaction materials for high energy density batteries. *Energy Environ. Sci.* **3,** 174 (2010).

14. Petersen, U. Mining the hydrosphere. *Geochim. Cosmochim. Acta* **58,** 2387–2403 (1994).

15. CRC. *Handbook of Chemistry Physics*. (2015).

16. Huie, M. M., Bock, D. C., Takeuchi, E. S., Marschilok, A. C. & Takeuchi, K. J. Cathode materials for magnesium and magnesium-ion based batteries. *Coord. Chem. Rev.* **287,** 15–27 (2015).

17. Yoo, H. D. *et al.* Mg rechargeable batteries: an on-going challenge. *Energy Environ. Sci.* **6,** 2265–2279 (2013).

18. Peled, E. & Straze, H. The Kinetics of the Magnesium Electrode in Thionyl Chloride Solutions. **834,** 1030–1035 (1977).

19. Lu, Z., Schechter, A., Moshkovich, M. & Aurbach, D. On the electrochemical behavior of magnesium electrodes in polar aprotic electrolyte solutions. *J. Electroanal. Chem.* **466,** 203–217 (1999).

20. Lossius, L. P. & Emmenegger, F. Plating Of Magnesium From Organic Solvents. *Electrochem. Acta* **41,** 445–447 (1996).

21. Bucur, C. B., Gregory, T., Oliver, A. G. & Muldoon, J. Confession of a Magnesium Battery. *J. Phys. Chem. Lett.* 3578–3591 (2015). doi:10.1021/acs.jpclett.5b01219

22. Mohtadi, R. & Mizuno, F. Magnesium batteries: Current state of the art, issues and future perspectives. *Beilstein J. Nanotechnol.* **5,** 1291–311 (2014).

23. Muldoon, J. *et al.* Electrolyte roadblocks to a magnesium rechargeable battery. *Energy Environ. Sci.* **5,** 5941–5950 (2012).

24. Park, M.-S., Kim, J.-G., Kim, Y.-J., Choi, N.-S. & Kim, J.-S. Recent Advances in Rechargeable Magnesium Battery Technology: A Review of the Field's Current Status and Prospects. *Isr. J. Chem.* **55,** 570–585 (2015).

25. Linn, C. B.; Noller, C. R. The Catalyzed Reaction of Ethylmagnesium Bromide with Ethyl Bromide. **58,** 816–819 (1926).

26. Gaddum, L. W. & French, H. E. The Electrolysis of Grignard Solutions. *J. Am. Chem. Soc.* **49,** 1295–1299 (1927).

27. Overcash, D. M. & Mathers, F. C. The Electrodeposition of Magnesium. *ECS Trans.* **64,** 305–311 (1933).

28. Evans, W. V.; Lee, F. H.; Lee, C. H. The Decomposition Voltage of Grignard Reagents in Ether Solution. *J. Am. Chem. Soc.* **57,** 489–491 (1935).

29. Connor, J. H., Reid, W. E. & Wood, G. B. Electrodeposition of Metals from Organic Solutions. *J. Electrochem. Soc.* **104,** 38 (1957).

30. Gregory, T. D., Hoffman, R. J. & Winterton, R. C. Nonaqueous Electrochemistry of Magnesium Applications to Energy Storage. *J. Electrochem. Soc.* **137,** 775–780 (1990).

31. Aurbach, D. *et al.* Prototype systems for rechargeable magnesium batteries. *Nature* **407,** 724–7 (2000).

32. Aurbach, D., Moshkovich, M., Schechter, A. & Turgeman, R. Magnesium Deposition and Dissolution Processes in Ethereal Grignard Salt Solutions Using Simultaneous EQCM-EIS and In Situ FTIR Spectroscopy. *Electrochem. Solid-State Lett.* **3,** 31–34 (2000).

33. Liebenow, C., Yang, Z., Lobitz, P., Moritz, E. & Uni, A. The electrodeposition of magnesium using solutions of organomagnesium halides , amidomagnesium halides and magnesium organoborates. 1–5 (2000).

34. Aurbach, D., Schechter, A., Moshkovich, M. & Cohen, Y. On the Mechanisms of Reversible Magnesium Deposition Processes. *J. Electrochem. Soc.* **148,** A1004 (2001).

35. Aurbach, D. *et al.* Electrolyte Solutions for Rechargeable Magnesium Batteries Based on Organomagnesium Chloroaluminate Complexes. *J. Electrochem. Soc.* **149,** A115 (2002).

36. Aurbach, D., Turgeman, R., Chusid, O. & Gofer, Y. Spectroelectrochemical studies of magnesium deposition by in situ FTIR spectroscopy. *Electrochem. commun.* **3,** 252–261 (2001).

37. Aurbach, D., Cohen, Y. & Moshkovich, M. The Study of Reversible Magnesium Deposition by In Situ Scanning Tunneling Microscopy. *Electrochem. Solid-State Lett.* **4,** A113 (2001).

38. Mohtadi, R., Matsui, M., Arthur, T. S. & Hwang, S.-J. Magnesium borohydride: from hydrogen storage to magnesium battery. *Angew. Chem. Int. Ed. Engl.* **51,** 9780–3 (2012).

39. Guo, Y. *et al.* Boron-based electrolyte solutions with wide electrochemical windows for rechargeable magnesium batteries. *Energy Environ. Sci.* **5,** 9100 (2012).

40. Tutusaus, O. *et al.* An Efficient Halogen-Free Electrolyte for Use in Rechargeable Magnesium Batteries. *Angew. Chem. Int. Ed. Engl.* 1–6 (2015). doi:10.1002/anie.201412202

41. Carter, T. J. *et al.* Boron clusters as highly stable magnesium-battery electrolytes. *Angew. Chem. Int. Ed. Engl.* **53,** 3173–7 (2014).

42. Aurbach, D. *et al.* Progress in Rechargeable Magnesium Battery Technology. *Adv. Mater.* **19,** 4260–4267 (2007).

43. Wang, F., Guo, Y., Yang, J., Nuli, Y. & Hirano, S. A novel electrolyte system without a Grignard reagent for rechargeable magnesium batteries. *Chem. Commun. (Camb).* **48,** 10763–5 (2012).

44. Bian, P., NuLi, Y., Abudoureyimu, Z., Yang, J. & Wang, J. A novel thiolate-based electrolyte system for rechargeable magnesium batteries. *Electrochim. Acta* **121,** 258–263 (2014).

45. Doe, R. E. *et al.* Novel, electrolyte solutions comprising fully inorganic salts with high anodic stability for rechargeable magnesium batteries. *Chem. Commun. (Camb).* **50,** 243–5 (2014).

46. Shterenberg, I. *et al.* Evaluation of $(CF_3SO_2)_2N^-$ (TFSI) Based Electrolyte Solutions for Mg Batteries. *J. Electrochem. Soc.* **162,** A7118–A7128 (2015).

47. Muldoon, J. *et al.* Corrosion of magnesium electrolytes: chlorides – the culprit. *Energy Environ. Sci.* **6,** 482 (2013).

48. Kitada, A. *et al.* Room Temperature Magnesium Electrodeposition from Glyme-Coordinated Ammonium Amide Electrolytes. *J. Electrochem. Soc.* **162,** D389–D396 (2015).

49. Ha, S. *et al.* Magnesium(II) Bis(trifluoromethane sulfonyl) Imide-Based Electrolytes with Wide Electrochemical Windows for Rechargeable Magnesium Batteries. *Appl. Mater. Interfaces* **6,** 4063–4073 (2014).

50. Kitada, A., Kang, Y., Uchimoto, Y. & Murase, K. Room-Temperature Electrodeposition of Mg Metal from Amide Salts Dissolved in Glyme-Ionic Liquid Mixture. *J. Electrochem. Soc.* **161,** D102–D106 (2014).

51. Fukutsuka, T. *et al.* New Magnesium-ion Conductive Electrolyte Solution Based on Triglyme for Reversible Magnesium Metal Deposition and Dissolution at Ambient Temperature. *Chem. Lett.* **43,** 1788–1790 (2014).

52. Shao, Y. *et al.* Coordination chemistry in magnesium battery electrolytes: how ligands affect their performance. *Sci. Rep.* **3,** 3130 (2013).

53. Chang, J. *et al.* Synergetic Role of Li(+) during Mg Electrodeposition/Dissolution in Borohydride Diglyme Electrolyte Solution: Voltammetric Stripping Behaviors on a Pt Microelectrode Indicative of Mg-Li Alloying and Facilitated Dissolution. *ACS Appl. Mater. Interfaces* **7,** 2494–2502 (2015).

54. Mohtadi, R. Borohydride Solvo-Ionic Liquid Family For Magnesium Battery. **1,** 1–4 (2015).

55. Su, S. *et al.* A novel rechargeable battery with a magnesium anode, a titanium dioxide cathode, and a magnesium borohydride/tetraglyme electrolyte. *Chem. Commun.* **51,** 2641–2644 (2015).

56. Tuerxun, F. *et al.* High concentration magnesium borohydride/tetraglyme electrolyte for rechargeable magnesium batteries. *J. Power Sources* **276,** 255–261 (2015).

57. Shao, Y. *et al.* Nanocomposite polymer electrolyte for rechargeable magnesium batteries. *Nano Energy* **12,** 750–759 (2015).

58. Welton, T. Room-Temperature Ionic Liquids. Solvents for Synthesis and Catalysis - Chemical Reviews (ACS Publications). *Chem. Rev.* (1999). doi:10.1021/cr1003248

59. Welton, T. & Wasserscheid, P. *Ionic Liquids in Synthesis*. (Wiley-VCH Verlag GmbH & Co., 2002).

60. Handy, S. H. Room temperature ionic liquids: different classes and physical properties. *Curr. Org. Chem.* **9,** 959–988 (2005).

61. Endres, F. & Zein El Abedin, S. Air and water stable ionic liquids in physical chemistry. *Phys. Chem. Chem. Phys.* **8,** 2101–2116 (2006).

62. Zhang, S., Sun, N., He, X., Lu, X. & Zhang, X. Physical Properties of Ionic Liquids: Database and Evaluation. *J. Phys. Chem. Ref. Data* **35,** 1475 (2006).

63. Stark, A. & Seddon, K. R. Ionic Liquids. *Kirk-Othmer Encycl. Chem. Technol.* **26,** 836–920 (2007).

64. Tsuda, T. & Hussey, C. L. Electrochemistry of Room-Temperature Ionic Liquids and Melts. *Mod. Asp. Electrochem.* **45,** 63–174 (2009).

65. Armand, M., Endres, F., MacFarlane, D. R., Ohno, H. & Scrosati, B. Ionic-liquid materials for the electrochemical challenges of the future. *Nat. Mater.* **8,** 621–9 (2009).

66. Endres, F. Physical chemistry of ionic liquids. *Phys. Chem. Chem. Phys.* **12,** 1648 (2010).

67. Angell, A. C., Ansari, Y. & Zhao, Z. Ionic Liquids: Past, present and future. *Faraday Discuss.* **154,** 9–27 (2012).

68. Fedorov, M. V & Kornyshev, A. A. Ionic liquids at electrified interfaces. *Chem. Rev.* **114,** 2978–3036 (2014).

69. MacFarlane, D. R. *et al.* Energy applications of ionic liquids. *Energy Environ. Sci.* **7,** 232–250 (2014).

70. Narayanan, N. S. V., Ashok Raj, B. V. & Sampath, S. Physicochemical, spectroscopic and electrochemical characterization of magnesium ion-conducting, room temperature, ternary molten electrolytes. *J. Power Sources* **195,** 4356–4364 (2010).

71. Venkata Narayanan, N. S., Ashok Raj, B. V. & Sampath, S. Magnesium ion conducting, room temperature molten electrolytes. *Electrochem. commun.* **11,** 2027–2031 (2009).

72. 'Aluminum.' Chemicool Periodic Table. 1 (2015). at <http://www.chemicool.com/elements/aluminum.html>

73. 'Carbon.' Chemicool Periodic Table. 1 (2015). at <http://www.chemicool.com/elements/carbon.html>

74. 'Magnesium.' Chemicool Periodic Table. 1 (2015). at <http://www.chemicool.com/elements/magnesium.html>

75. 'Lithium.' Chemicool Periodic Table. 1 (2015). at <http://www.chemicool.com/elements/lithium.html>

76. 'Zinc.' Chemicool Periodic Table. 1 (2015). at <http://www.chemicool.com/elements/zinc.html>

77. ‘Calcium.’ Chemicool Periodic Table. 1 (2015). at <http://www.chemicool.com/elements/calcium.html>

Chapter 2

1. Kisza, A., Kaźmierczak, J., Børresen, B., Haarberg, G. M. & Tunold, R. Kinetics and mechanism of the magnesium electrode reaction in molten magnesium chloride. *J. Appl. Electrochem.* **25,** 940–946 (1995).

2. Kisza, A., Kazmierczak, J., Borresen, B., Haarberg, G. M. & Tunold, R. Kinetics and Mechanism of the Magnesium Electrode Reaction in Molten MgCl2-NaCl Binary Mixtures. *J. Electrochem. Soc.* **144,** 1646 (1997).

3. Borresen, B., Haarberg, G. M. & Tunold, R. Electrodeposition of magnesium from halide melts-charge transfer and diffusion kinetics. *Electrochem. Acta* **42,** 1613–1622 (1997).

4. Martínez, a. M., Børresen, B., Haarberg, G. M., Castrillejo, Y. & Tunold, R. Electrodeposition of magnesium from the eutectic LiCl-KCl melt. *J. Appl. Electrochem.* **34,** 1271–1278 (2004).

5. Balasubrahmanyam, K. Raman Spectra of Liquid MgCl2 and Liquid MgCl2[Single Bond]KCl System. *J. Chem. Phys.* **44,** 3270 (1966).

6. Maroni, V. A., Hathaway, E. J. & Cairns, E. J. Structural Studies of Magnesium Halide-Potassium Halide Melts by Raman Spectroscopy. *J. Phys. Chem.* **75,** 155–159 (1969).

7. Capwell, R. J. Raman spectra of crystalline and molten MgCl2. *Chem. Phys. Lett.* **12,** 443–446 (1972).

8. NuLi, Y., Yang, J., Wang, J., Xu, J. & Wang, P. Electrochemical Magnesium Deposition and Dissolution with High Efficiency in Ionic Liquid. *Electrochem. Solid-State Lett.* **8,** C166 (2005).

9. NuLi, Y., Yang, J. & Wang, P. Electrodeposition of magnesium film from BMIMBF4 ionic liquid. *Appl. Surf. Sci.* **252,** 8086–8090 (2006).

10. Wang, P., NuLi, Y., Yang, J. & Feng, Z. Mixed ionic liquids as electrolyte for reversible deposition and dissolution of magnesium. *Surf. Coatings Technol.* **201,** 3783–3787 (2006).

11. Cheek, G. T., O'Grady, W. E., El Abedin, S. Z., Moustafa, E. M. & Endres, F. Studies on the Electrodeposition of Magnesium in Ionic Liquids. *J. Electrochem. Soc.* **155,** D91–95 (2008).

12. Murase, K. *et al.* Enhanced Anodic Dissolution of Magnesium in Quaternary-Ammonium-Based Ionic Liquid Containing a Small Amount of Water. *J. Electrochem. Soc.* **160,** D453–D458 (2013).

13. Amir, N., Vestfrid, Y., Chusid, O., Gofer, Y. & Aurbach, D. Progress in nonaqueous magnesium electrochemistry. *J. Power Sources* **174,** 1234–1240 (2007).

14. Shimamura, O., Yoshimoto, N., Matsumoto, M., Egashia, M. & Morita, M. Electrochemical co-deposition of magnesium with lithium from quaternary ammonium-based ionic liquid. *J. Power Sources* **196,** 1586–1588 (2011).

15. Vardar, G. *et al.* Electrochemistry of Magnesium Electrolytes in Ionic Liquids for Secondary Batteries. (2014).

16. Howlett, P. C., Izgorodina, E. I., Forsyth, M. & Macfarlane, D. R. Electrochemistry at Negative Potentials in Bis(trifluoromethansulfonyl)amide Ionic Liquids. *Zeitschrift fur Phys. chemie.* **220,** 1483–1498 (2006).

17. Zhao, Q., NuLi, Y., Nasiman, T., Yang, J. & Wang, J. Reversible Deposition and Dissolution of Magnesium from Imidazolium-Based Ionic Liquids. *Int. J. Electrochem.* **2012,** 1–8 (2012).

18. Galiński, M., Lewandowski, A. & Stępniak, I. Ionic liquids as electrolytes. *Electrochim. Acta* **51,** 5567–5580 (2006).

19. Lu, Z., Schechter, A., Moshkovich, M. & Aurbach, D. On the electrochemical behavior of magnesium electrodes in polar aprotic electrolyte solutions. *J. Electroanal. Chem.* **466,** 203–217 (1999).

20. Peled, E. & Straze, H. The Kinetics of the Magnesium Electrode in Thionyl Chloride Solutions. **834,** 1030–1035 (1977).

21. Appetecchi, G. B., Scaccia, S., Tizzani, C., Alessandrini, F. & Passerini, S. Synthesis of Hydrophobic Ionic Liquids for Electrochemical Applications. *J. Electrochem. Soc.* **153,** A1685–A1691 (2006).

22. Bard, A. J., Faulkner, L. R., Swain, E. & Robey, C. *Electrochemical Methods: Fundamentals and Applications*. (2001).

23. Rajput, N. N., Qu, X., Sa, N., Burrell, A. K. & Persson, K. a. The Coupling between Stability and Ion Pair Formation in Magnesium Electrolytes from First-Principles Quantum Mechanics and Classical Molecular Dynamics. *J. Am. Chem. Soc.* **137,** 3411–3420 (2015).

24. Su, Y.-Z., Fu, Y.-C., Wei, Y.-M., Yan, J.-W. & Mao, B.-W. The electrode/ionic liquid interface: electric double layer and metal electrodeposition. *Chemphyschem* **11,** 2764–78 (2010).

25. Zhang, C. *et al.* Chelate Effects in Glyme/Lithium Bis(trifluoromethanesulfonyl)amide Solvate Ionic Liquids. I. Stability of Solvate Cations and Correlation with Electrolyte Properties. *J. Phy* **118,** 5144–5153 (2014).

26. Kitada, A. *et al.* Room Temperature Magnesium Electrodeposition from Glyme-Coordinated Ammonium Amide Electrolytes. *J. Electrochem. Soc.* **162,** D389–D396 (2015).

27. Kitada, A., Kang, Y., Uchimoto, Y. & Murase, K. Room-Temperature Electrodeposition of Mg Metal from Amide Salts Dissolved in Glyme-Ionic Liquid Mixture. *J. Electrochem. Soc.* **161,** D102–D106 (2014).

28. Fukutsuka, T. *et al.* New Magnesium-ion Conductive Electrolyte Solution Based on Triglyme for Reversible Magnesium Metal Deposition and Dissolution at Ambient Temperature. *Chem. Lett.* **43,** 1788–1790 (2014).

29. Ha, S. *et al.* Magnesium(II) Bis(trifluoromethane sulfonyl) Imide-Based Electrolytes with Wide Electrochemical Windows for Rechargeable Magnesium Batteries. *Appl. Mater. Interfaces* **6,** 4063–4073 (2014).

30. Watkins, T. & Buttry, D. a. Determination of Mg(2+) Speciation in a TFSI- Based Ionic Liquid With and Without Chelating Ethers Using Raman Spectroscopy. *J. Phys. Chem. B* (2015). doi:10.1021/acs.jpcb.5b00339

31. Ueno, K. *et al.* Anionic Effects on Solvate Ionic Liquid Electrolytes in Rechargeable Lithium–Sulfur Batteries. *J. Phys. Chem. C* **117,** 20509–20516 (2013).

32. Yoshida, K., Tsuchiya, M., Tachikawa, N., Dokko, K. & Watanabe, M. Correlation between Battery Performance and Lithium Ion Diffusion in Glyme-Lithium Bis(trifluoromethanesulfonyl)amide Equimolar Complexes. *J. Electrochem. Soc.* **159,** A1005–A1012 (2012).

33. Yoshida, K., Tsuchiya, M., Tachikawa, N., Dokko, K. & Watanabe, M. Change from Glyme Solutions to Quasi-ionic Liquids for Binary Mixtures Consisting of Lithium Bis(trifluoromethanesulfonyl)amide and Glymes. *J. Phys. Chem. C* **115,** 18384–18394 (2011).

34. Mandai, T. *et al.* Effect of ionic size on solvate stability of glyme-based solvate ionic liquids. *J. Phys. Chem. B* **119,** 1523–34 (2015).

35. Serizawa, N. *et al.* EQCM Measurement of Deposition and Dissolution of Lithium in Glyme-Li Salt Molten Complex. *J. Electrochem. Soc.* **160,** A1529–A1533 (2013).

36. Ueno, K. *et al.* Glyme-lithium salt equimolar molten mixtures: concentrated solutions or solvate ionic liquids? *J. Phys. Chem. B* **116,** 11323–31 (2012).

37. Mohtadi, R. & Mizuno, F. Magnesium batteries: Current state of the art, issues and future perspectives. *Beilstein J. Nanotechnol.* **5,** 1291–311 (2014).

Chapter 3

1. Yoo, H. D. *et al.* Mg rechargeable batteries: an on-going challenge. *Energy Environ. Sci.* **6,** 2265–2279 (2013).

2. Muldoon, J. *et al.* Electrolyte roadblocks to a magnesium rechargeable battery. *Energy Environ. Sci.* **5,** 5941–5950 (2012).

3. Muldoon, J., Bucur, C. B. & Gregory, T. Quest for Nonaqueous Multivalent Secondary Batteries: Magnesium and Beyond. *Chem. Rev.* **114,** 11683–11720 (2014).

4. Shterenberg, I., Salama, M., Gofer, Y., Levi, E. & Aurbach, D. The challenge of developing rechargeable magnesium batteries. *MRS Bull.* **39,** 453–460 (2014).

5. Fedorov, M. V & Kornyshev, A. A. Ionic liquids at electrified interfaces. *Chem. Rev.* **114,** 2978–3036 (2014).

6. MacFarlane, D. R. *et al.* Energy applications of ionic liquids. *Energy Environ. Sci.* **7,** 232–250 (2014).

7. Armand, M., Endres, F., MacFarlane, D. R., Ohno, H. & Scrosati, B. Ionic-liquid materials for the electrochemical challenges of the future. *Nat. Mater.* **8,** 621–9 (2009).

8. Cheek, G. T., O'Grady, W. E., El Abedin, S. Z., Moustafa, E. M. & Endres, F. Studies on the Electrodeposition of Magnesium in Ionic Liquids. *J. Electrochem. Soc.* **155,** D91–95 (2008).

9. Zhao, Q., NuLi, Y., Nasiman, T., Yang, J. & Wang, J. Reversible Deposition and Dissolution of Magnesium from Imidazolium-Based Ionic Liquids. *Int. J. Electrochem.* **2012,** 1–8 (2012).

10. Kitada, A., Kang, Y., Uchimoto, Y. & Murase, K. Room-Temperature Electrodeposition of Mg Metal from Amide Salts Dissolved in Glyme-Ionic Liquid Mixture. *J. Electrochem. Soc.* **161,** D102–D106 (2014).

11. Lu, Z., Schechter, A., Moshkovich, M. & Aurbach, D. On the electrochemical behavior of magnesium electrodes in polar aprotic electrolyte solutions. *J. Electroanal. Chem.* **466,** 203–217 (1999).

12. Vardar, G. *et al.* Electrochemistry of Magnesium Electrolytes in Ionic Liquids for Secondary Batteries. (2014).

13. Amir, N., Vestfrid, Y., Chusid, O., Gofer, Y. & Aurbach, D. Progress in nonaqueous magnesium electrochemistry. *J. Power Sources* **174,** 1234–1240 (2007).

14. Lodovico, L., Martins, V. L., Benedetti, T. M. & Torresi, R. M. Electrochemical Behavior of Iron and Magnesium in Ionic Liquids. *J. Braz. Chem. Soc.* **25,** 460–468 (2014).

15. Yoshimoto, N., Matsumoto, M., Egashia, M. & Morita, M. Mixed electrolyte consisting of ethylmagnesiumbromide with ionic liquid for rechargeable magnesium electrode. *J. Power Sources* **195,** 2096–2098 (2010).

16. Shimamura, O., Yoshimoto, N., Matsumoto, M., Egashia, M. & Morita, M. Electrochemical co-deposition of magnesium with lithium from quaternary ammonium-based ionic liquid. *J. Power Sources* **196,** 1586–1588 (2011).

17. Kakibe, T., Hishii, J., Yoshimoto, N., Egashira, M. & Morita, M. Binary ionic liquid electrolytes containing organo-magnesium complex for rechargeable magnesium batteries. *J. Power Sources* **203,** 195–200 (2012).

18. Monteiro, M. J., Bazito, F. F. C., Siqueira, L. J. a, Ribeiro, M. C. C. & Torresi, R. M. Transport coefficients, Raman spectroscopy, and computer simulation of lithium salt solutions in an ionic liquid. *J. Phys. Chem. B* **112,** 2102–2109 (2008).

19. Lassègues, J.-C., Grondin, J. & Talaga, D. Lithium solvation in bis(trifluoromethanesulfonyl)imide-based ionic liquids. *Phys. Chem. Chem. Phys.* **8,** 5629–32 (2006).

20. Lassègues, J., Grondin, J., Aupetit, C. & Johansson, P. Spectroscopic Identification of the Lithium Ion Transporting Species in LiTFSI-Doped Ionic Liquids. *J. Phys. Chem. A.* **113,** 305–314 (2009).

21. Duluard, S. *et al.* Lithium solvation and diffusion in the bis(trifluoromethanesulfonyl)imide ionic liquid. *J. Raman Spectrosc.* **39,** 627–632 (2008).

22. Umebayashi, Y. *et al.* Lithium ion solvation in room-temperature ionic liquids involving bis(trifluoromethanesulfonyl) imide anion studied by Raman spectroscopy and DFT calculations. *J. Phys. Chem. B* **111,** 13028–32 (2007).

23. Castriota, M. *et al.* Raman Investigation of the Ionic Liquid N -Methyl- N -propylpyrrolidinium Bis (trifluoromethanesulfonyl) imide and Its Mixture with LiN (SO 2 CF 3) 2. 92–96 (2005).

24. Hardwick, L. J., Holzapfel, M., Wokaun, A. & Petr, N. Raman study of lithium coordination in EMI-TFSI additive systems as lithium-ion battery ionic liquid electrolytes. *J. Raman Spectrosc.* **38,** 110–112 (2007).

25. Borodin, O., Smith, G. D. & Henderson, W. Li+ Cation Environment, Transport, and Mechanical Properties of the LiTFSI Doped N-Methyl-N-alkylpyrrolidinium+TFSI- Ionic Liquids. *J. Phys. Chem. B.* **110,** 16879–16886 (2006).

26. Nicotera, I., Oliviero, C., Henderson, W. A., Appetecchi, G. B. & Passerini, S. NMR Investigation of Ionic Liquid-LiX Mixtures: Pyrrolidinium Cations and TFSI- Anions. *J. Phys. Chem. B.* **109,** 22814–22819 (2005).

27. Saito, Y., Umecky, T., Niwa, J., Sakai, T. & Maeda, S. Existing condition and migration property of ions in lithium electrolytes with ionic liquid solvent. *J. Phys. Chem. B* **111,** 11794–802 (2007).

28. Umecky, T., Saito, Y., Okumura, Y., Maeda, S. & Sakai, T. Ionization condition of lithium ionic liquid electrolytes under the solvation effect of liquid and solid solvents. *J. Phys. Chem. B* **112,** 3357–64 (2008).

29. Matsumoto, K., Hagiwara, R. & Tamada, O. Coordination environment around the lithium cation in solid Li2(EMIm)(N(SO2CF3)2)3 (EMIm=1-ethyl-3-methylimidazolium): Structural clue of ionic liquid electrolytes for lithium batteries. *Solid State Sci.* **8,** 1103–1107 (2006).

30. Zhou, Q., Fitzgerald, K., Boyle, P. D. & Henderson, W. A. Phase Behavior and Crystalline Phases of Ionic Liquid-Lithium Salt Mixtures with 1-Alkyl-3-methylimidazolium Salts. *Chem. Mater.* **22,** 1203–1208 (2010).

31. Zhou, Q. *et al.* Phase Behavior of Ionic Liquid-LiX Mixtures: Pyrrolidinium Cations and TFSI- Anions - Linking Structure to Transport Properties. *Chem. Mater.* **23,** 4331–4337 (2011).

32. Henderson, W. A. & Passerini, S. Phase Behavior of Ionic Liquid - LiX Mixtures : Pyrrolidinium Cations and TFSI - Anions. 2881–2885 (2004).

33. Nowinski, J. L., Lightfoot, P. & Bruce, P. G. Structure of LiN(CF3S02)2, a Novel Salt for Electrochemistry. *J. Mater. Chem.* **4,** 1579–1580 (1994).

34. Giffin, G., Moretti, A., Jeong, S. & Passerini, S. Complex Nature of Ionic Coordination in Magnesium Ionic Liquid-Based Electrolytes: Solvates with Mobile Mg2+ Cations. *J. Phys. Chem. C* **118,** 9966–9973 (2014).

35. Shirai, A. *et al.* Solvation of Lithium Ion in N,N-Diethyl-N-methyl-N-(2-methoxyethyl)ammonium Bis(trifluoromethanesulfonyl)-amide Using Raman and Multinuclear NMR Spectroscopy. *Anal. Sci.* **24,** 1291–1296 (2008).

36. Dillon, R. E. A. & Shriver, D. F. Ion Transport in Cryptand and Crown Ether Lithium Salt Complexes. *Chem. Mater.* **11,** 3296–3301 (1999).

37. Brouillette, D. *et al.* Stable solvates in solution of lithium bis(trifluoromethylsulfone)imide in glymes and other aprotic solvents: Phase diagrams, crystallography and Raman spectroscopy. *Phys. Chem. Chem. Phys.* **4,** 6063–6071 (2002).

38. Henderson, W. A., Brooks, N. R., Brennessel, W. W. & Young, V. G. Triglyme-Li+ Cation Solvate Structures: Models for Amorphous Concentrated Liquid and Polymer Electrolytes (I). *Chem. mater.* **15,** 4679–4684 (2003).

39. Choquette, Y. *et al.* Sulfamides and Glymes as Aprotic Solvents for Lithium Batteries. *J. Electrochem. Soc.* **145,** 3500–3507 (1998).

40. Dillon, R. E. A. & Shriver, D. F. Influence of cation size on ionic glass formation and ionic conductivity. *Solid State Ionics* **132,** 93–99 (2000).

41. Dillon, R. E. A., Stern, C. L. & Shriver, D. F. Influence of the Anion on the Formation of Amorphous Ionically Conducting Lithium Salt Complexes with 18-C-6 and 2.2.2-Cryptand Macrocycles. *Chem. Mater.* **13,** 2516–2522 (2001).

42. Hayamizu, K., Akiba, E., Bando, T. & Aihara, Y. 1H, 7Li, and 19F nuclear magnetic resonance and ionic conductivity studies for liquid electrolytes composed of glymes and polyetheneglycol dimethyl ethers of CH3O(CH2CH2O)n CH3 (n=3–50) doped with LiN(SO2CF3)2. *J. Chem. Phys.* **117,** 5929–5939 (2002).

43. Henderson, W. A. Glyme-Lithium Salt Phase Behavior. *J. Phys. Chem. B.* **110,** 13177–13183 (2006).

44. Pappenfus, T. M., Henderson, W. A., Owens, B. B., Mann, K. R. & Smyrl, W. H. Complexes of Lithium Imide Salts with Tetraglyme and Their Polyelectrolyte Composite Materials. *J. Electrochem. Soc.* **151,** A209–A215 (2004).

45. Mandai, T., Yoshida, K., Ueno, K., Dokko, K. & Watanabe, M. Criteria for solvate ionic liquids. *Phys. Chem. Chem. Phys.* **16,** 8761–72 (2014).

46. Ueno, K. *et al.* Glyme-lithium salt equimolar molten mixtures: concentrated solutions or solvate ionic liquids? *J. Phys. Chem. B* **116,** 11323–31 (2012).

47. Yoshida, K. *et al.* Oxidative-stability enhancement and charge transport mechanism in glyme-lithium salt equimolar complexes. *J. Am. Chem. Soc.* **133,** 13121–9 (2011).

48. Yoshida, M., Tsuchiya, M., Tachikawa, N., Dokko, K. & Watanabe, M. Solvate Ionic Liquids and Their Application to Li Batteries: Glyme-Li Bis(fluorosulfonyl)amide Equimolar Complexes. *Mater. Res. Soc. Symp. Proc.* **1473,** (2012).

49. Zhang, C. *et al.* Chelate Effects in Glyme/Lithium Bis(trifluoromethanesulfonyl)amide Solvate Ionic Liquids. I. Stability of Solvate Cations and Correlation with Electrolyte Properties. *J. Phy* **118,** 5144–5153 (2014).

50. Zhang, C. *et al.* Chelate Effects in Glyme/Lithium Bis(trifluoromethanesulfonyl)amide Solvate Ionic Liquids, Part 2: Importance of Solvate-Structure Stability for Electrolytes of Lithium Batteries. *J. Phys. Chem. C* **118,** 17362–17373 (2014).

51. Angell, C. A. A New Class of Molten Salt Mixtures The Hydrated Dipositive Ion as an Independent Cation Species. *J. Electrochem. Soc.* **112,** 1224 (1965).

52. Bayley, P. M., Lane, G. H., Lyons, L. J., MacFarlane, D. R. & Forsyth, M. Undoing Lithium Ion Association in Ionic Liquids through the Complexation by Oligoethers †. *J. Phys. Chem. C* **114,** 20569–20576 (2010).

53. Angell, A. C., Ansari, Y. & Zhao, Z. Ionic Liquids: Past, present and future. *Faraday Discuss.* **154,** 9–27 (2012).

54. Appetecchi, G. B., Scaccia, S., Tizzani, C., Alessandrini, F. & Passerini, S. Synthesis of Hydrophobic Ionic Liquids for Electrochemical Applications. *J. Electrochem. Soc.* **153,** A1685–A1691 (2006).

55. Johansson, P., Gejji, S. P., Tegenfeldt, J. & Lindgren, J. The imide ion: potential energy surface and geometries. *Electrochim. Acta* **43,** 1375–1379 (1998).

56. Herstedt, M. *et al.* Spectroscopic characterization of the conformational states of the bis(trifluoromethanesulfonyl)imide anion (TFSI−). *J. Raman Spectrosc.* **36,** 762–770 (2005).

57. Shin, J.-H., Henderson, W. A. & Passerini, S. An Elegant Fix for Polymer Electrolytes. *Electrochem. Solid-State Lett.* **8,** A125–A127 (2005).

58. Fujii, K. *et al.* Conformational equilibrium of bis(trifluoromethanesulfonyl) imide anion of a room-temperature ionic liquid: Raman spectroscopic study and DFT calculations. *J. Phys. Chem. B* **110,** 8179–83 (2006).

59. Rey, I. *et al.* Spectroscopic and Theoretical Study of (CF3SO2)2N- (TFSI-) and (CF3SO2)2NH (HTFSI). *J. Phys. Chem. A* **102,** 3249–3258 (1998).

60. Xue, L., Padgett, C. W., DesMarteau, D. D. & Pennington, W. T. Synthesis and structures of alkali metal salts of bis[(trifluoromethyl)sulfonyl]imide. *Solid State Sci.* **4,** 1535–1545 (2002).

61. Seo, D. M., Borodin, O., Han, S.-D., Boyle, P. D. & Henderson, W. A. Electrolyte Solvation and Ionic Association II. Acetonitrile-Lithium Salt Mixtures: Highly Dissociated Salts. *J. Electrochem. Soc.* **159,** A1489–A1500 (2012).

62. Seo, D. M. *et al.* Solvate structures and spectroscopic characterization of LiTFSI electrolytes. *J. Phys. Chem. B* **118,** 13601–13608 (2014).

63. Qian, J. *et al.* High rate and stable cycling of lithium metal anode. *Nat. Commun.* **6,** 6362 (2015).

64. Rajput, N. N., Qu, X., Sa, N., Burrell, A. K. & Persson, K. a. The Coupling between Stability and Ion Pair Formation in Magnesium Electrolytes from First-Principles Quantum Mechanics and Classical Molecular Dynamics. *J. Am. Chem. Soc.* **137,** 3411–3420 (2015).

65. Henderson, W. A. *et al.* Glyme-Lithium Bis(trifluoromethanesulfonyl)imide and Glyme-Lithium Bis(perfluoroethanesulfonyl)imide Phase Behavior and Solvate Structures. *Chem. Mater.* **17,** 2284–2289 (2005).

66. Gutman, V. *The Donor-Acceptor Approach to Molecular Interactions*. (Plenum Press, 1987).

67. Umebayashi, Y. *et al.* Raman spectroscopic studies and ab initio calculations on conformational isomerism of 1-butyl-3-methylimidazolium bis-(trifluoromethanesulfonyl)amide solvated to a lithium ion in ionic liquids: effects of the second solvation sphere of the lithium ion. *J. Phys. Chem. B* **114,** 6513–21 (2010).

68. Fujii, K., Nonaka, T., Akimoto, Y., Umebayashi, Y. & Ishiguro, S. Solvation Structures of Some Transition Metal(II) Ions in a Room-Temperature Ionic Liquid , 1-Ethyl-3-methylimidazolium Bis(trifluoromethanesulfonyl) amide. *Anal. Sci.* **24,** 1377–1380 (2008).

69. Rudolph, W. W., Irmer, G. & Hefter, G. T. Raman spectroscopic investigation of speciation in MgSO4(aq). *Phys. Chem. Chem. Phys.* **5,** 5253–5261 (2003).

70. Bradley, M. S. & Krech, J. H. High-pressure Raman Spectra of the Acetone C-C Stretch in Binary Liquid Mixtures with Methanol. *J. Phys. Chem.* **96,** 75–79 (1992).

71. Bock, C. W., Kaufman, A. & Glusker, J. P. Coordination of water to magnesium cations. *Inorg. Chem.* **33,** 419–427 (1994).

72. Ha, S. *et al.* Magnesium(II) Bis(trifluoromethane sulfonyl) Imide-Based Electrolytes with Wide Electrochemical Windows for Rechargeable Magnesium Batteries. *Appl. Mater. Interfaces* **6,** 4063–4073 (2014).

73. Kim, I.-T., Yamabuki, K., Morita, M., Tsutsumi, H. & Yoshimoto, N. Effects of alkoxide addition on the electrochemical deposition and dissolution in triglyme-based solution dissolving magnesium bis(trifluoromethanesulfonyl)amide. *J. Power Sources* **278,** 340–343 (2015).

74. Bakker, A., Gejji, S., Lindgren, J. & Hermansson, K. Contact Ion Pair Formation and Ether Oxygen Coordination in the Polymer Electrolytes M[N(CF3SO2)2]2PEOn for M = Mg, Ca, Sr and Ba. *Polymer (Guildf).* **36,** 4371–4378 (1995).

75. Izatt, R. M., Bradshaw, J. S., Nielsen, S. A., Lamb, J. D. & Christensen, J. J. Thermodynamic and Kinetic Data for Cation-Macrocycle Interaction. *J. Chem. Rev.* **85,** 271–339 (1985).

Chapter 4

1. Yoo, H. D. *et al.* Mg rechargeable batteries: an on-going challenge. *Energy Environ. Sci.* **6,** 2265–2279 (2013).

2. Mohtadi, R. & Mizuno, F. Magnesium batteries: Current state of the art, issues and future perspectives. *Beilstein J. Nanotechnol.* **5,** 1291–311 (2014).

3. Muldoon, J., Bucur, C. B. & Gregory, T. Quest for Nonaqueous Multivalent Secondary Batteries: Magnesium and Beyond. *Chem. Rev.* **114,** 11683–11720 (2014).

4. Park, M.-S., Kim, J.-G., Kim, Y.-J., Choi, N.-S. & Kim, J.-S. Recent Advances in Rechargeable Magnesium Battery Technology: A Review of the Field's Current Status and Prospects. *Isr. J. Chem.* **55,** 570–585 (2015).

5. Liu, T. *et al.* A fundamental study on the [(μ-Cl)3Mg2(THF)6](+) dimer electrolytes for rechargeable Mg batteries. *Chem. Commun. (Camb).* **51,** 2312–5 (2015).

6. Muldoon, J. *et al.* Electrolyte roadblocks to a magnesium rechargeable battery. *Energy Environ. Sci.* **5,** 5941–5950 (2012).

7. Muldoon, J. *et al.* Corrosion of magnesium electrolytes: chlorides – the culprit. *Energy Environ. Sci.* **6,** 482 (2013).

8. Lv, D. *et al.* A Scientific Study of Current Collectors for Mg Batteries in Mg(AlCl2EtBu)2/THF Electrolyte. *J. Electrochem. Soc.* **160,** A351–A355 (2012).

9. Yagi, S., Tanaka, a., Ichikawa, Y., Ichitsubo, T. & Matsubara, E. Electrochemical Stability of Magnesium Battery Current Collectors in a Grignard Reagent-Based Electrolyte. *J. Electrochem. Soc.* **160,** C83–C88 (2013).

10. Aurbach, D. *et al.* Electrolyte Solutions for Rechargeable Magnesium Batteries Based on Organomagnesium Chloroaluminate Complexes. *J. Electrochem. Soc.* **149,** A115 (2002).

11. Shao, Y. *et al.* Coordination chemistry in magnesium battery electrolytes: how ligands affect their performance. *Sci. Rep.* **3,** 3130 (2013).

12. Tuerxun, F. *et al.* High concentration magnesium borohydride/tetraglyme electrolyte for rechargeable magnesium batteries. *J. Power Sources* **276,** 255–261 (2015).

13. Mohtadi, R. Borohydride Solvo-Ionic Liquid Family For Magnesium Battery. **1,** 1–4 (2015).

14. Mohtadi, R., Matsui, M., Arthur, T. S. & Hwang, S.-J. Magnesium borohydride: from hydrogen storage to magnesium battery. *Angew. Chem. Int. Ed. Engl.* **51,** 9780–3 (2012).

15. Shterenberg, I., Salama, M., Gofer, Y., Levi, E. & Aurbach, D. The challenge of developing rechargeable magnesium batteries. *MRS Bull.* **39,** 453–460 (2014).

16. Rajput, N. N., Qu, X., Sa, N., Burrell, A. K. & Persson, K. a. The Coupling between Stability and Ion Pair Formation in Magnesium Electrolytes from First-Principles Quantum Mechanics and Classical Molecular Dynamics. *J. Am. Chem. Soc.* **137,** 3411–3420 (2015).

17. Shao, Y. *et al.* Nanocomposite polymer electrolyte for rechargeable magnesium batteries. *Nano Energy* **12,** 750–759 (2015).

18. Chang, J. *et al.* Synergetic Role of Li(+) during Mg Electrodeposition/Dissolution in Borohydride Diglyme Electrolyte Solution: Voltammetric Stripping Behaviors on a Pt Microelectrode Indicative of Mg-Li Alloying and Facilitated Dissolution. *ACS Appl. Mater. Interfaces* **7,** 2494–2502 (2015).

19. MacFarlane, D. R. *et al.* Energy applications of ionic liquids. *Energy Environ. Sci.* **7,** 232–250 (2014).

20. NuLi, Y., Yang, J., Wang, J., Xu, J. & Wang, P. Electrochemical Magnesium Deposition and Dissolution with High Efficiency in Ionic Liquid. *Electrochem. Solid-State Lett.* **8,** C166 (2005).

21. NuLi, Y., Yang, J. & Wang, P. Electrodeposition of magnesium film from BMIMBF4 ionic liquid. *Appl. Surf. Sci.* **252,** 8086–8090 (2006).

22. Zhao, Q., NuLi, Y., Nasiman, T., Yang, J. & Wang, J. Reversible Deposition and Dissolution of Magnesium from Imidazolium-Based Ionic Liquids. *Int. J. Electrochem.* **2012,** 1–8 (2012).

23. Lodovico, L., Martins, V. L., Benedetti, T. M. & Torresi, R. M. Electrochemical Behavior of Iron and Magnesium in Ionic Liquids. *J. Braz. Chem. Soc.* **25,** 460–468 (2014).

24. Vardar, G. *et al.* Electrochemistry of magnesium electrolytes in ionic liquids for secondary batteries. *ACS Appl. Mater. Interfaces* **6,** 18033–18039 (2014).

25. Giffin, G., Moretti, A., Jeong, S. & Passerini, S. Complex Nature of Ionic Coordination in Magnesium Ionic Liquid-Based Electrolytes: Solvates with Mobile Mg2+ Cations. *J. Phys. Chem. C* **118,** 9966–9973 (2014).

26. Watkins, T. & Buttry, D. A. Determination of Mg2+ Speciation in a TFSI−-Based Ionic Liquid With and Without Chelating Ethers Using Raman Spectroscopy. *J. Phys. Chem. B* **119,** 7003–7014 (2015).

27. Venkata Narayanan, N. S., Ashok Raj, B. V. & Sampath, S. Magnesium ion conducting, room temperature molten electrolytes. *Electrochem. commun.* **11,** 2027–2031 (2009).

28. Narayanan, N. S. V., Ashok Raj, B. V. & Sampath, S. Physicochemical, spectroscopic and electrochemical characterization of magnesium ion-conducting, room temperature, ternary molten electrolytes. *J. Power Sources* **195,** 4356–4364 (2010).

29. Murase, K. *et al.* Enhanced Anodic Dissolution of Magnesium in Quaternary-Ammonium-Based Ionic Liquid Containing a Small Amount of Water. *J. Electrochem. Soc.* **160,** D453–D458 (2013).

30. Kar, M., Winther-Jensen, B., Forsyth, M. & MacFarlane, D. R. Chelating ionic liquids for reversible zinc electrochemistry. *Phys. Chem. Chem. Phys.* **15,** 7191–7 (2013).

31. Giffin, G. a., Tannert, J., Jeong, S., Uhl, W. & Passerini, S. Crystalline Complexes of Pyr 12O1 TFSI-Based Ionic Liquid Electrolytes. *J. Phys. Chem. C* **119,** 5878–5887 (2015).

32. Dobbelin, M. *et al.* Synthesis of Pyrrolidinium-Based Poly (ionic liquid) Electrolytes with Poly (ethylene glycol) Side Chains. *Chem. Mater.* **24,** 1583–1590 (2012).

33. Ganapatibhotla, L. V. N. R., Zheng, J., Roy, D. & Krishnan, S. PEGylated Imidazolium Ionic Liquid Electrolytes: Thermophysical and Electrochemical Properties. *Chem. Mater.* **22,** 6347–6360 (2010).

34. Marks, T. J., Kolb, J. R. & Introduction, I. Covalent Transition Metal, Lanthanide, and Actinide Tetrahydroborate Complexes. *Chem. Rev.* **77,** 263–293 (1976).

35. Shirk, a. E. & Shriver, D. F. Solvent and cation dependence of the tetrahydroborate, BH4-, Raman spectrum. *J. Am. Chem. Soc.* **95,** 5901–5904 (1973).

36. Marks, T. J., Kennelly, W. J., Kolb, J. R. & Shimp, L. a. Structure and dynamics in metal tetrahydroborates. II. Vibrational spectra and structures of some transition metal and actinide tetrahydroborates - NO COPY. *Inorg. Chem.* **11,** 2540–2546 (1972).

37. Davies, N., Bird, P. H. & Wallbridge, M. G. H. Spectroscopic Studies on Derivatives of Aluminium Borohydride. *J. Chem. Soc. A* 2269–2272 (1968).

38. Emery, A. R. & Taylor, R. C. Raman Spectroscopy in Liquid Ammonia Solutions. Vibrational Frequencies and Force Constants for Isotopic Species of the Borohydride Ion Having Tetrahedral Symmetry. *J. Chem. Phys* **3848,** 1953–1956 (1958).

39. Dalton, D. A., Somayazulu, M., Goncharov, A. F. & Hemley, R. J. Static compression of tetramethylammonium borohydride. *J. Phys. Chem. A* **115,** 11033–11038 (2011).

40. Brouillette, D. *et al.* Stable solvates in solution of lithium bis(trifluoromethylsulfone)imide in glymes and other aprotic solvents: Phase diagrams, crystallography and Raman spectroscopy. *Phys. Chem. Chem. Phys.* **4,** 6063–6071 (2002).

41. Monteiro, M. J., Bazito, F. F. C., Siqueira, L. J. a, Ribeiro, M. C. C. & Torresi, R. M. Transport coefficients, Raman spectroscopy, and computer simulation of lithium salt solutions in an ionic liquid. *J. Phys. Chem. B* **112,** 2102–2109 (2008).

42. Lassègues, J.-C., Grondin, J. & Talaga, D. Lithium solvation in bis(trifluoromethanesulfonyl)imide-based ionic liquids. *Phys. Chem. Chem. Phys.* **8,** 5629–32 (2006).

43. Lassègues, J., Grondin, J., Aupetit, C. & Johansson, P. Spectroscopic Identification of the Lithium Ion Transporting Species in LiTFSI-Doped Ionic Liquids. *J. Phys. Chem. A.* **113,** 305–314 (2009).

44. Duluard, S. *et al.* Lithium solvation and diffusion in the bis(trifluoromethanesulfonyl)imide ionic liquid. *J. Raman Spectrosc.* **39,** 627–632 (2008).

45. Umebayashi, Y. *et al.* Lithium ion solvation in room-temperature ionic liquids involving bis(trifluoromethanesulfonyl) imide anion studied by Raman spectroscopy and DFT calculations. *J. Phys. Chem. B* **111,** 13028–32 (2007).

46. Castriota, M. *et al.* Raman Investigation of the Ionic Liquid N-Methyl-N-propylpyrrolidinium Bis(trifluoromethanesulfonyl)imide and Its Mixture with LiN(SO2CF3)2. *J. Phys. Chem. A* **109,** 92–96 (2005).

47. Hardwick, L. J., Holzapfel, M., Wokaun, A. & Petr, N. Raman study of lithium coordination in EMI-TFSI additive systems as lithium-ion battery ionic liquid electrolytes. *J. Raman Spectrosc.* **38,** 110–112 (2007).

48. Borodin, O., Smith, G. D. & Henderson, W. Li+ Cation Environment, Transport, and Mechanical Properties of the LiTFSI Doped N-Methyl-N-alkylpyrrolidinium+TFSI- Ionic Liquids. *J. Phys. Chem. B.* **110,** 16879–16886 (2006).

49. Herstedt, M. *et al.* Spectroscopic characterization of the conformational states of the bis(trifluoromethanesulfonyl)imide anion (TFSI−). *J. Raman Spectrosc.* **36,** 762–770 (2005).

50. Tutusaus, O. *et al.* An Efficient Halogen-Free Electrolyte for Use in Rechargeable Magnesium Batteries. *Angew. Chem. Int. Ed. Engl.* 1–6 (2015). doi:10.1002/anie.201412202

51. Ha, S. *et al.* Magnesium(II) Bis(trifluoromethane sulfonyl) Imide-Based Electrolytes with Wide Electrochemical Windows for Rechargeable Magnesium Batteries. *Appl. Mater. Interfaces* **6,** 4063–4073 (2014).

52. Kitada, A., Kang, Y., Uchimoto, Y. & Murase, K. Room-Temperature Electrodeposition of Mg Metal from Amide Salts Dissolved in Glyme-Ionic Liquid Mixture. *J. Electrochem. Soc.* **161,** D102–D106 (2014).

53. Fukutsuka, T. *et al.* New Magnesium-ion Conductive Electrolyte Solution Based on Triglyme for Reversible Magnesium Metal Deposition and Dissolution at Ambient Temperature. *Chem. Lett.* **43,** 1788–1790 (2014).

Chapter 5

1. Giffin, G. a., Tannert, J., Jeong, S., Uhl, W. & Passerini, S. Crystalline Complexes of Pyr_{12O1} TFSI-Based Ionic Liquid Electrolytes. *J. Phys. Chem. C* **119,** 5878–5887 (2015).

APPENDIX A

SUPPORTING INFORMATION FOR CHAPTER 4

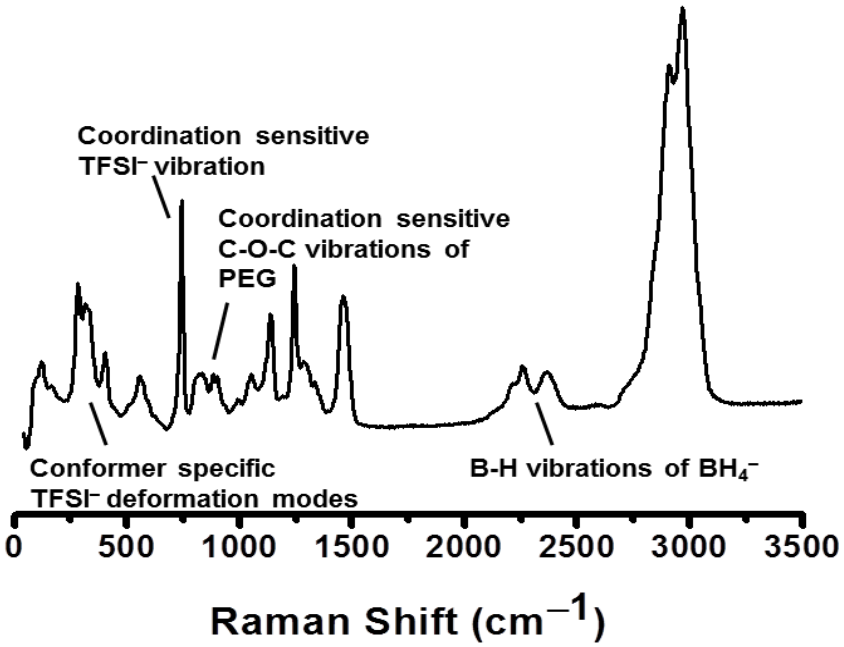

Figure A1: Raman spectrum (50–3800 cm^{-1}) for electrolyte with composition $[Mg(BH_4)_2]_{0.3}[MPEG_7PyrTFSI]_{0.7}$. The four major regions of interest mentioned in the text are identified.

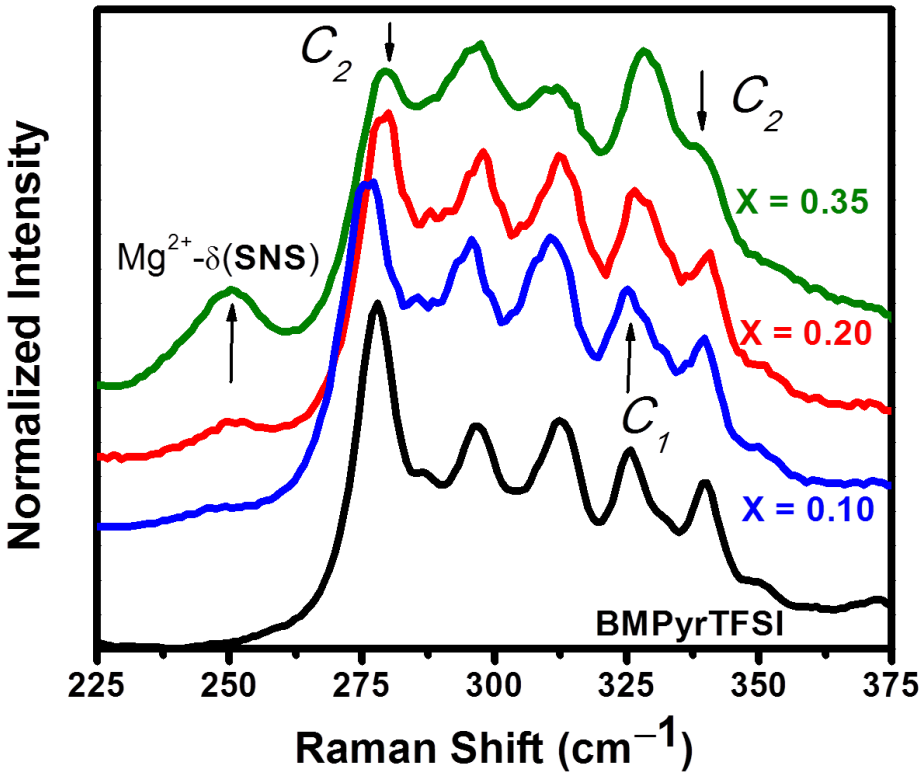

Figure A2: Conformational specific region for $TFSI^-$ modes at given $Mg(BH_4)_2$ mole fractions (x) in BMPyrTFSI, $[Mg(BH_4)_2]_x[BMPyrTFSI]_{1-x}$. The cis (*C1*) conformer increases, while the trans (*C2*) conformer decreases as the mole fraction of $Mg(BH_4)_2$ increases. This is consistent with previous reports for Mg^{2+} with $TFSI^-$ (references 26 and 31 in the main text). The mode at 250 also increases with an increase in $Mg(BH_4)_2$ and has been briefly described in references 26 and 32.

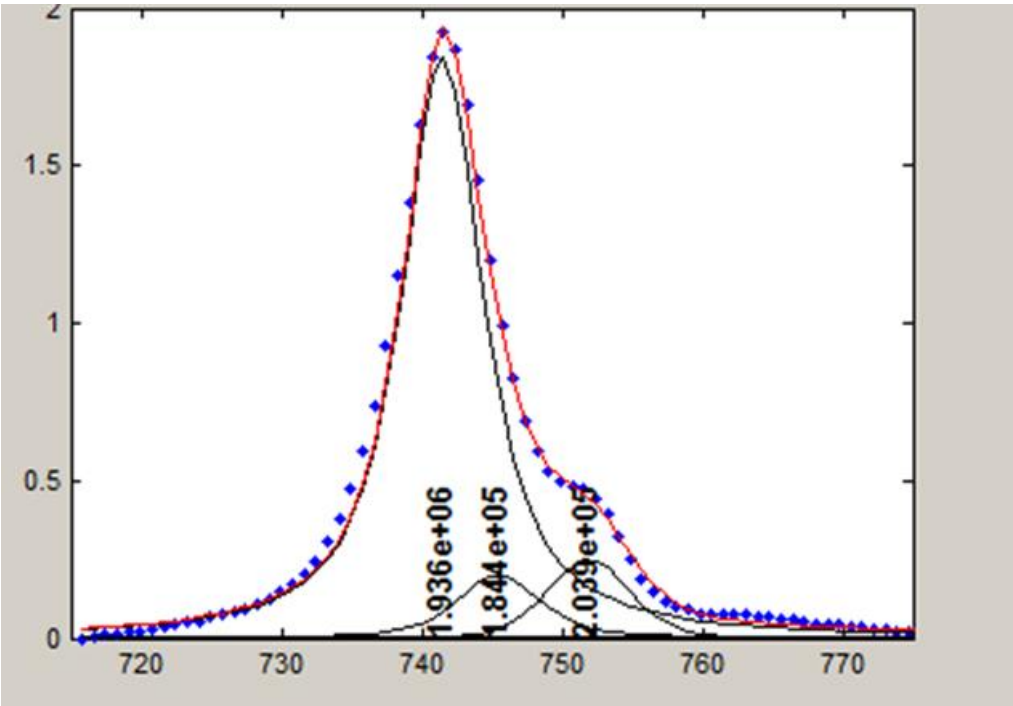

Figure A3: Example modeled fit for the coordination sensitive $TFSI^-$ peak in an electrolyte with composition $[Mg(BH_4)_2]_{0.15}[MPEG_7PyrTFSI]_{0.85}$.

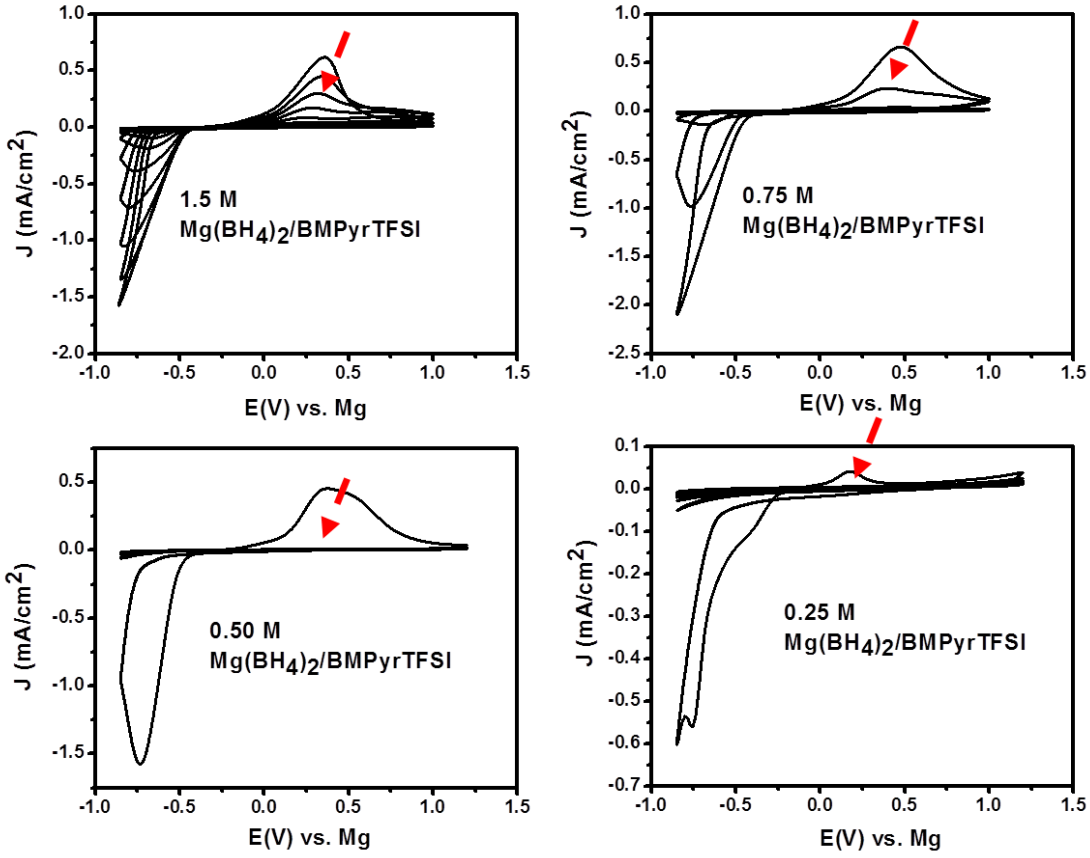

Figure A4: Successive CVs for $Mg(BH_4)_2$/BMPyrTFSI electrolytes at a) 1.5 M b) 0.75 M c) 0.50 M and d) 0.25 M.

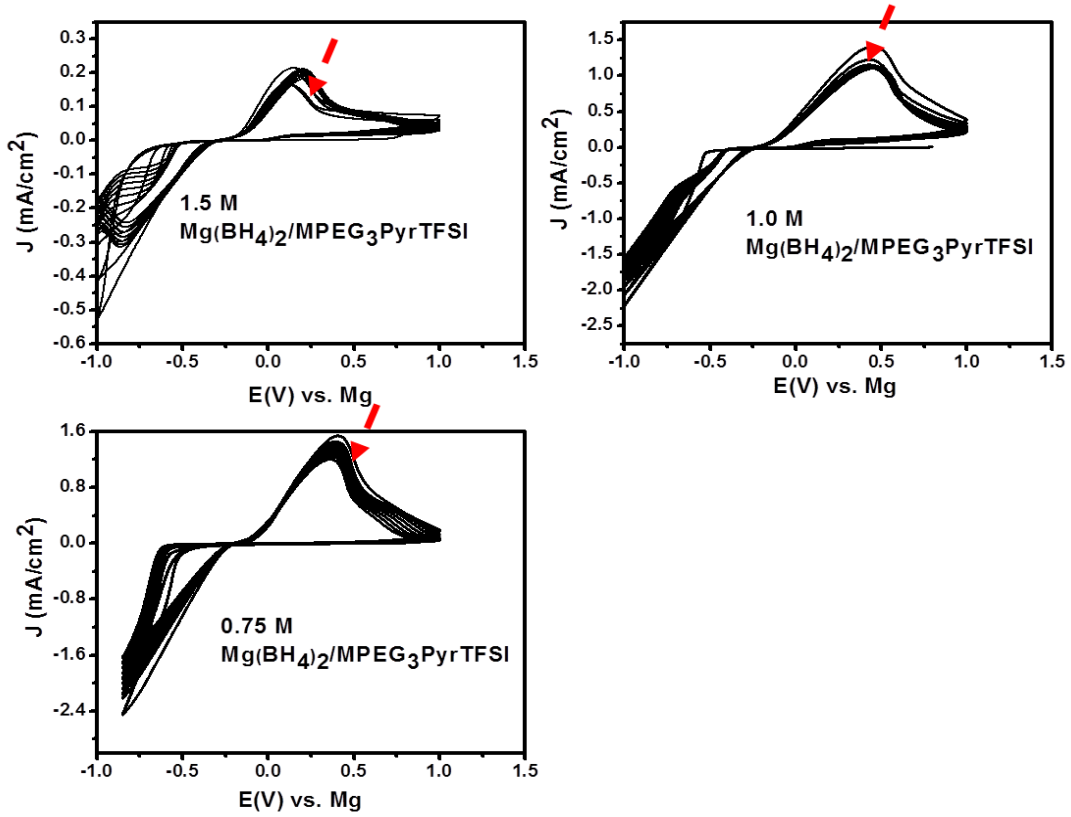

Figure A5: Successive CVs for $Mg(BH_4)_2$/$MPEG_3$PyrTFSI electrolytes at a) 1.5 M b) 1.0 M and c) 0.75 M

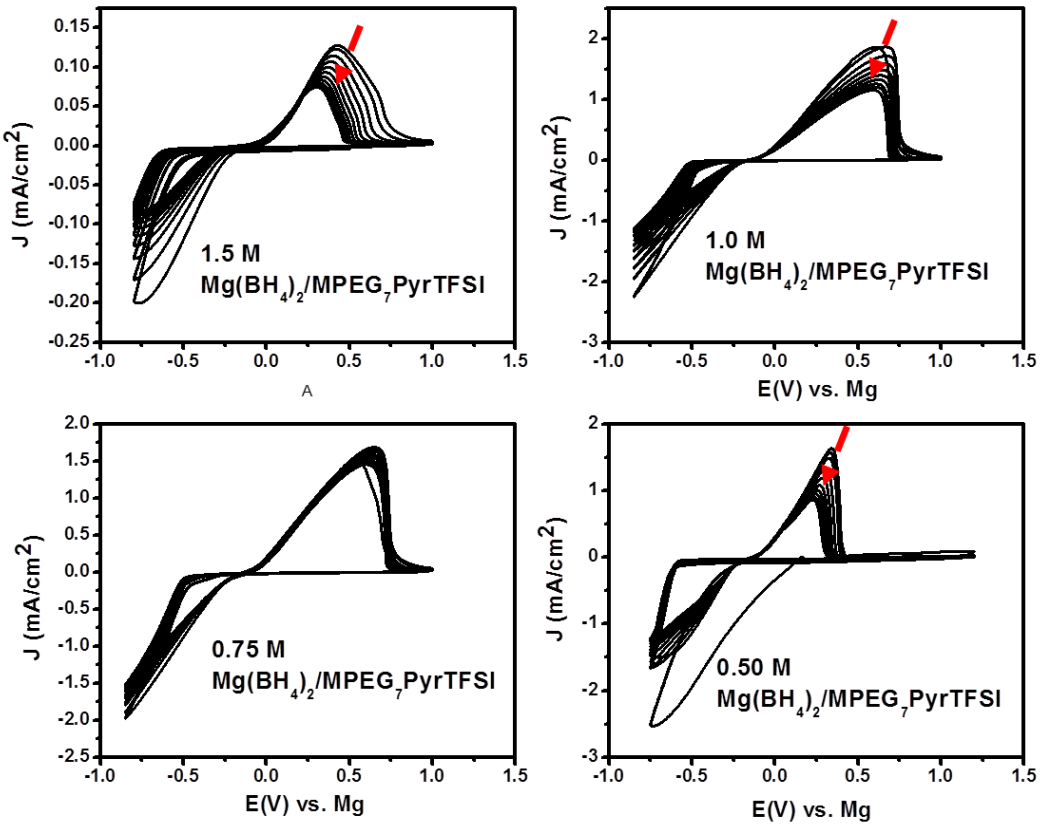

Figure A6: Successive CVs for $Mg(BH_4)_2$/$MPEG_7$PyrTFSI electrolytes at a) 1.5 M b) 1.0 M c) 0.75 M and d) 0.25 M.

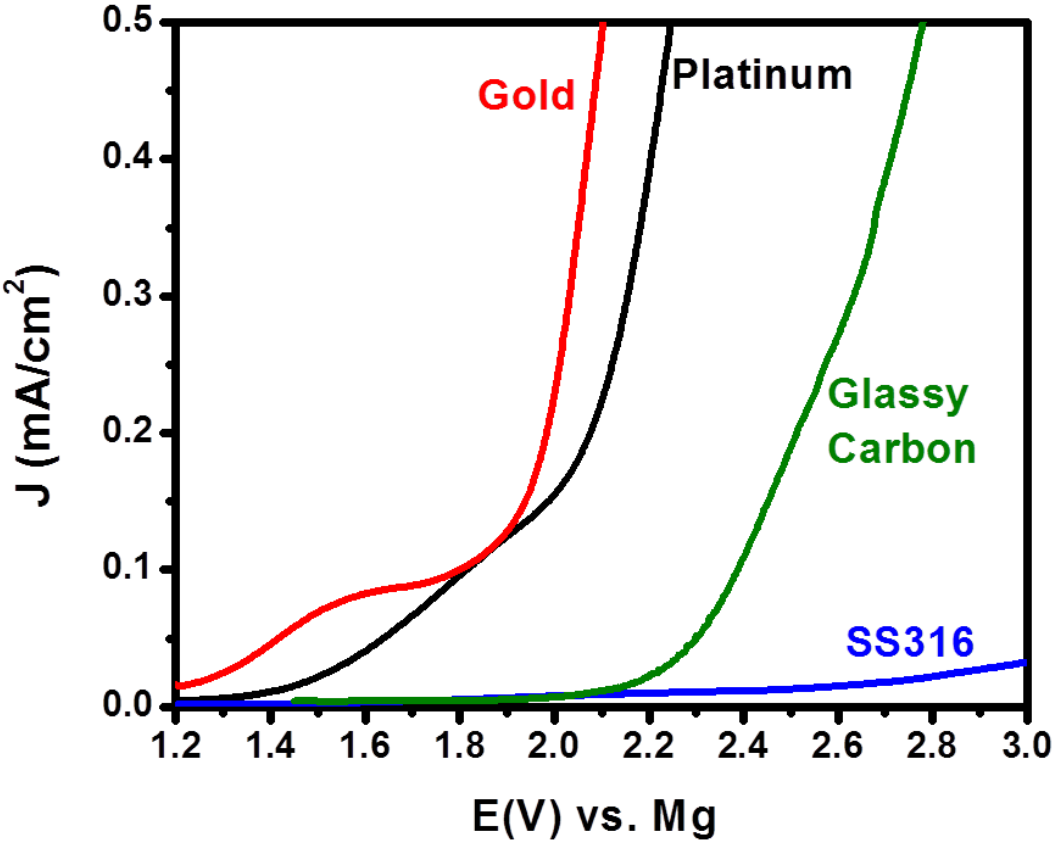

Figure A7: Linear sweep voltammegrams for 0.5 M Mg(BH4)2/MPEG7PyrTFSI. The working electrodes are indicated in the figure, the reference and counter electrodes were polished Mg and the scan rate was 1 mV/s. Note: a two electrode set-up was used for the stainless steel (SS316) measurement.

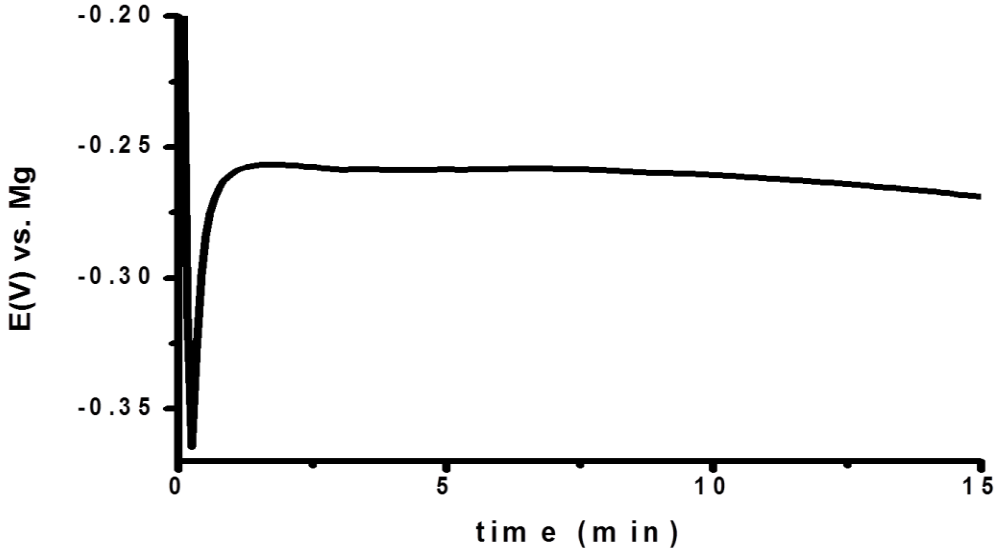

Figure A8: Potential trace (first 15 minutes) for 0.1 mA/cm^2 galvanostatic deposition of Mg on Au in 0.5 M $Mg(BH_4)_2$/$MPEG_7PyrTFSI$.

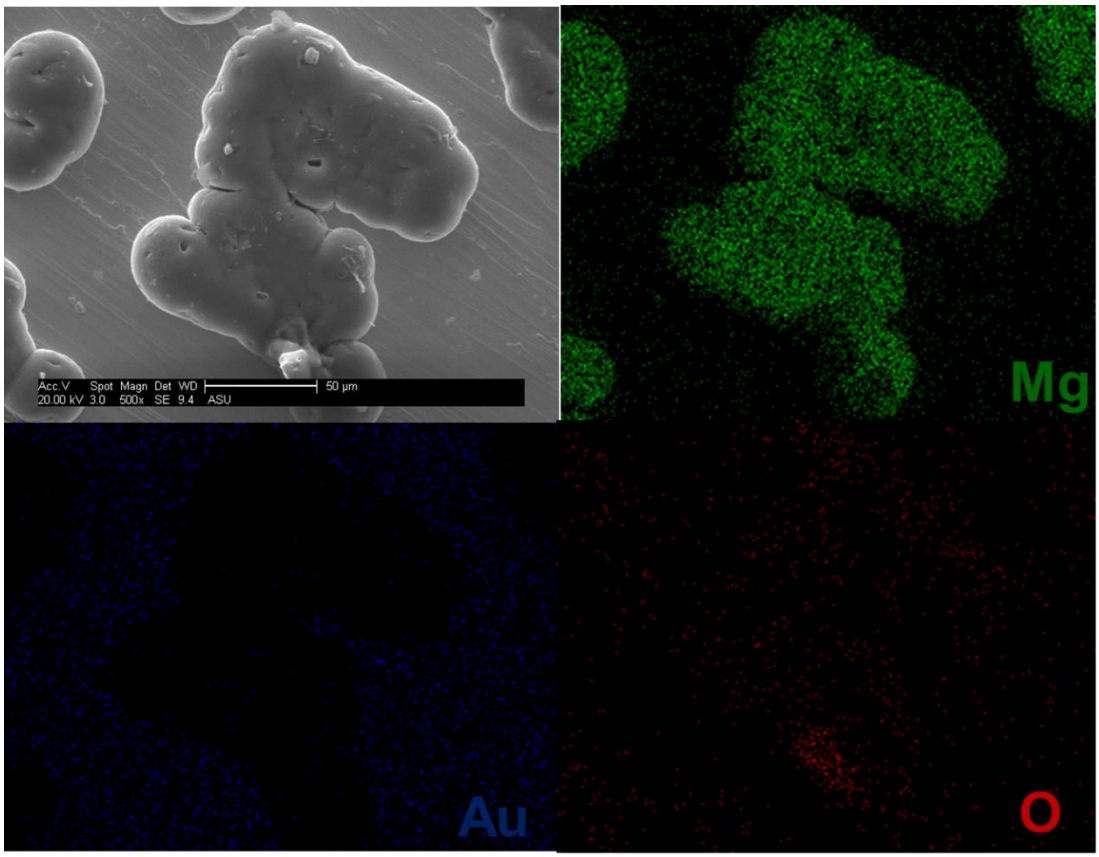

Figure A9: EDS elemental mapping for the area in figure 35b.

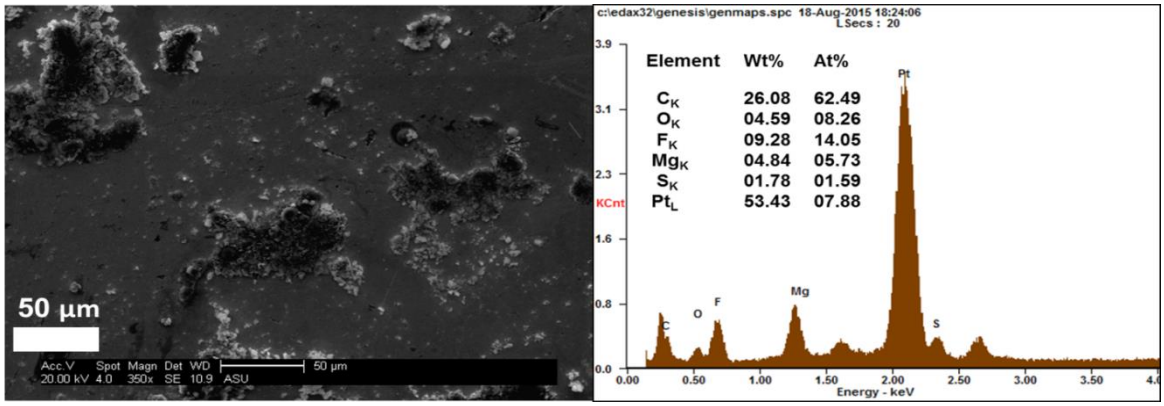

Figure A10: SEM image (*left*) and EDS spectrum (*right*) for 0.1 mA/cm^2 deposition from 0.75 M $Mg(BH_4)_2$/BMPyrTFSI.

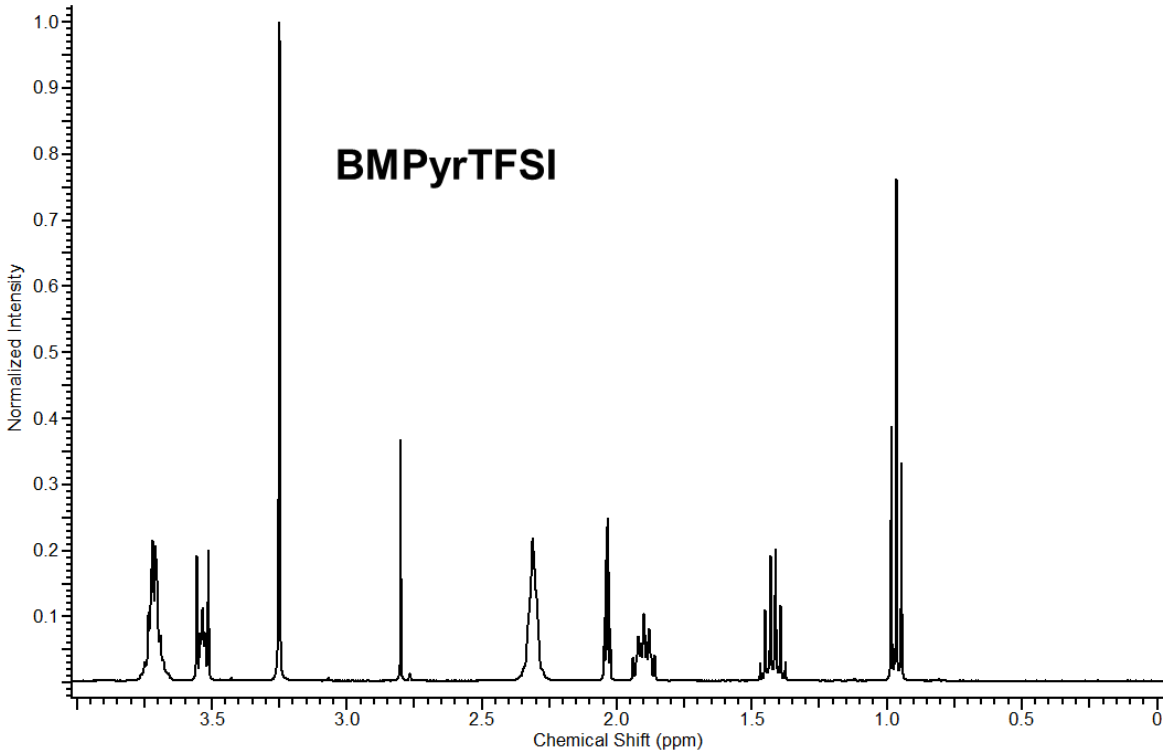

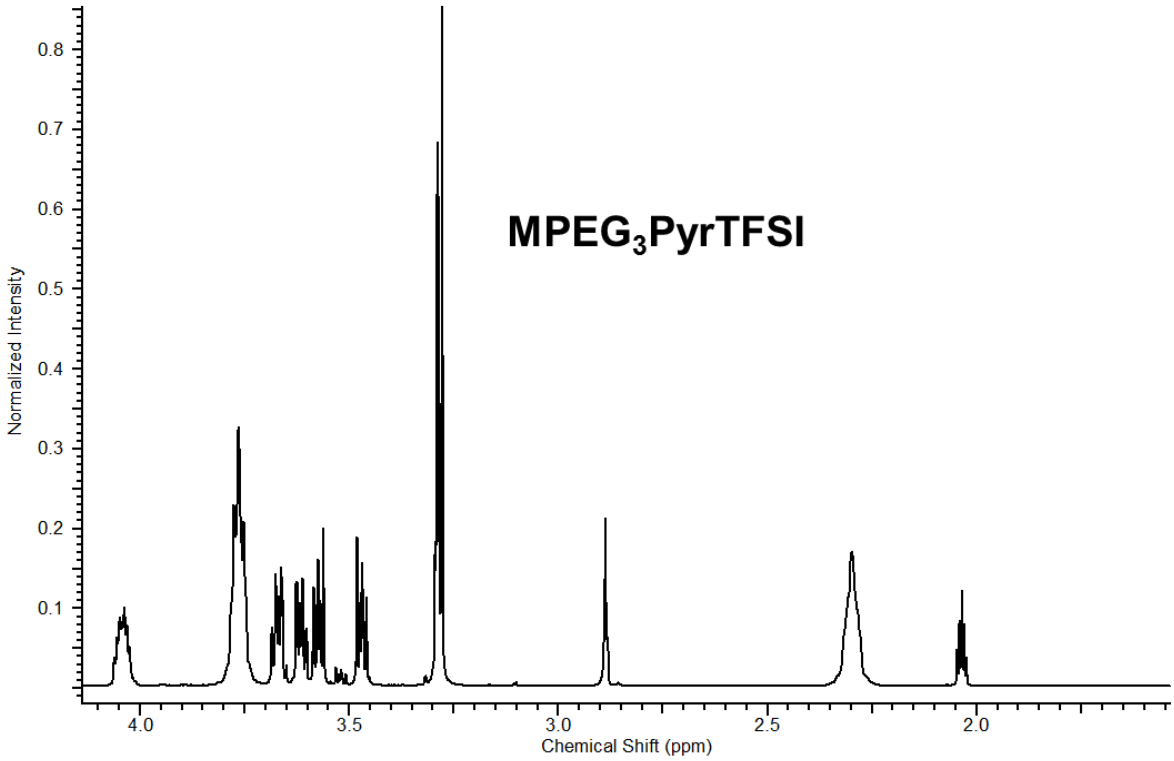
MPEG3PyrTFSI
Normalized Intensity
0.8
0.7
0.6
0.5
0.4
0.3
0.2
0.1
4.0
3.5
3.0
2.5
2.0
Chemical Shift (ppm)

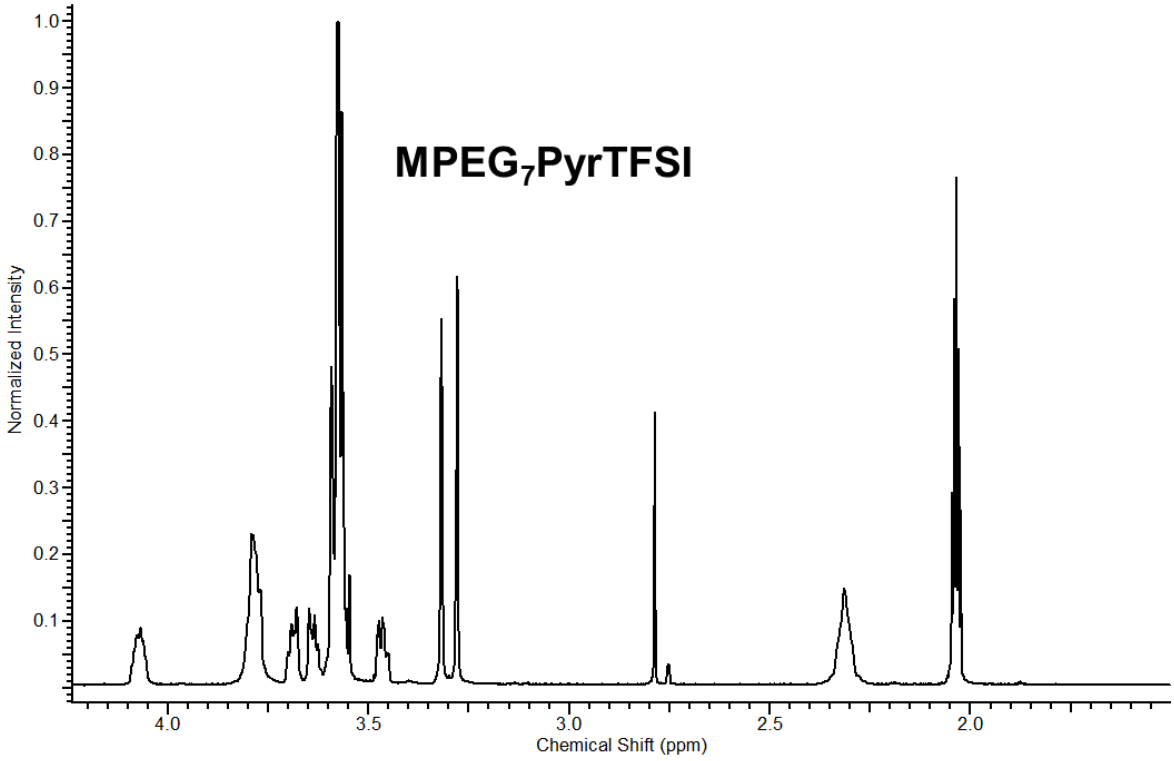
MPEG7PyrTFSI
Normalized Intensity
1.0
0.9
0.8
0.7
0.6
0.5
0.4
0.3
0.2
0.1
4.0
3.5
3.0
2.5
2.0
Chemical Shift (ppm)